The Synthesis and Investigation of Novel Inorganic Nanotubes and Nanorods

by

Graham Dawson

Thesis presented towards the degree of

DOCTOR OF PHILOSOPHY

University of St Andrews **July 2006**

DECLARATION

I, Graham Dawson, hereby certify that this thesis, which is of approximately 40,000 words in length has been written by me, that it is the record of work carried out by me and that it has not been submitted in any previous application for a higher degree.

date 7/7/06 signature of candidate

I was admitted as a research student in October 2002 and as a candidate for the degree of Doctor of Philosophy in October 2003; the higher study for which this is a record was carried out in the University of St. Andrews between 2002 and 2006.

date 7/7/06 signature of candidate

I hereby certify that the candidate has fulfilled the conditions of the Resolution and Regulations appropriate for the degree of Doctor of Philosophy in the University of St. Andrews and that the candidate is qualified to submit this thesis in application for that degree.

date 7/7/06 signature of supervisor

In submitting this thesis to the University of St. Andrews I understand that I am giving permission for it to be made available for use in accordance with the regulations of the University Library for the time being in force, subject to any copyright vested in the work not being affected thereby. I also understand that the title and abstract will be published, and that a copy of the work may be made and supplied to any *bona fide* library or research worker.

date 7/7/06 signature of candidate

Acknowledgements

I would like to thank my supervisor Dr. Zhou for all his help and guidance and the degree of freedom that he has given me. I would also like to thank Ross Blackley and Calum Dickinson for all their help around the department.

I am grateful to Dr. Wright and Professor Cole-Hamilton for the use of their labspace.

On a personal note I would like to thank my flatmates in St. Andrews for the duration of my research, Stu, Bob and Tom for your help with chemistry and day to day life and making the last three years so enjoyable.

I also wish to thank Gary, Craig, Jak, Liv, Sam, Banjo, Chris, Nick and Dave for their friendship and support throughout this period.

Finally, I would like to thank my mum and dad for all their support and encouragement over the past four years.

I am grateful for the funding provided by the ESPRC/St. Andrews University School of Chemistry.

Abstract

$H_2Ti_3O_7$-related crystalline nanotubes, known as the first example of synthesized nanotubes of transition metal oxide hydroxides, were produced and their structures were investigated using various techniques, such as HRTEM, SEM, EDX and XRD, etc. By studying the early-stage of the reaction, we have postulated the following mechanism: TiO_2 particles react with 10 molar NaOH to form a disordered amorphous phase. Single sheets of trititanate extrude from this phase, forming thin plates with several layers of $H_2Ti_3O_7$. These layers scroll up to form nanotubes due to an asymmetry of hydrogen concentration on the surface sheet. The tension in the layer is the driving force for the forming of the trititanate nanotubes. The tubes have an interlayer spacing of 0.78 nm and diameters of ca. 8 nm.

Based on the above mechanism, trititanate nanotubes were also produced directly from bulk $H_2Ti_3O_7$ and hexaniobate nanotubes from ion-exchanged potassium hexaniobate, $K_{4-x}H_xNb_6O_{17}$, using an amine as an intercalating agent. The intershell spacing of the latter has been altered using different template amines.

The reaction between tantalum oxide, Ta_2O_5, and tetraethyl ammonium hydroxide, $(C_2H_5)_4NOH$ in water, results in the formation of a mixture of tantalum oxide nanotubes and nanorods. The tubes had an interlayer spacing of 0.62 nm and an average diameter of 8.8 nm. The rods had an average diameter of 31 nm. The formation mechanism is thought to be that amine molecules are intercalated into the structure and cleave off the nanorods, or in the case of the tubes, sheets, which scroll to form the tubes. Other inorganic nanotubes, e.g. WO_3 with an average diameter of 12.9 nm and Al_2O_3 of 37.6 nm in diameter, were also synthesized.

Contents

Chapter 1 Introduction

1.1 Nanotechnology

The research and development of nanoscale materials- so called nanotechnology, is a huge world-wide business – the USA's federal budget for 2002 includes $604 million for research and development in nanotechnology- the estimated global market for products based on nanoscale materials for 2011 is in excess of $1 trillion and a government report in this country has stated that the field of nanotechnology and its application is crucial to the future competitiveness and productivity of the UK economy.[1]

Nanotechnology has recently been at the forefront of discussions in the media. Prince Charles called upon the Royal Society to investigate the "enormous environmental and social risks" of nanotechnology in a planned report. The report was released on the 29th of July 2004[2]. The media is often guilty of glaring hyperbole, both for and against, scientific issues, with global warming and stem cell research two obvious cases. Nanotechnology is no exception, with the grey-goo hypothesis, a term referring to a hypothetical end of the world event in which out-of-control self-replicating robots consume all living matter while building more of themselves, receiving many column inches due to Prince Charles's comments.

Nanotechnology is any technology that exploits phenomena and structures that can only occur at the nanometer scale, which is 10^{-9}m. Nano comes from the Greek word for dwarf. These phenomena include quantum confinement, which can result in different electromagnetic and optical properties of a material between nanoparticles and the bulk material, the lowering of melting point of a material when it is on the nanometer scale (the Gibbs-Thomson effect). Nanoscience is the study of nanoscale phenomenon used in nanotechnology, including atoms, molecules, quantum dots and

macromolecular assemblies. Surface effects, such as Van der Waals force, hydrogen, ionic and covalent bonding, hydrophobicity and hydrophilicity dominate to the virtual exclusion of macro scale effects, for example, turbulence.

Nanotechnology is based on the fact that the properties of materials become markedly different when their size approaches that of a few hundreds or tens of atoms. In the field of catalysis, a material that exhibits no catalytic behaviour on the macroscale, may become an efficient catalyst in the form of nanoparticles. The vastly increased ratio of surface area to volume opens new possibilities in surface-based science, such as catalysis.

Critics of the advances in nanotechnology have expressed concern over the potential toxicity of new classes of nanosubstances that could adversely affect the stability of cell membranes or disturb the immune system when inhaled or digested. The effects of exposure to asbestos and quartz have been greatly studied and this knowledge will be useful for risk assessment. However the levels of exposure to nanoparticles in ambient air and in pollutants are relatively high, with no specific toxicological (physiological) effects.

Other public fears appear to revolve around the use of nanotechnology in the military. While advanced nanomaterials obviously have applications for improving existing weapons and military hardware through novel properties such as improved strength to weight ratios or modified reflectivity to electro magnetic radiation for stealth applications, direct use of new technology as a weapon is in the realms of science fiction.

Advances in nanotechnology will impact electronics and computing, medicine, cosmetics, foods, energy – all walks of life. Sun blocks which contain nanoparticles of zinc oxide that absorb ultra violet light are commercially available. Targeted delivery

of medicine is still someway off, but research in Stanford have used carbon nanotubes coated in folate molecules, making it easy for them to pass into cancer cells, but unable to bind with their healthy cousins. These nanotubes are heated by near infra red lasers, which normally pass through the human body, and destroy the cancer cells. A major cause of death and disease in the third world is a contaminated water supply. Researchers also developed a method of large-scale production of carbon nanotube filters for water quality improvement, which will be lightweight and therefore easily transported. Socks have been developed that are made with nano-silver particles give anti-microbial protection, preventing bacteria and fungus that cause itchiness and smells[3].

The basis of nanotechnology is nanomaterials. These can be grouped according to their dimension: nanoparticles are zero dimensional, nanowires and nanorods are one dimensional, nanosheets and nanofilms are two dimensional, whereas nanotubes have some special properties in between one and two dimensional materials. This project is concerned with the synthesis of nanotubes.

1.2 Nanotubes

1.2.1 Carbon Nanotubes

One of the main areas of research in nanoscale materials is in the field of nanotubes. Nanotubular materials have been of great interest since the discovery of carbon nanotubes during research into fullerene production by Iijima in 1991[4]. These nanotubes were produced using an arc-discharge evaporation method.

These tubes had a range of diameters- the smallest hollow diameter observed was 2.2 nm[4], and consisted of concentric tubes of graphene sheets, as shown in Fig. 1.1. The number of layers in each tube varied, with single walled tubes and multi-walled tubes containing up to 7 layers observed. Graphene sheets are hexagonal networks of

carbon, which stack to form bulk graphite. When the sheets fold the unsaturated bonds at the edge of the layers join, which results in fused cylinders of graphene. The nanotubes can be open-ended or closed by caps containing five-membered rings Carbon nanotubes can exhibit metallic or semiconducting properties[5], which depend on the way the graphene sheets fold to make the tubes and the properties of the electrons in the tubes. The graphene sheets can fold in one of three ways, producing: armchair tubes, which are metallic, zigzag tubes, which are semiconducting and chiral tubes, as shown in Fig. 1.2.

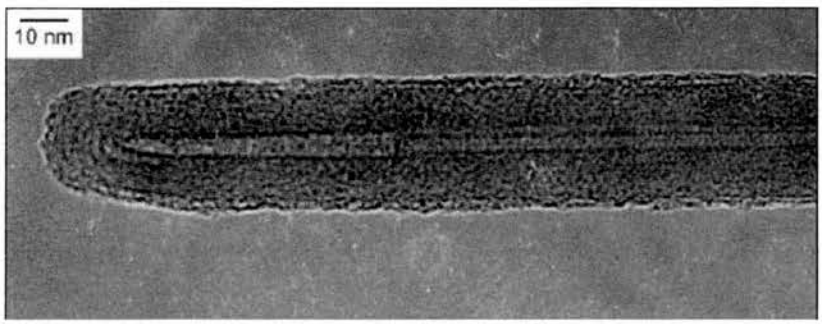

Fig 1.1 Multiwalled carbon nanotube, reproduced from ref[6].

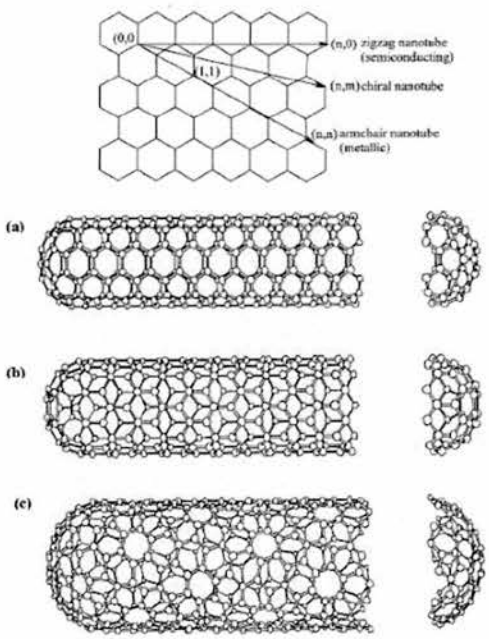

Fig. 1.2 Nature of folding of a graphene sheet to form carbon nanotubes, reproduced from ref[6].

Carbon nanotubes already have many uses, with many potential applications being researched. Nanotubes have been added to tennis rackets and strings to increase strength[7]. The carbon nanotubes can potentially be used for the same role as silicon in electronic circuits, but on the molecular level. Carbon nanotubes exhibit field emission behaviour and have potential uses in thinner and more efficient flat panel displays such as televisions and monitors[8].

In September 2005 Texas-based Applied Nanotech, in conjunction with six Japanese electronics firms, has created a prototype of a 25-inch TV using carbon nanotubes. The prototype TV does not suffer from "ghosting," as some types of digital TVs.[9] Ray Baughman's group from the University of Texas produced the current toughest material known in 2003 by spinning fibres of single wall carbon nanotubes with polyvinyl alcohol. This material was four times stronger than spider silk.[10] The same group have produced transparent carbon nanotube sheets that are stronger than the same-weight steel sheets and have demonstrated applicability for organic light-emitting displays, low-noise electronic sensors, artificial muscles, conducting appliqués and broad-band polarized light sources that can be switched in one ten-thousandths of a second.[11] Single walled carbon nanotubes have been used in room temperature transistors and can be described by the semiclassical band bending model used for traditional semiconductor devices[12].

In the field of heterogeneous catalysis carbon materials have been used to disperse and stabilise metallic particles[13,14]. The selectivity compared to aluminium oxide support increased dramatically in the production of cinnamylalcohol. Metal nanocluster filled nanotubes have applications in methanol oxidation as well as the gas-phase catalysis of hydrocarbons. High selectivity has also been shown in the oxidative dehydrogenation of ethylbenzene to produce styrene[15], the high surface area along with

the selectivity of the graphitic nanotubular material gives a higher specific yield of styrene than graphite itself and offers an alternative to the direct dehydrogenation of ethylbenzene to styrene, which is one of the most important industrial processes in the world. In the process a potassium-promoted iron catalyst is used at high temperatures. This method is thermodynamically limited and, because of the required excess of steam, very energy consuming.

The application of these nanotubes in energy storage has also been of much interest[16]. Using Fe nanoparticles as catalysts both the outer and the inner tubules are electrochemically active for Li^+ intercalation, suggesting possible applications such as Li ion battery anodes.

1.2.2 Metal chalcogenide nanotubes

The discovery of carbon nanotubes led to a great deal of research in inorganic nanotubes. The metal dichalcogenides,MX_2 (M= Mo, W, X= S, Se), have a structure analogous to that of the graphite sheets and have a tendency to roll into curved structures rather than bend. This makes them ideal for research into nanotubes.

The first inorganic tubes to be discovered were WS_2 by Tenne in 1992 (Fig. 1.3)[17]. These tubes were produced by heating a thin film of tungsten in an atmosphere of hydrogen disulphide. The crystalline tubes have a range of diameters, a tube of outer diameter 16 nm and length of 200 nm was observed with the smallest tube having an inner diameter of 4 nm and containing 4 layers. The tubes contained concentric layers of WS_2 and were closed at the tip, exhibiting the same nature as the carbon tubes. The same sulfirization process produced molybdenum disulphide nanotubes from MoO_3. The tubes contained between 5 and 10 layers and had lengths in excess of a few micrometers[18]. The interlayer spacing is 0.62 nm. Both reactions also produced

inorganic nested fullerenes along with the nanotubes. The metal trisulfides were formed as intermediates in the production of metal disulfide nanotubes. Accordingly, both WS_2 and MoS_2 nanotubes have been formed directly by the decomposition of WS_3 and MoS_3 respectively in a hydrogen atmosphere[19]. MoS_3 was prepared by the decomposition of $(NH_4)_2MoS_4$ at 400 °C in argon. Heating the MoS_3 in hydrogen at 1200-1300 °C gave a high yield of nanotubes. The tubes had an external diameter of 20-30 nm and a wall thickness of 10-15 nm. Nanotubes were also produced by the direct decomposition of amonium thiomolybdate in H_2 at 1200-1300 °C. These tubes had an outer diameter of 25 nm and a wall thickness of 10 nm. The interlayer spacing was 0.6 nm and the tubes were closed tipped. WS_2 nanotubes were produced by the thermal decomposition of ammonium thiotungstate in hydrogen at 1200-1300 °C. The tubes have an outer diameter of 25 nm and a wall thickness of 10 nm. These nanotubes also consist of concentric rings.

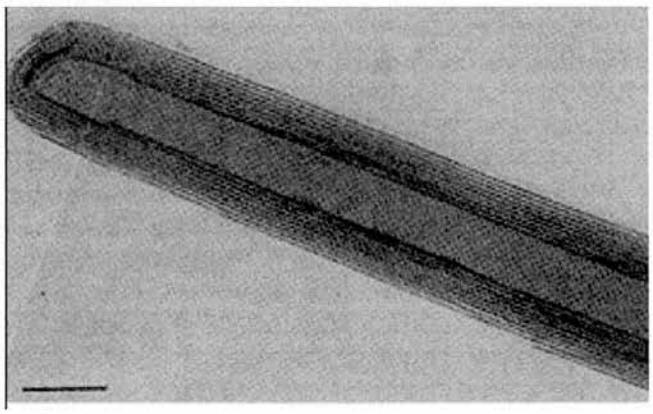

Fig. 1.3 HRTEM image of a WS_2 nanotube. Scale bar 10 nm. Reproduced from ref [17].

Both MoS_2 and WS_2 nanotubes have also been synthesised by direct synthesis from the vapour phase[20]. MoS_2 hollow microtubes, several millimetres in lengths and less than 0.1 μm wall thickness, were grown directly from the vapour phase. Scanning

electron microscopy studies reveal that instability of thin weakly bonded sheets against folding causes the tube growth directly or indirectly beyond the formation of turbulent gas flow. The tubes had a large range of diameters and lengths, with one tube having a diameter of 11 μm and a 60 nm thick wall, while another 100 μm in length and 8 μm in diameter. The tubes were grown by the iodine transport method at 1000 K in an evacuated silica ampoule at a pressure of 10^{-3} Pa and with a temperature gradient of 2 K/cm. After 22 days the ampoule was cooled to room temperature at a rate of 15 °C per hour. WS_2 nanotubes with diameters of 73 nm, 2 μm and less than 20 nm were also produced by the same group[21]. The polycrystalline tubes grow by the spiral winding of molecular layers. These tubes were also grown by the same iodine transport method (at 1060 K and with a temperature gradient of 1.6 K/cm).

The synthesis of nanotubes of the group 6 metal dichalcogenides from their corresponding trichalcogenides opened this synthetic route to other transition metals, even though the trichalcogenides may be crystalline rather than amorphous, in the case of Mo and W. The properties of the second row transition metals zirconium and niobium are very similar to those of molybdenum, as are those of the third row metals hafnium and tantalum to tungsten.

Crystalline $NbSe_2$ nanotubes have been prepared by the decomposition of the triselenide at 970 K under Ar[22]. The rate of argon flow has an effect on the ratio of nanotubes and nanorods in the final product. At a smaller flow rate, there was a higher percentage of nanotubes in the final product, while higher flow rates gave a greater percentage of nanorods. These tubes mostly contain more than 10 layers. One example of a tube contains 16 layers and has an outer diameter of 57 nm. The nanostructures have outer diameters in the 35–100 nm range, with lengths in excess of several hundred nanometers. The inner diameters of the tubes were in the range 10-50 nm. The

nanostructures are metallic and become superconducting at 8.3 K. The nanotubes appear to exhibit a concentric layer structure, with both open and closed tipped tubes observed. Several varieties of closed tip tubes have been documented: non-spherical tips exhibiting 90° bends, conical tips and hemispherical caps have all been observed within the nanotube sample. Most of the tubes are open ended. It is thought that defects cause the tubes to close.

A similar method was later used to produce nanotubes of Nb and Ta disulfides[23]. The precursor trisulfides, NbS_3 and TaS_3, are crystalline, however the reaction still produced nanotubes. NbS_2 nanotubes were prepared by heating NbS_3 in a H_2 stream at 1000 °C for 30-60 minutes. A NbS_2 tube is shown in Fig. 1.4. The layer separation in the walls is 6 Å, corresponding to the (002) plane of bulk NbS_2. The nanotubes are hollow with inner diameters of 4-15 nm TaS_2 nanotubes were prepared by the same method, with TaS_3 decomposed at 1270 K under H_2. The tubes were also hollow with inner diameters of 20-40 nm. The NbS_2 nanostructures were not superconducting. Both types of nanotubes are single crystals with closed non-spherical, almost rectangular ends.

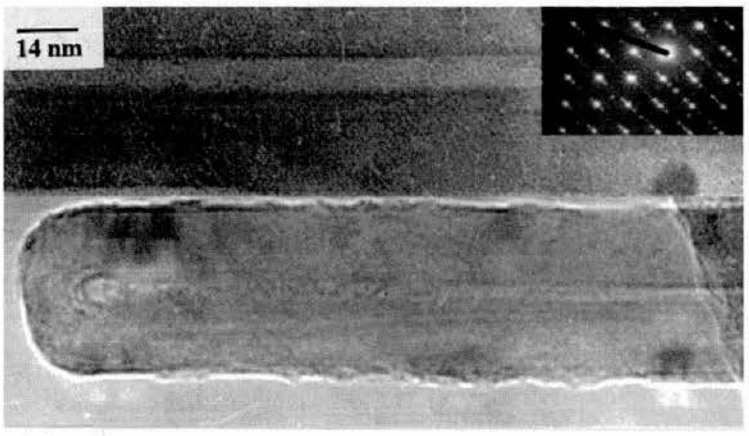

Fig. 1.4 TEM images of a NbS_2 nanotube with a closed nonspherical tip. Inset is a SAED pattern of the tube, showing it to be a single crystal. Reproduced from ref[23].

Crystalline zirconium and hafnium disulfide nanotubes were produced by the decomposition of the appropriate trisulfide at 1170 K in a H_2/Ar atmosphere[24]. Many of the polycrystalline nanotubes exhibit rectangular tips, with nearly all showing non spherical ends. The tubes are closed multiwall structures, like carbon nanotubes. HfS_2 nanotubes had an interlayer spacing of 5.8 Å, which corresponds to the (001) plane. The diameter of the nanotubes is between 55-60 nm, with inner diameters in the range of 17-30 nm. The inner diameter of some of the nanotubes varies along the length. The outer diameter of ZrS_2 nanotubes is approximately 125 nm, with inner diameters of around 60 nm. Nanorods and nested structures are also seen in the product. The same group also produced TiS_2 nanotubes by the thermal decomposition of TiS_3 in a H_2 and He atmosphere at 800 °C, however the tubes were beam sensitive and no structural data could be observed.

Nanotubes of rhenium(IV) sulfide, ReS_2, have been prepared by carbon nanotube templating[25]. Rhenium is also a third row transition metal, with an atomic number one higher than tungsten. A multiwall carbon nanotube material was impregnated with solutions of NH_4ReO_4 or $ReCl_5$, followed by drying and sulfidation with H_2S at 1000 °C. Like previously described MS_2 nanotube compounds, ReS_2 has a layered structure consisting of S-M-S layers. The rhenium layers closely follow the multi-walled carbon nanotube layers over the closed end of the nanotube, showing that a closed cylindrical structure is present.

A number of other synthetic routes to metal chalchonide nanotubes have been established including surfactant-assisted synthesis and hydrothermal means. Intense electron irradiation has been used to prepare $NbSe_2$ nanotubes[26]. The radiation produces defects, some of which are thought to be nanotubes. The superconducting critical current density is increased with the radiation[27].Surfactant-assisted synthesis

has been used extensively to produce nanotubes of transition metal chalchonides, as well as Bi_2S_3 tubes. The nanotubes produced have a wide range of diameters and lengths.

Nanotubes of CdS and CdSe have been formed using surfactant-assisted synthesis[28]. Cadmium oxide was reacted with a selenidizing agent, NaHSe, in the presence of a surfactant such as Triton 100X (t-octyl- $(OCH_2CH_2)_xOH$, x = 9,10) to produce CdSe nanotubes. In the case of CdS thioacetamide was used as a sulfidizing agent. The reaction produced nanowires as well as nanotubes. The yield of nanotubes compared to nanowires is controlled by the concentration of surfactant, which changes the morphology and shape of the micellar cavity. In both CdS and CdSe reactions, a higher concentration of surfactant preferentially produces nanotubes. CdSe nanotubes have outer diameters of 15-20 nm, with inner diameters of 10-15 nm. The polycrystalline tubes contain several concentric layers, with an interlayer spacing of 3.23 Å. The tubes have lengths of up to 5 μm. The CdS nanotubes have an outer diameter of 50 nm, with an inner diameter of 15 nm and lengths of a few microns. The diameter of the nanowires of CdS is in the range of 40-160 nm and length 3–4 μm and the diameter of the nanowires of CdSe is in the range of 30-40 nm and length ranges up to 1 μm.

Bi_2S_3 nanotubes[29] have also been grown through surfactant-assisted growth using Triton-X 100 as the template at 115 °C for 12 h. These nanotubes are nearly uniform in dimensions, with diameter around 120 nm and length up to 8 μm, their nature being single crystalline.

Template synthesis followed by sulfidisation was used to prepare ZnS nanotubes[30]. Monocrystalline ZnO columns were grown using electodeposition. The ZnO column was heated in H_2S above 400 °C to give ZnS coated ZnO. Tubular

structures of ZnS are prepared by etching out the ZnO core due to the large difference in etch resistance between ZnS and ZnO. Typical dimensions of the ZnS tubes are a length of 1–3 μm, a diameter of 100–300 nm, with a wall thickness of 10–30 nm. The tubes have a hexagonal shape, due to the shape of the column and can be found with closed or open tops.

NiS nanotubes[31] were prepared by a hydrothermal route- $Ni(NH_3)_4^{2+}$ was sulfidised by CS_2 in aqueous amonia. The tubes had a scroll structure.

A hydrothermal method was also used to produce $Cu_{5.5}FeS_{6.5}$ nanotubes[32]. Elemental copper, sulfur and iron (from the steel autoclave), lithium hydroxide monohydrate and hydrazine were put in an autoclave with distilled water and reacted at 195 °C for 6 days. The nanotubes have a diameter of 50 nm and the thick walled variety appeared more crystalline than the thin walled tubes. The polycrystalline tubes are mostly open-ended. The tubes have a layered structure containing MS_4 tetrahedra and are thought to be formed by the rolling of the layer planes. The nanotubes exhibit armchair and zig-zag types.

The main synthetic route to metal chalconide nanotubes is the decomposition of the metal trisulfide or triselenide, however a number of other synthetic routes have been employed, including surfactant assisted synthesis and hydrothermal means.

1.2.3 Group 13 nitride nanotubes

The next variety of tube to be discovered were boron nitride, which were created in a carbon free plasma discharge between a BN packed tungsten rod and a cooled copper electrode[33]. The multiwalled tubes are semiconducting with interlayer distances of 3.3 angstroms. Boron nitride also has a very similar structure to graphite and is an ideal material from which to make multi-walled nanotubes. Many other methods to produce

BN tubes have been discovered, including the decomposition of borazine in the presence of transition metal nanoparticles.

Gallium nitride nanotubes[34] have also been prepared using ZnO nanowires as a template. The GaN was deposited by chemical vapour deposition and created tubes with inner diameters of 30-200 nm and wall thickness of 5-50 nm. The ZnO nanowire template was removed by thermal reduction and evaporation at 600$^{\circ C}$ with 10% H_2 in Ar, which resulted in ordered arrays of GaN nanotubes on the substrate. The ZnO nanowires were grown on sapphire wafers using a vapour deposition process. The tubes are single crystals with most having one open end and one end closed, due to the mechanism of formation.

1.2.4 Silicon oxide nanotubes

The sol-gel method is the main process used in the production of SiO_2 nanotubes. With slight modifications nanotubes of varying size and shape are produced from essentially the same precursor method. Hollow tubes of SiO_2 were synthesised by hydrolysing tetraethylorthosilicate in a mixture of ammonia, ethanol, water and tartaric acid in 1995[35]. The tubes are square with widths of 0.8-1 μm and are 200-300 μm in length, as shown in Fig. 1.5. A small amount of cylindrical tubes was also formed in the reaction. The diameter of the tubes decreased with decreasing reaction temperatures down to a diameter of 0.05-0.1 μm. It is thought that the SiO_2 sol particles are the starting point for the formation of tubes and that they are formed in the tartaric acid matrices. Worm type silica-gel hollow tubes[36] were also produced by hydrolysing tetraethylorthosilicate in a mixture of ammonia, ethanol, water and citric acid monohydrate. The TEOS was dissolved in the ethanol, citric acid and water and allowed to stand for half an hour to form the sol, at which point the ammonium

hydroxide solution was added. The reaction was kept at room temperature for 2 h. The worm like tubes were mostly open at one end and closed at the other, with a circular cross section and a square inner compartment. The outer diameters were in the range 0.6-1.2 μm and lengths of between 8 and 12 μm. The tubes have been shown to be amorphous by X-ray diffraction.

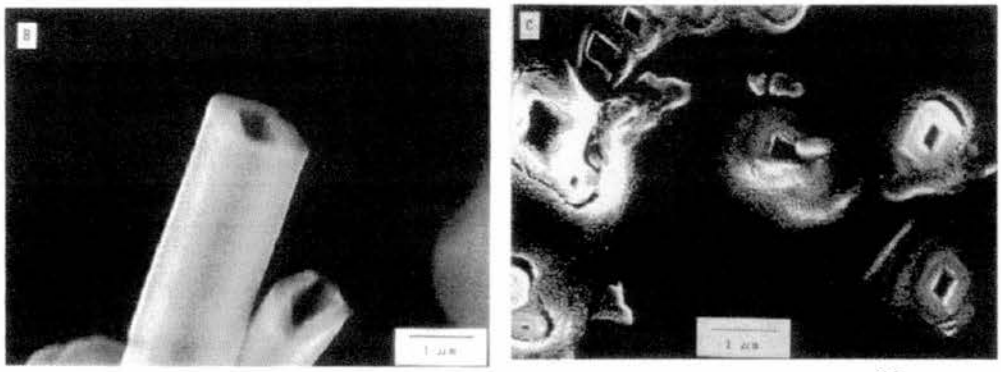

Fig. 1.5 SEM image of square SiO_2 tubes reproduced from ref[35].

Silica nanotubes were also formed by first dissolving a template (C_{16}TMAB) in water, then adding nitric acid and TEOS to form a gel[37]. This gel was dried and then added to an autoclave along with ammonium hydroxide solution. The organic structure directing agents were removed by calcining the sample at 560 °C. The tubes produced had diameters of 30-100 nm. Using this post synthetic ammonia hydrothermal treatment of the silica the pore size, nanochannel regularity and morphology were restructured. In a separate synthesis, laurylamine hydrochloride was used as the surfactant template around which TEOS was hydrolyzed[38]. The amine salt forms micelles around which the Si forms aggregates, and then condenses. Nanotubes are formed by calcination of the aggregates. Si aggregate formation could also be followed by trisilylation treatment. Trimethylsilylation inactivated the silanol groups on the surface of the tube, thus inhibiting the condensation of silanol groups between the different bundles, and yielding long individual silica tubes. This method also meant that

the surfactant was removed without the need for calcination. The aggregates had a diameter of 10 nm. The diameter of the nanotubes can be altered using surfactants of different alkyl chain lengths. If Laurylamine hydrochloride (n = 12) was replaced with a surfactant of n = 18 the diameter of the tubes increased from 5 nm to 6.25 nm.

Citric acid has been used as a structure modifier to produce individual silica nanotubes, which were 0.5-20 μm in length and had outer diameters in the range of 50-500 nm. The method used was very similar to that which produced the worm like tubes. However the tubes produced here have a much smaller diameter[39]. The nanotubes were amorphous in nature.

The sol-gel technique has also been used to dope silica into TiO_2 nanotubes[40]. The Si content was varied using different amounts of TEOS in the reaction. Butanediol and TEOS were mixed in a beaker at room temperature. Tetrapropylorthotitanate was then added to the mixture to create the sol which was aged at room temperature for a few days. The gel was calcined to bring about the formation of nanotubes. The pore size of the nanotubes decreases with increasing Si content, however the surface area after calcination is dramatically increased, showing that Si doping affects the sintering process and suppresses grain growth of Ti nanoparticles. The outer diameters of the nanotubes are 13 nm, with inner diameters of 3 nm. EDX has shown that titanium and silicon are homogeneously distributed in the tubes, which suggests that the tubes are constructed from homogeneous Si-doped titania.

Nanotubes of SiO_2 were produced using carbon nanotubes as templates[41]. Using tetraethylorthosilicate as a precursor for SiO_2, carbon nanotubes were coated in silica. When the tubes were heated in air to remove the carbon through oxidation the tubular nature of the silica was retained. The SiO_2 nanotubes are amorphous and crystallise only at very high temperatures.

Strong visible photoluminescence has been observed from mesorporous SiO_2 material with nanotubes within tubes[42]. The material was produced by dissolving a surfactant (C_{16}TMAB) in water and adding SiO_2 as a silicon source, Al_2O_3 as an aluminium source and sulphuric acid, to create a gel. The gel was heated in an autoclave at 100 °C for 48 h and the product calcined at 580 °C to remove the organic template. The strong photoluminescence of the material is due to the presence of Si-OH complexes located on the surface of the nanotube.

1.2.5 Aluminium oxide nanotubes

Alumina nanotubes were prepared by an electrochemical method[43]. An aluminium film deposited on a p-type Si substrate was anodised in dilute sulphuric acid. A potential was applied to the alumina film. The nanotubes formed were attached to the anodic porous alumina film. If the potential is applied to the Si surface, the tubes produced are designated NSA (normal stepwise anodisation). If the potential is applied to the Al, then the tubes are termed LSA (lateral stepwise anodisation). The NSA tubes were smaller than the LSA tubes. The longest nanotube observed was 650 nm in length and had outer and inner diameters of 35 and 12 nm. Branchy alumina nanotubes were also produced in the same synthesis[44]. The stem of the branches was 50-70 nm in outer diameter and 30-45 nm in inner diameter, and the two branches had an outer diameter of 40 nm, with inner diameter of 20 nm.

Al_2O_3 tubes were also produced using carbon nanotubes as templates[41]. Using aluminium isopropoxide as a precursor for Al_2O_3 carbon nanotubes were coated in alumina. When the tubes were heated in air to remove the carbon through oxidation the tubular nature of the Al_2O_3 was not preserved.

1.2.6 Transition metal oxide nanotubes

Nanotubes of transition metal oxides that do not possess layered structures have been prepared by employing the sol–gel technique, membrane-confined growth and templated growth. In the cases of carbon and metal dichalcogenide nanotubes, the parent material contains discreet layers which can fold into nanotubes. A major synthetic route in the production of these tubes is decomposition of the appropriate tri-sulphide or tri-selenide. In the case of transition metal oxides, which are not layered in nature, but contain three-dimensional connected networks, precursors for the oxide or sol-gel chemistry have been mainly used to produce nanotubes. Many of the tubes are produced using template synthesis.

The need to use templates often results in loss of tubular structure when the template is removed. This is because the reactants are deposited onto the surface of the template with little control over order or arrangement, resulting in amorphous walls, which without the permanent support of the template are unstable. Templates used include carbon nanotubes, with the reactants deposited onto the tube surface and structure directing amine molecules.

Nanotubes of V_2O_5 and MoO_3 were produced using carbon nanotubes as templates[41]. To produce V_2O_5 coated carbon tubes a V_2O_5 gel prepared by passing sodium metavanadate through a cation exchange column was used. The crystalline V_2O_5 tubes were well preserved after they were heated in air to facilitate the oxidation of the carbon. Molybdenum tubes were prepared using carbon nanotubes coated with molybdic acid.

Nanotubes of vanadium oxide have been produced by more than one group through the reactions of structure directing amines and a vanadium oxide precursor. The tubes have been prepared from a vanadium alkoxide precursor[45]. The hydrothermal

reaction of the product of the hydrolysis of vanadium triisopropoxide and hexadecylamine produced scroll like nanotubes. The template was irretrievably intercalated between the layers. The crystalline tubes were up to 2000 nm long and had an outer diameter between 50 and 70 nm. It was later discovered that the amine could be exchanged with other amines[46], as shown in Fig. 1.6. The distance between the layers can be controlled by the alkyl chain length of the amine. Diamines created tubes with thicker walls. Vanadium oxide nanotubes have also been prepared using non alkoxide precursors such as $VOCl_3$ and V_2O_5 and long chain amines[47]. This method requires stirring of V_2O_5 and the amine to allow intercalation, followed by a 7 day hydrothermal reaction at 180 °C in an autoclave. These nanotubes also had a scroll structure and an outer diameter of 75-100 nm.

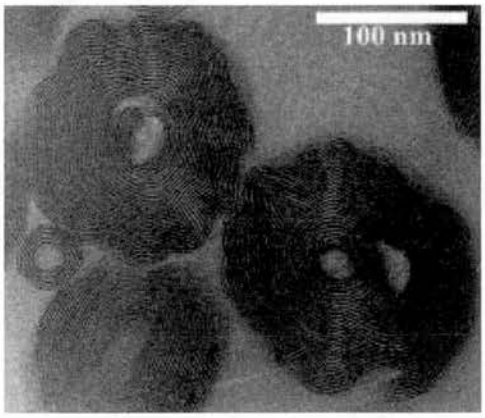

Fig.1.6 TEM image of diamine intercalated VO_x nanotubes showing their scroll structure, reproduced from ref[46].

Nanotubes of TiO_2 have elicited a great deal of research since their discovery and have been produced by some very different synthetic routes. In 1996 TiO_2 nanotubes were synthesised using a porous alumina mould[48]. The tubular structure was formed by electrochemical deposition in the mould. The tubes were amorphous, but after heat

treatment polycrystalline tubes were observed. The inner diameter of the tubes decreased from about 100 (controlled by the pore size of the membrane) to 70 nm during the crystallisation. Kasuga[49] discovered another method of producing titanium dioxide nanotubes in 1998. A mixture of titanium isopropoxide and tetraethylorthosilicate (TEOS) was hydrolyzed and gelled in an incubator, and the gel further heated to 870 K resulting in the precipitation of fine TiO_2 crystals of the anatase phase. This material was further treated in a hydrothermal reaction with 5-10 molar NaOH solution at 380 K for 20 h to yield the TiO_2 nanotubular phase. There was also an amorphous SiO_2 phase present in the product, which was removed by chemical treatment. The product was then washed with HCl. The crystalline nanotubes had a range of diameters, with an average of 8 nm and lengths of up to 100 nm. The tubes are shown in Fig. 1.7.

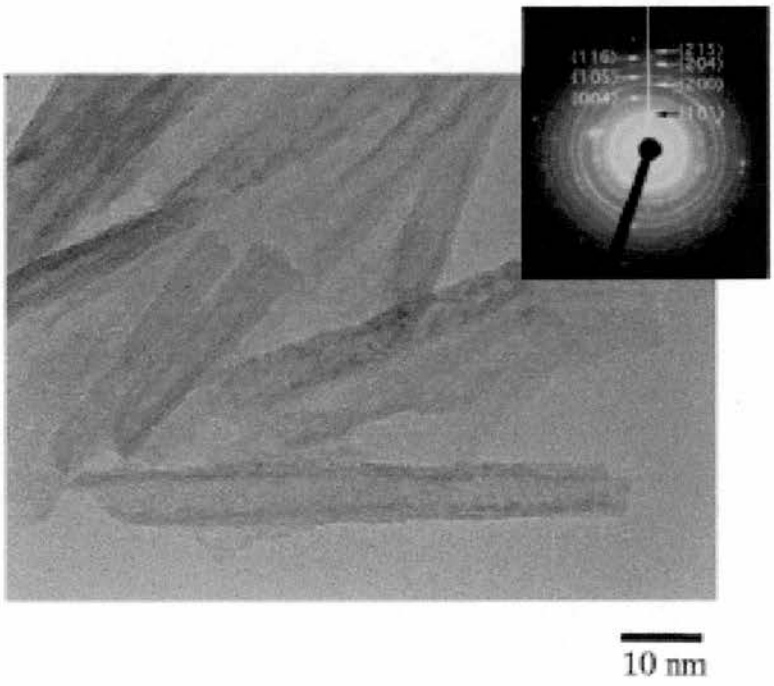

Fig. 1.7 TEM image of so-called TiO_2 nanotubes including SAED pattern, reproduced from ref[49].

Titanium dioxide nanotubes can also be formed by the direct deposition of titanium tetraflouride in the pores of an aniodically grown aluminia membrane[50]. Hollow cylinders of anatse type TiO_2 were deposited from aqueous solutions of TiF_4. The hydrolysis of TiF_4 in solution occurs stepwise to produce TiO_2. As the shape of the tubes matched that of the channels within the membrane, deposition seems to have occurred through heterogeneous nucleation on the alumina surface. The precursor solutions supersaturated with titania directly produce crystal nuclei of anatase on the surface of the alumina. The open ended cylinders had outer diameters of 200 nm and inner diameters of 100-150 nm.

ZnO nanotubes[51] have been prepared in a simple hydrothermal reaction. An aqueous solution of a ZnO precursor, $Zn(NH_4)^{2+}$, and ethanol was heated to 450K for 13 hours in a teflon lined autoclave, producing ZnO tubes. The nanotubes were 450 nm in diameter and up to 4 μm in length and are built up by ZnO polycrystals. The tubes had closed ends. X-ray diffraction has shown the tubes to have the Wurzite structure.

1.2.7 Other metal oxide nanotubes

Nanotubes containing s and p block metal oxides have been synthesised using porous templates, which result in large diameter nanotubes. Nanotubes of perovskite oxides have been produced using template mediated growth[52]. Heating the metal acetate sol with Ti-isopropoxide in ethanol produced $BaTiO_3$ and $PbTiO_3$ nanotubes. The Masked Whatman template membrane with 200 nm pores was immersed in the sol and then air-dried. The template was removed by alkali treatment. The tubes, shown in Fig. 1.8, had outer diameters of 200 nm, corresponding to the pore size, were 50 μm long, open ended and found in bundles. XRD and electron diffraction measurements

showed that the Pb tubes were formed in a tetragonal frerroelectric phase and that the Ba tubes were formed in a cubic paraelectric phase from small polycrystalline grains.

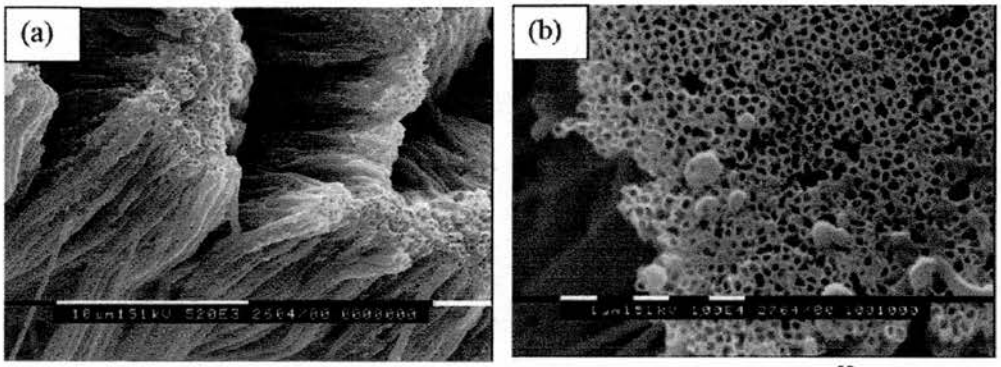

Fig. 1.8 SEM images of perovskite nanotubes reproduced from ref [52]. Image (b) is an enlargement of a bundle in image (a).

The properties of indium and gallium are very similar to those of boron and aluminium, elements whose compounds have borne some of the earliest nanotubes. Crystalline In_2O_3 and Ga_2O_3 nanotubes[53] have been synthesised using sol-gels of In^{3+} and Ga^{3+} and porous alumina templates. The template is dipped in the sol and annealed in air at elevated temperatures for 12 hours. The template is dissolved in alkali solution to give the free tubes, which have variable diameters depending on the pore size of the template and lengths of up to 10 μm. When a pore size of 200 nm is used, the nanotubes have an outer diameter of 200 nm and an inner diameter of 100 nm. One surface of the template was anchored to the substrate so after its removal the nanotubes retain the alignment of the nanochannels that were present in the template. The tubes are open ended.

1.2.8 Metal nanotubes

Very few metallic nanotubes have been synthesised. With the exception of tellurium, a p block metalloid, all the tubes were produced from transition metals.

Co and Fe nanotubes[54] have been synthesised by electrochemical deposition of the metal using polycarbonate membranes as templates. The membranes were 6 μm thick with a pore diameter of 30 nm. The electrolytes used to deposit the metals were $CoSO_4$ and $FeSO_4$. All the nanotubes and nanowires synthesised were found to have an average diameter of 30 nm, corresponding to the pore size. The wall thickness of the nanotubes is 1-2 nm. Nanotubes are created from different pulse cycles of deposition compared to nanowires. The iron tubes comprise a mixture of body centred cubic and face centred cubic phases, and are polycrystalline.

Gold nanotubes[55] have been synthesised using a pore wall modified alumina membrane. The gold tubes are prepared via electrolytic deposition onto the pore walls. By varying the deposition rate the inner diameter of the tubes can be varied, giving tubes with inner diameters of < 1 nm, making them molecular sieves. The tubes are up to 6 μm in length. Bottlenecking occurs due to preferential deposition at mouth of tubes.

Tellurium nanotubes[56] have been prepared using the polyol method. Orthotelluric acid in ethylene glycol was added to a refluxing solution of ethylene glycol. TEM images taken after stopping the reaction at different stages showed the formation of cylindrical seeds and the subsequent growth of nanotubules along the peripheral edge of the seeds. Decreasing the amount of Te precursor led to the preferential formation of solid nanorods.

Nickel nanotubes[57] have been prepared by electrodeposition of Ni in the pores of an alumina membrane. The walls of the membrane pores were modified by the addition of an amine. The nickel binds preferentially to the walls of the membrane due to its affinity with the amine. Solid nickel nanorods are formed in the absence of the amine. The membrane is removed by alkali treatment giving highly ordered arrays of Ni

nanotubes. The nanotubes were ferromagnetic, with increased coercivity compared to bulk nickel.

1.2.9 F block metal nanotubes

Due to the importance of radioactive waste management research into uranyloxy compounds has attracted considerable attention. Nanotubes of amine templated uranyl selenate, $(C_4H_{12}N)_{14}[(UO_2)_{10}(SeO_4)_{17}(H_2O)]$, have been prepared by the room temperature reaction of uranyl nitrate, butylamine and H_2SeO_4 in aqueous solution[58]. The tubules consist of single layers of $[(UO_2)_{10}(SeO_4)_{17}(H_2O)]^{-14}$ and have an eliptical cross section with dimensions of 2.5 x 2.3 nm. The internal diameter of the tubes is 15.3 Å. The nanotubes are thought to be formed around cylindrical micelles of protonated amine molecules. The same group also produced $K_5[(UO_2)_3(SeO_4)_5](NO_3)(H_2O)_{3.5}$, a compound based upon nanoscale uranyl selenate tubules[59]. The K^+ ions and H_2O molecules are present inside the tubes, with the NO_3^- groups between them. The tubes were produced from a similar reaction, with K_2CO_3 replacing butylamine. These materials are not technically nanotubes as they are not free standing structures.

Nanotubes of four Lanthenide oxides have also been synthesised from rare earth salts in hydrolysis and hydrothermal reactions. The parent oxides do not have layered structures which would make direct synthesis of nanotubes easier, so precursors of the metals must be used. Nanotubes of Er, Tm, Yb and Lu oxides[60] have been formed from template-mediated reactions using dodecylsulfate assemblies. The nanotube phase was precipitated from the reaction mixture when the rare earth salt was hydrolysed at 60 °C. The reaction contained the rare earth salt, sodium dodecylsulfate, water and urea, which was added during the reaction to vary the pH. The tubes have small inner diameters and

thin walls. Only Yb and Lu nanotubes have been obtained reproducibly from this method.

CeO_{2-x} nanotubes[61] have been synthesised by precipitation under hydrothermal conditions. An aqueous solution of cerium nitrate, $Ce(NO_3)$, was heated to 100°C and ammonia solution was added, upon which precipitation occurred. The solution was boiled for 3 minutes and then cooled at 0°C for 45 days. The diameters of the tubes range from 5-30 nm and are a few microns in length. The tubes have a cubic fluorite structure.

1.2.10 Metal halide nanotubes

Only one example of nanotubes formed from metal halides currently exists, $NiCl_2$. These tubes were prepared by heating $NiCl_2.6H_2O$ initially in air to lose the water of crystallisation, and then heated further at 450 °C under nitrogen. Closed cage structures were also formed. The nanotubes had a diameter of 70 nm and a length of 6 μm[62].

Concluding statements

Many inorganic nanotubes have now been successfully synthesised. There are six different families of inorganic nanotube: transition metal chalcogenides, metal oxide (transition metals, rare earth metals and silicon oxides), transition metal halide, mixed phase (including metal doped oxide tubes), boron based and metal nanotubes. The main synthetic methods for the production of nanotubes are sulfurisation, template synthesis, decomposition of precursor crystals, layered precursor and direct growth from the vapour phase. Nanotubes grown by the sulfurisation process or directly from the vapour phase often exhibit less defects and more perfect lattices than nanotubes grown from a template.

Carbon nanotubes contain concentric rings of graphene and can exhibit open or closed tips. The tips are spherical. Metal chalcogenide nanotubes are all crystalline and many exhibit the concentric layered structure seen in carbon nanotubes.

Tungsten and molybdenum disulfide tubes have displayed both open ended and closed tipped ends, however the tip is not spherical, as is the case in carbon tubes. Rectangular tips are often observed in metal chalcogenide nanotubes[63]. The open ended tubes are also not uniform, with conical tips apparent as well as flat open ends. Nanotubes of Nb and Ta disufide have been shown to be single crystals, as have MoS_2 and WS_2. Nanotubes of WS_2 and MoS_2 produced directly from the vapour phase are polycrystalline. NiS tubes produced by a hydrothermal route have a scroll structure. The concentric ring structure produces nanotubes of varying diameter, which corresponds to the number of layers in the tube. These types of tubes can be open-ended or close tipped.

Metal oxide nanotubes are produced mainly using templated growth. Vanadium oxide tubes have exhibited both concentric ring and scroll structures, depending on the reaction method. Several metal oxide tubes have been synthesised using sol-gel chemistry followed by templating reactions. Chemical deposition has also been used to create tubes of this kind. These chemical methods are necessary because the metal oxides are not layered structure, like the metal chalcogenides, but contain connected three-dimensional networks.

Scroll nanotubes have to be open ended due to the nature of their formation, whilst the diameter range appears to be smaller compared to the inorganic concentric ring tube structures.

Metal nanotubes have been produced mainly by chemical deposition in pores and membranes. This creates tubes whose dimensions can be controlled by the size of the pores and deposition time.

Most synthetic nanotubes have large diameters- greater than 20 nm. This is often due to the structure of the tubes- concentric rings of material consisting of many layers. The inner diameters of the tubes are often less than 5 nm. BN tubes have outer diameters of 8 nm and titania nanotubes have similar dimensions. The range of diameters is often large in the nanotubes. In the concentric ring structure this is because there is not an optimum number of layers for a tube. In the case of nanotubes grown from pores or other templates the diameters are more tightly regulated. The lengths of all nanotubes vary considerably within a sample. Many tube lengths are in the micron scale.

Inorganic nanotubes already have many uses, with many more foreseen. MoS_2 nanotubes have shown activity on the methanation of carbon monoxide with hydrogen[64]. WS_2 tubes are used as ultra sharp tips for scanning probe microscopy[65]. $NbSe_2$ nanotubes are superconducting[66]. Nanotubes can be used as storage materials for lithium batteries. Hollow nanoparticles of WS_2 act as a better lubricant than the bulk phase[67]. Vanadium oxide shows good catalytic activity in the bulk phase and redox catalytic activity is retained in the nanotubular phase. The potential applications of inorganic nanotubes range from highly porous catalysts to electron field emitters and non-toxic strengthening fibres.

Among the above mentioned inorganic nanotubes, transition metal oxide nanotubes are of interest because of the catalytic properties and the large surface area. Among these materials the titanium dioxide tubes are of great interest due to its excellent photocatalytic properties[68] and other potential applications in environmental

purification, decomposition of carbonic acid gas and generation of hydrogen gas[69-71]. The present research is therefore focussed on the synthesis and characterisation of these materials.

1.3 TiO_2 nanotubes and their potential applications

Due to its properties as a photocatalyst, titanium dioxide has applications in self cleaning materials[72]. Super-hydrophilic materials were developed by coating glass, ceramic tiles or plastics with the semiconducting photocatalyst titanium dioxide. Water forms a highly uniform sheet on contact with these surfaces. If TiO_2 is illuminated by light then grease, dirt and organic contaminants are decomposed and can easily be swept away by rain water. The photocatalytic properties of TiO_2 have also been put to use in a transparent electric windows based on dye-sensitised nanocrystalline TiO_2 solar cells[73,74]. Many sun-block creams also contain TiO_2. The tubular form of titanium oxide, due to its high surface area and higher photocatalytic activity[75], is especially interesting. When exposed to light titanium dioxide is chemically activated and decomposes organic material which comes in contact with it. It has many applications as an anti-bacterial agent, self-cleaning coating, anti-fogging coating, deodorizing coating and in water treatment. In water treatment, it can be used to remove light concentrations of organic contaminants. It is therefore suitable for use in the later stages of a water treatment. It can also be used to capture undesirable volatile organic contaminants[75]. Titanium dioxide is the most widely used white pigment, [76] it is very white and has a very high refractive index – surpassed only by diamond. The refractive index determines the non-transparency that the material confers to the matrix in which the pigment is housed. Hence, with its high refractive index, relatively low levels of titania pigment are required to achieve a white opaque coating.

Titanium dioxide is a ceramic that exists predominantly as the rutile phase with the anatase phase being less common. The rutile phase consists of distorted hexagonally close-packed oxide layers in which half of the octahedral holes are filled by oxygen (Fig. 1.9). Titanium is in oxidation state +4, therefore has no electrons in its valence shell (3d).

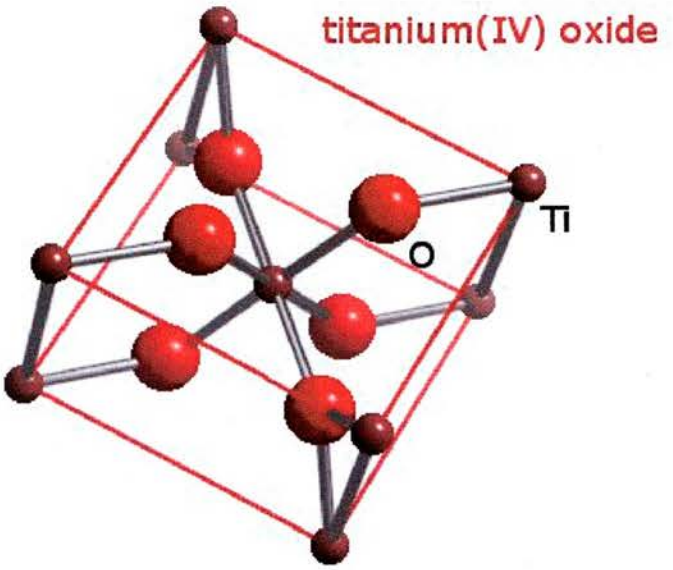

Fig. 1.19 A unit cell of rutile TiO_2.

Direct synthesis of titanium dioxide nanotubes was first achieved by Kasuga[49] et al in 1998. The nanotubular material was produced by treating crystalline TiO_2 with 10 molar NaOH. It was concluded that washing the alkali treated specimen with water followed by further reaction with HCl are vital steps in the formation of nanotubes[77]. It was thought that the reaction with NaOH converted Ti-O-Ti bonds in the starting material into Ti-O-Na and Ti-OH bonds, when this material is reacted with HCl and water these bonds form new Ti-O-Ti bonds and the nanotubes.

Work done by Chen et al[78] has later shown that the nanotubes could be prepared via a single hydrothermal alkali treatment of crystalline TiO_2. The role of NaOH in the

reaction is crucial. When the sodium hydroxide was replaced by KOH nanorods and plates were observed, but no tubes. When NaCl or $NaNO_3$ was used to replace NaOH no nanotubes were observed. A high concentration of Na^+ and strong basic conditions are required in order to produce nanotubes.

These nanotubes show neither the composition nor the structure expected from tubes made of either anatase or rutile TiO_2. The proposed structure for the nanotubes is scrolled single layers of trititanate, $H_2Ti_3O_7$. This was determined through high resolution transmission electron microscopy, X-Ray diffraction and selected area electron diffraction.[78-82] The XRD pattern of the nanotubular phase cannot be attributed to any known phase of TiO_2. All of the observed XRD peaks and SAED patterns can be indexed based on a $H_2Ti_3O_7$ structure. The structure of trititanate is usually described as corrugated ribbons of edge sharing TiO_6 octahedra[83], with each ribbon being three octahedra wide, which join corners to form stepped sheets separated by hydrogen ions, as shown in Fig. 1.10.

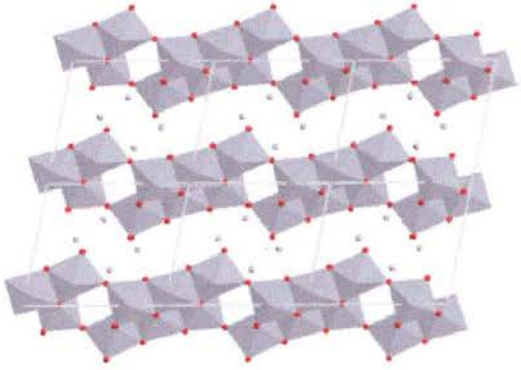

Fig. 1.10 Structure model of $H_2Ti_3O_7$ reproduced from ref [84]. Grey spheres are H^+ ions, red spheres O atoms and grey polyhedron are TiO_6 octahedron.

The nanotubes are about 9 nm in diameter and 100 to several hundred nm in length. The interlayer spacing is 0.78 nm. To confirm the model of the structure

simulations of HRTEM images and XRD patterns was carried out[78]. An excellent match was found in the image simulation and the XRD also showed a good match. The tube axis has been shown by SAED to be the [010] plane of $H_2Ti_3O_7$.

The electronic structure of trititanate nanotubes is significantly different from common TiO_2 nanocrystals[85]. Photovoltaic responses corresponding to band-to-band transition and new surface photovoltage responses extended to 550 nm have been observed under the effect of the external electric field. The responses were measured using field induced surface photovoltage spectroscopy, surface photovoltage spectrum and photoluminescence spectroscopy, three highly sensitive tools to study the photophysics of photogenerated species or excited states. The new photovoltage responses that the nanotubes exhibit are attributed to electronic transitions in surface states caused by oxygen vacancies at the surface. Due to these differences in electronic structure nanotubes are not as suitable for standalone photocatalytic applications as rutile or anatase.

The high surface area of the tubes lends itself to use in heterogeneous catalytic studies where the titania tubes serve as a support. Nanotubes containing gold nanoparticles were produced by a deposition-precipitation method, which gives gold particles with strong contact to the support[86]. Gold hydroxide was deposited onto nanotubes suspended in water via the reaction between $HAuCl_4$ and Na_2CO_3. The catalytic activity of the gold-supported titania nanotubes was evaluated in the water-gas shift reaction. The activity of the sample was higher than that of gold supported on alumina but lower than that of gold on mesoporous TiO_2. As the nanoparticle size is similar to the diameter of the nanotube it is thought that some of the gold is contained inside the tube hollow, resulting in a decrease in contact area and a lower activity. The catalytic performances of gold markedly depend on dispersion, supports, and

preparation methods. When gold is deposited on select metal oxides as hemispherical ultra-fine particles with diameters smaller than 5 nm high activity or selectivity is shown in many reactions: the combustion of CO and saturated hydrocarbons, the oxidation-decomposition of amines and organic halogenated compounds, the partial oxidation of hydrocarbons, the hydrogenation of carbon oxides, unsaturated carbonyl compounds, alkynes and alkadienes, and the reduction of nitrogen oxides. The unique catalytic nature of supported gold can be explained by assuming that the gold-metal oxide perimeter interface acts as a site for activating at least one of the reactants[87].

Sulfated tubes, which have been impregnated with sulphuric acid solution and calcined at 300 °C, have shown high reactivity towards the esterification reaction between cyclohexanol and acetic acid. The TiO_2 powder used to prepare the nanotube did not catalyze the reaction.[88] Nanotubes have also been used in catalysis through framework doping. TiO_2 nanotubes doped with nitrogen were synthesised, with nitrogen atoms substituted into oxygen sites of TiO_2. These nanotubes exhibited photocatalytic oxidation activity of gaseous isopropanol into acetone and carbon dioxide when illuminating with visible light[89].

Photocatalytic activity can also be bestowed on titanate systems by decorating them with suitable semiconductor quantum dots. Trititanate nanotubes produced by the hyrothermal reaction of anatase TiO_2 and 10 M NaOH solution were covered in CdS nanoparticles by first introducing Cd^{2+} ions into the tubes by sonicating a suspension of nanotubes in 1 M $Cd(CH_3COO)_2$ solution containing ammonia. The Cd^{2+} ions were converted to CdS by bubbling H_2S through the suspension. The photocatalytic activity of the CdS adorned nanotubes was tested by their ability to decompose methyl orange in aqueous suspension under irradiation by a mercury vapor lamp, monitored by measuring the absorbance of the dye solution. Undoped nanotubes failed to act as a

photocatalyst, however the CdS/nanotube system was active in the photooxidation reaction. The photocatalytic behaviour is interpreted as coming from the intimacy of the nanotube and CdS nanoparticles. These particles are thought to grow from Cd^{2+} ions located within the nanotube wall at the ion-exchange positions. The particles had an average diameter of 6 nm.[90]

Work done by Kukovecz et al has shown trititanate nanotubes can be formed by replacing sodium hydroxide with 10 M Na_2S[91]. The reaction was performed at 130°C for 2 weeks without shaking or stirring. The synthesis in Na_2S took much longer than in NaOH, where the reaction takes 3 days. The tubes produced appeared similar under TEM and had similar specific surface areas (AS = 116 m^2/g for 336 h reaction time) to the NaOH reaction. The tubes were, however, three times longer in the Na_2S preparation, this is probably due to the longer reaction time. The S^{2-} ion is a strong Bronsted base, therefore a 10 M Na_2S solution will provide a highly basic environment. It is therefore likely that the reaction proceeds by the same mechanism as the NaOH synthesis. The presence of S^{2-} and HS^- ions in the solution opened up the possibility of a one step reaction to produced tubes adorned with nanoparticles of metal sulphides. Due to the low solubility of CdS, Cd-EDTA complexes were used to produce monodisperse CdS particles. An aqueous solution of Cd-EDTA was prepared by mixing the disodium salt of ethylenediaminetetraacetic acid and $Cd(NO_3)_2$. This was added to an autoclave containing anatase TiO_2 and a mixture of 10 M NaOH and Na_2S (10:1). The nanotubes obtained had an excellent coverage of semiconducting CdS quantum dots with an average diameter of 5.3 nm. The complex assisted one step process gives more complete coverage of the nanotubes and smaller nanoparticles compared to the two step process (5.3 nm against 6 nm) described above.

Trititanate nanotubes also have a high potential for Li storage[92]. The tubes show high ion-exchange reactivity with alkali metal cations. A sample of trititanate nanotubes was soaked in alkali metal hydroxide solution at room temperature for 3 days. The ions intercalate between the tubular layers and pin adjacent layers. Ion exchange has also been achieved with Cd^{2+}, Zn^{2+}, Ni^{2+}, Co^{2+}, Cu^{2+} and Ag^{+}. The metal salts were dissolved in water and ammonia solution was added to stabilise the metal ion by complexation. The nanotubes were added and the suspension stirred for 20 hrs or sonicated for 100 minutes. There were no clusters or amalgamations of ions on the nanotube surface, showing that the ions were homogeneously distributed within the tubes[93].

Anatase TiO_2 nanotubes were prepared by annealing trititanate tubes at 350 °C for 2 hrs. The tubes were dried for 4 hrs at 80 °C in a vacuum oven and then calcined at 350 °C for 2 hrs. The calcined tubes had similar diameters to the starting material (~9 nm) and maintained the tubular wall structure. However, they exhibited a lower interlayer spacing of 0.62 nm, compared to 0.78 nm. The specific surface area of the tubes was 274 m^2/g, compared to 314 m^2/g for trititanate tubes, due to some particle sintering. The nanotubes were investigated as electrode material for Li storage. Through galvanostatic investigation, the nanotubes as electrode exhibited high discharge capacity and held a larger capacity in continuous cycles compared with normal crystalline TiO_2. After several cycles the coulombic efficiency (the ratio of release capacity to insertion capacity) is 100%. The initial capacity of the material fades after the first cycle, which has been observed in several electrode materials and is thought to be due to surface morphology change resulting from adsorbed water. The capacity is stable after 65 cycles which makes the material a potential candidate as a novel lithium storage material[94].

Titania nanotube arrays grown by anodizing titanium foil using an electrolyte of hydrofluoric acid in water and a platinum counter electrode have been shown to exhibit extreme changes in electrical resistance with exposure to hydrogen. Tubes of different length and diameter were formed using different anodization voltage: 20V gave inner diameters of 76 nm and lengths of 400 nm, 14 V gave 53 nm diameter and 260 nm length while 10 V gave 22 nm diameter and 200 nm length tubes. Reduction of the diameter of the tubes from 76 nm to 22 nm increases the surface area by a factor of two, but increases the hydrogen sensitivity by a factor of 200. When a sample of 22 nm tubes is exposed to hydrogen cycled from 0 to 500 ppm in discreet 100 ppm steps a three order of magnitude variation in the resistance is seen with exposure of only 100 ppm, with no hysteresis. These arrays of tubes can be used as extremely sensitive, drift free and robust hydrogen sensors. Applications for hydrogen sensors include industrial process control, combustion control and clinical use where hydrogen is an indicator for bacterial infections[95].

Trititanate nanotubes have been tested for use in decontamination of chemical warfare agents[96]. The large surface area of the tubes provides the desired rapid absorption of the contaminant while water molecules, contained within the titanate nanoscrolls, provide the necessary chemistry for the hydrolytic reaction. The decomposition of 2-chloroethyl ethylsulfide (CEES), a simulant of bis(2-chloroethyl) sulfide, mustard gas, was monitored by ^{13}C NMR. No additional water was added to the system. The nanotubes quickly adsorb the agent, encapsulate it, due to large surface area, and render it harmless through hydrolysis. In low concentrations of CEES the reaction of water with the sulfonium cation dominates, producing 2-hydroxyethyl ethyl sulfide and HCl. The reaction in higher CEES concentration goes via dimeric cation species, forming 2-hydroxyethyl ethyl sulfide as the final reaction product.

Nanotubes from $Na_2Ti_3O_7$ have subsequently been formed in a hydrothermal reaction[97]. The tubes were prepared by reacting $Na_2Ti_3O_7$ and water in an autoclave at 170 °C for 18 days, had outer diameters of 30-40 nm, with wall thickness of ~10 nm and lengths of several hundred nanometers. XRD has shown that the tubes were TiO_2. The proposed formation mechanism is that the starting material, $Na_2Ti_3O_7$, which is comprised of sheets of edge sharing TiO_6 octahedra with Na^+ ions between the layers, as shown in Fig. 1.11, under hydrothermal conditions gradually releases the sodium ions and water molecules are intercalated between the layers. As the H_2O molecules are larger than the Na^+ ions the interlayer space is increased resulting in weakened interaction between neighbouring sheets. As a result nanosheets of titanate are exfoliated and these sheets scroll into tubes due to the asymmetry in the sheet.

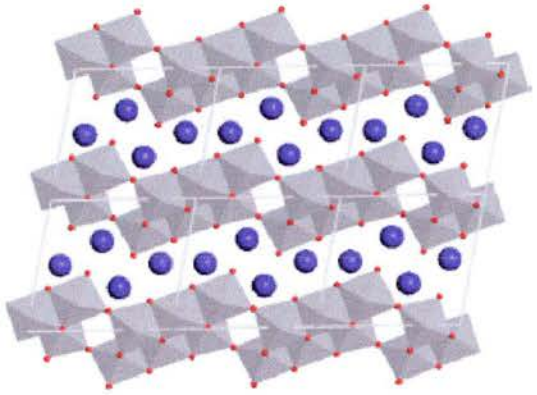

Fig. 1.11 Structure model of $Na_2Ti_3O_7$ reproduced from ref[84]. Purple spheres are Na^+ ions, red spheres O atoms and grey polyhedron are TiO_6 octahedron.

1.4 Nanotubes from $K_4Nb_6O_{17}$ and uses of material

1.4.1 $K_4Nb_6O_{17}$ and its uses

The crystalline layered material $K_4Nb_6O_{17}$ is a transparent semiconductor and photcatalyst. Its structure consists of octahedral NbO_6 units, which form a layered

structure with bridging oxygen atoms. The K^+ ions are found between the layers and compensate the negative charge. The layer structure is shown in Fig. 1.12.

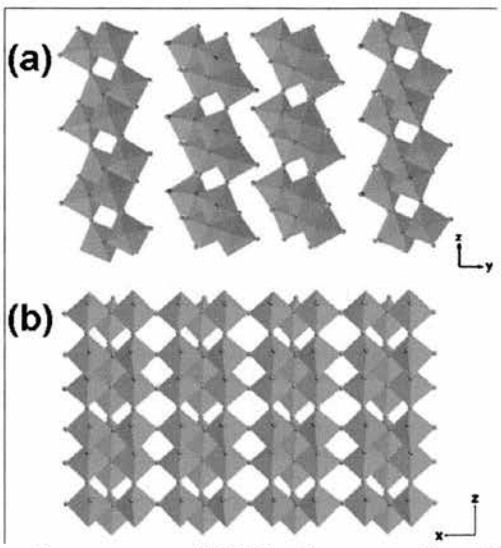

Fig. 1.12 Layered structure of $K_4Nb_6O_{17}$ reproduced from ref[98].

$K_4Nb_6O_{17}$ has two types of crystallographic interlayers, one which is easily hydrated and one which is not[99,100]. The two distinct potassium sites are shown in Fig. 1.13. Proton exchange at room temperature is therefore only partial and leads to the compound denoted $K_{4-X}H_XNb_6O_{17}$.

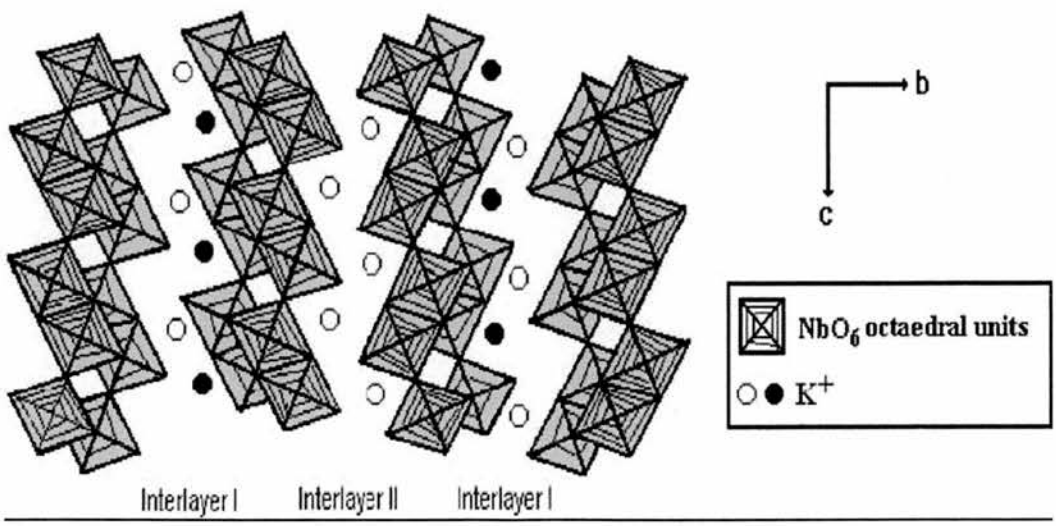

Fig. 1.13 Interlayer potassium sites in $K_4Nb_6O_{17}$, reproduced from ref[101].

Proton-exchanged $K_4Nb_6O_{17}$ showed high activity for the photocatalytic decomposition of water from aqueous methanol solution without any assistance from other materials such as noble metals[102]. The ion exchanged niobate, $K_{4-X}H_XNb_6O_{17}$, was prepared via the reaction of $K_4Nb_6O_{17}$ with H_2SO_4.

Photocatalytic ability is also shown by $K_4Nb_6O_{17}$ that has been intercalated with transition metal ions. Pt intercalated $K_4Nb_6O_{17}$ which has been treated with aqua regia to remove the platinum on the external surface has shown activity for the photocatalytic decomposition of water, without a reverse reaction[103].

Nickel-loaded $K_4Nb_6O_{17}$ has also shown activity in the decomposition of water[104]. It was shown by XPS, EXAFS, TEM and XRD that the nickel is predominantly located in interlayer I. From this structural information a mechanism for the reaction was proposed: intercalated water is reduced to H_2 on the nickel metal in interlayer I and is oxidised to O_2 in interlayer II. Hence, each niobate sheet is regarded as a "two-dimensional" photocatalyst where H_2 and O_2 evolve at different sides of the layer. Both CdS and $K_4Nb_6O_{17}$ have been shown to be photocatalysts for the decomposition of water. When the CdS was intercalated into the niobate layers the ion exchanged product showed much higher H_2 evolution activity from water than CdS or a physical mixture of CdS and $K_4Nb_6O_{17}$ in aqueous K_2SO_3 solution under visible light irradiation[105]. CdS/ $K_4Nb_6O_{17}$ was prepared by the ion exchange reaction of K^+ to Cd^{2+} in aqueous $Cd(NO_3)_2$ solution, followed by sulfurization in aqueous Na_2S solution. The more intimate contact of the CdS and $K_4Nb_6O_{17}$ enabled a more efficient transfer of excited electrons, which allowed more reduction of H^+.

There has been an abundance of research into the field of intercalation into potassium niobate and the subsequent exfoliation. $K_4Nb_6O_{17}$ single crystals were reacted directly with propylamine under hydrothermal conditions[106]. Propylamine is

intercalated into the layers of the crystal and nanosheets of an extraordinarily large size (100 μm) are exfoliated. When the reaction was repeated with hexylamine instead of propylamine an intercalatrion compound was formed but there was no exfoliation. Hexylamine is relatively hydrophobic and cannot entrain water molecules after intercalation.

Liquid crystalline nanosheet colloids[107] have been prepared by exfoliating single crystals of $K_4Nb_6O_{17}$. The use of single crystals allows for some control on the size of the nanosheets. The exfoliated material was dispersed in water and subjected to ultrasonic treatment. The liquid crystallinity of the samples depended on the lateral size of the nanosheets and the concentration of the sheets in the sample. The fluidity of the nanosheets was very high.

Methylene blue has been intercalated into $K_4Nb_6O_{17}$ single crystals in the presence of propylamine. The adsorption of methylene blue in heterogeneous systems is done to characterise the surface and to create photo and electrofunctional supramolecular systems. Propylamine was present in the reaction as direct intercalation is difficult. The reaction was done in one step to prevent exfoliation. The intercalation was confirmed by the increase in basal spacing and the expansion of the crystallographic b axis. This was the first successful example of an intercalation compound with in plane anisotropy of the guest species[108].

1.4.2 Nanotubes from $K_4Nb_6O_{17}$

When hydrogen ion exchanged potassium niobate, $K_{4-X}H_XNb_6O_{17}$, was reacted with tetra(n-butyl)ammonium hydroxide for 3 days at room temperature nanotubes were formed. The TBA^+ ions are much larger than the K^+ ions so when they intercalate into the layered structure exfoliation occurs and single asymmetric layers result. The

strain in these single layers results in curvature (due to lower energy considerations) and nanotube formation[109,110]. When potassium niobate that has not been ion exchanged is reacted with the tetra(n-butyl)ammonium hydroxide bilayers are usually produced.

Straight chain monoamines of different lengths have also been used in the place of TBAOH to produce nanotubes of different interlayer dimensions. The amines are thought to be necessary for structural conformity.[98]

Concluding statements

This thesis is concerned with the synthesis and investigation of titanium and niobium containing nanotubes. There has been a great deal of research invested in both organic and inorganic nanotubes due to their interesting possible properties, which may be markedly different from the bulk material, and applications in all fields. Among inorganic nanotubes, transition metal oxide nanotubes are of interest because of the catalytic properties and the large surface area.

Titanium dioxide and potassium hexaniobate tubes are of great interest due to the parent material's excellent photocatalytic behaviour. The synthetic route to nanotubes from titanium dioxide has been discovered and refined so that nanotubes can be produced in a single step reaction involving the hydrothermal reaction of TiO_2 and 10 molar sodium hydroxide. The structure and mechanism of formation of the nanotubes had, however, yet to be confirmed.

Nanotubes of ion exchanged potassium hexaniobate, $K_{4-X}H_XNb_6O_{17}$, have been produced using straight chain mono-amines as intercalation and exfoliation agents. If different length amines are used the interlayer spacing of the tubes can be tailored. The present research is focussed on attempting to produce tubes using di and tri substituted

amines and other small molecules. The aim of this project was the synthesis and characterisation of novel inorganic nanotubes using transmission electron microscopy.

Chapter 2 Experimental Methods

2.1 Synthesis of Specimens

2.1.1 Preparation of Trititanate Nanotubes From TiO_2

Ground rutile was added to sodium hydroxide solution and the resultant slurry was stirred at room temperature for 30 minutes. The mixture was transferred to a teflon vessel and sealed in an autoclave. The autoclave was then placed in an oven at the desired temperature for the required time.

Table 2.1 Reaction conditions of TiO_2 with 10M NaOH

Experiment Number	*Mass TiO_2 g*	*Vol. NaOH 10M (ml)*	*Molar ratio* TiO_2 : NaOH	*Temperature* ^oC	*Time (hrs)*
gd1	4.17	10	1:2	160	72
gd2	4.17	10	1:2	160	72
gd3	3.2	10	1 : 2.5	140	72
gd4.1	3.2	10	1 : 2.5	140	2
gd4.2	3.2	10	1 : 2.5	140	4
gd4.3	3.2	10	1 : 2.5	140	24
gd4.4	3.2	10	1 : 2.5	140	6
gd4.5	3.2	10	1 : 2.5	140	22
gd4.6	3.2	10	1 : 2.5	140	12
gd4.7	3.2	10	1 : 2.5	140	14
gd4.8	3.2	10	1 : 2.5	140	16
gd4.9	3.2	10	1 : 2.5	140	18
gd4.10	3.2	10	1 : 2.5	140	20
gd7	3.2	10	1 : 2.5	130	72
gd13	3.2	10	1 : 2.5	160	168

The autoclave was removed and cooled under running water for 30 minutes. The teflon vessel was removed and the solid white product was scraped out and stirred

vigorously at room temperature in 100 ml of distilled water to break up the coagulated large particles. The white solid was then washed with copious amounts of distilled water until the pH of the effluent was neutral. The product was then dried in an oven at 160°C until consecutive masses were equal. The reactions were all done in 10 molar NaOH and are listed in Table 2.1.

2.1.2 Production of Nanotubes from $Na_2Ti_3O_7$ and $H_2Ti_3O_7$

$Na_2Ti_3O_7$ was produced using the literature procedure[83]. Stoichiometric amounts of dried sodium carbonate (1.5 g) and rutile titanium dioxide (3.4 g) were ground together using a mortar and pestle and fired in an oven at 850 °C for 24 h in an alumina crucible. A pellet pressed at ~2 tonnes was made and the reactants replaced in the oven for a further 24 h. The products were analysed using powder X-ray diffraction.

$H_2Ti_3O_7$ was produced using a modified literature procedure[83]. As prepared $Na_2Ti_3O_7$ was ground in a mortar and pestle and stirred at room temperature in 1 M HCl for 3 days. The product was filtered and washed with H_2O. The structure was confirmed by XRD.

Layered titanate was ground and added to a sodium hydroxide solution and stirred vigorously for 30 minutes. The resultant mixture was poured into a teflon vessel which was placed in a sealed autoclave. The autoclave was put in an oven at the desired temperature.

The autoclave was removed and cooled under running water for 30 minutes. The teflon vessel was removed and the solid white product was scraped out and stirred vigorously at room temperature in 100 ml of distilled water to break up the coagulated large particles. The white solid was then washed with copious amounts of distilled water until the pH of the effluent was neutral. The product was then dried in an oven at

160 °C until consecutive masses were equal. The reactions completed are listed in Table 2.2. The products were all examined using TEM.

Table 2.2 Reaction conditions of titanates with NaOH

Experiment Number	Titanate	Mass Titanate (g)	Vol. NaOH 10M (ml)	Temperature °C	Time (hrs)
gd10	$Na_2Ti_3O_7$	0.1	5	160	63
	$H_2Ti_3O_7$	0.1	10	160	67
	$H_2Ti_4O_9$	0.3	10	160	67
gd12	$Na_2Ti_3O_7$	0.3	3	160	168
	$H_2Ti_3O_7$	0.1	2	160	168
gd14	$Na_2Ti_3O_7$	1	2.5*	160	72
gd15	$Na_2Ti_3O_7$	1	5*	160	72
gd16	$Na_2Ti_3O_7$	0.6	5	120	96

*-Concentration of NaOH 8.5M

2.1.3 Production of Nanotubes from $K_4Nb_6O_{17}$

The layered niobate, $K_4Nb_6O_{17}$, was produced using the literature procedure[111]. Stoichiometric amounts of dried potassium carbonate (K_2CO_3, 0.34 g) and niobium oxide (Nb_2O_5, 1 g) were ground together using a mortar and pestle and fired in an oven at 800 °C for 24 h in an alumina crucible. A pellet pressed at ~2 tonnes was made and then replaced in the oven for a further 24 h at 1050 °C. The structure was confirmed by XRD.

$K_4Nb_6O_{17}$ was also produced using a hydrothermal synthesis[112]. KOH (0.28 g) was dissolved in water (4 ml). The solution was transferred to a teflon vessel. Nb_2O_5 (0.5 g) was added to the teflon innard and sealed in an autoclave. The autoclave was then placed in an oven at 190 °C for 24 h.

The autoclave was removed and cooled under running water for 30 minutes. The teflon vessel was removed and the product was washed with distilled water and dried in an oven at 100 °C. The structure was confirmed by XRD.

As prepared $K_4Nb_6O_{17}$ was ground in a mortar and pestle and stirred at room temperature in 1M HCl for 3 days. The product was filtered and washed with H_2O. The structure was confirmed by XRD. Ion-exchanged potassium niobate, $K_{4-x}H_xNb_6O_{17}$, was added to an aqueous solution of amine and stirred at room temperature for 3 days, as shown in Table 2.3. All reactions done in 10 ml H_2O unless otherwise stated. The product was filtered and dried based on the literature procedure.[98]

Table 2.3 Reactions of $K_{4-x}H_xNb_6O_{17}$ and amine

Experiment Number	Mass $K_{4-x}H_xNb_6O_{17}$ (g)	Amine	Volume amine (ml)
gd29	0.1	Butyl amine	1.4
gd36	0.1	Diethyl amine	0.7
gd40	0.1	Triethyl amine	1
gd72	0.1	Pyrole	1
gd73	0.1	Diphenyl amine	1

Table 2.4 Reactions of $K_{4-x}H_xNb_6O_{17}$

Experiment Number	Mass $K_{4-x}H_xNb_6O_{17}$ (g)	Intercalation compound	Volume (ml)
gd50	0.1	Ethanol	2.5
gd49	0.1	Pentane thiol	1
gd41	0.1	$(Bu^n)_4P^+Br^-$	1g

The same procedure was repeated using other compounds as intercalation agents, as shown in Table 2.4. Nanotubes were not produced in these cases.

2.1.4 Synthesis of Nanotubes and Nanowires from Other Oxide Precursors

Tantalum Oxide

In method one, Ta_2O_5 (0.3 g) and tetraethyl ammonium hydroxide (1.5 ml) were added to a beaker containing 10 ml H_2O. The suspension was stirred at room temperature for 3 days. The product was filtered, dried and examined by TEM.

In the second method, Ta_2O_5 (0.3 g) was added to 10M NaOH (4g in 10 ml) solution and stirred vigorously for 30 minutes. The resultant mixture was poured into a teflon vessel which was placed in a sealed autoclave. The autoclave was put in an oven at 170 °C for 48 h.

The autoclave was removed and cooled under running water for 30 minutes. The teflon vessel was removed and the resultant pink solid was washed under vacuum with copious amounts of distilled water. The product was examined using TEM.

Tungsten Oxide

WO_3 (9.28 g, 0.04 M) was ground and added to 10 M NaOH (4 g in 10 ml) and stirred vigorously for 30 minutes. The resultant mixture was poured into a teflon vessel which was placed in a sealed autoclave. The autoclave was put in an oven at 160°C for 24 hours.

The autoclave was removed from the oven and cooled under running water for 30 minutes. The contents of the autoclave were poured into a beaker containing ~100 ml of water. The reactants had all dissolved in the reaction mixture. The mixture was neutralised by the addition of hydrochloric acid, this resulted in the precipitation of a

yellow solid. Upon filtration and drying the yellow powder crystallised into green randomly shaped crystals. The product was examined using TEM, no nanotubes were observed. The sample was subjected to mass spec analysis; ES- 335($NaWO_8$), 309, 277, 263(WO_5), 248(WO_4), 232(WO_3), analysed by the School Mass Spectrometry Service on a Micromass LCT electro-spray mass spectrometer.

^{183}W NMR, collected on a Varian Unity + 500MHz NMR machine at 20.808 MHz was attempted on the product of the reaction[113]. The spectrum of the tungsten standard, $Na_2[WO_4]$ was taken. However as the ^{183}W nucleus is $5.85x10^{-2}$ times less sensitive than carbon 13, not enough of the sample could be dissolved in solvent to produce a signal. The solvents tried were H_2O, methanol, chloroform, DMSO, acetone. The sample was run in HCl with D_2O. The literature method for the study of aqueous isopolytungtates reacted WO_3 with LiOH and the NMR of the acidified reaction solution was taken directly. As the product initially came out of the autoclave as a liquid the reaction was repeated with the hope of directly taking the NMR spectrum from the reaction solution. When the mixture was poured from the autoclave a white solid had formed. This solid could also not be dissolved in a solvent. The isotope abundance of W is: 182- 26%, 183- 14%, 184- 30%, 186- 30%.

In the second method WO_3 (0.2 g) and butyl amines (1 ml) were added to a beaker containing 10 ml H_2O. The suspension was stirred at room temperature for 3 days. The product was filtered, dried and examined by TEM.

Silicon Oxide

SiO_2 (2.57 g, 0.04 M) was ground and added to 10 M NaOH (4 g in 10 ml) and stirred vigorously for 30 minutes. The resultant mixture was poured into a teflon vessel

which was placed in a sealed autoclave. The autoclave was put in an oven at 160 °C for 24 h.

The autoclave was removed from the oven and cooled under running water for 30 minutes. The contents of the autoclave were poured into a beaker containing ~100 ml of water. The reactants had all dissolved in the reaction mixture. The mixture was neutralised by the addition of hydrochloric acid. The water was removed using a rotary evaporator. The resultant solid contained the product and NaCl salt, the later was dissolved in water while the silicon material did not re-dissolve due to its insolubility at this pH. The product was examined using TEM.

Aluminium Oxide

Al_2O_3 (4.08 g, 0.04 M) was ground and added to 10 M NaOH (4 g in 10 ml) and stirred vigorously for 30 minutes. The resultant mixture was poured into a teflon vessel which was placed in a sealed autoclave. The autoclave was put in an oven at 160 °C for 24 h.

The autoclave was removed from the oven and cooled under running water for 30 minutes. The contents of the autoclave were poured into a beaker containing ~100 ml of water. The product was examined using TEM.

2.2 Characterisation of Nanotubes

2.2.1 Selected Area Electron Diffraction

When the electron beam passes through a crystalline specimen it is scattered by the crystal planes, as shown in Fig. 2.1, defined by (h k l) according to Bragg's law:

$$2d\sin\theta = n\lambda \qquad 2.1$$

where d is the d-spacing of the crystal planes, n the order of reflection and θ the angle of incidence (Bragg angle). As the electron wavelength for an electron microscope operating at 200 kV is 0.0251 Å, much smaller than the wavelength used in conventional X-ray diffraction, the Bragg angle is also much smaller due to Bragg's law.

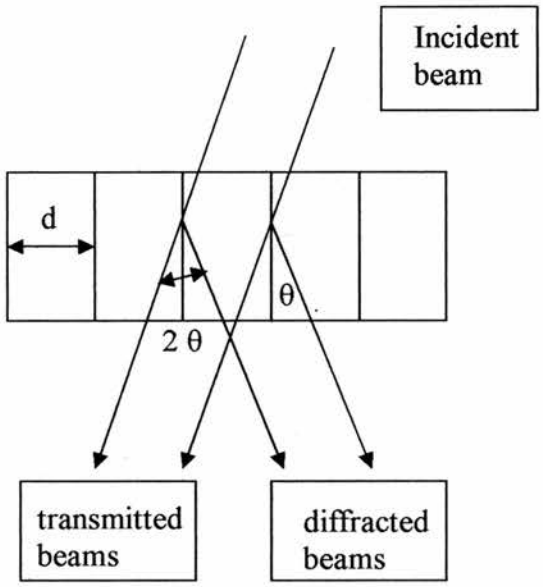

Fig. 2.1 Electron beam passing through a crystalline sample.

Both transmitted and diffracted beams are focused by the objective lens to the back focal plane. The beams diverge and form a magnified image of the object in the intermediate image plane. Below this plane, two modes of operation are possible: imaging and diffraction, as shown in Fig. 2.2.

In the image mode, the lower lens magnifies further the intermediate image onto the florescent screen. When a weaker lens is used underneath the intermediate image plane, the electron wavefront in the objective back focal plane is projected onto the screen, giving the diffraction mode. Selected area electron diffraction (SAED) is achieved when an aperture is inserted into the intermediate image plane, which enables the collection of beams scattered only from a small area in the specimen, as shown in Fig.

2.3. In the intermediate image plane a larger aperture can be used than would be necessary near the specimen due to the enlarged image.

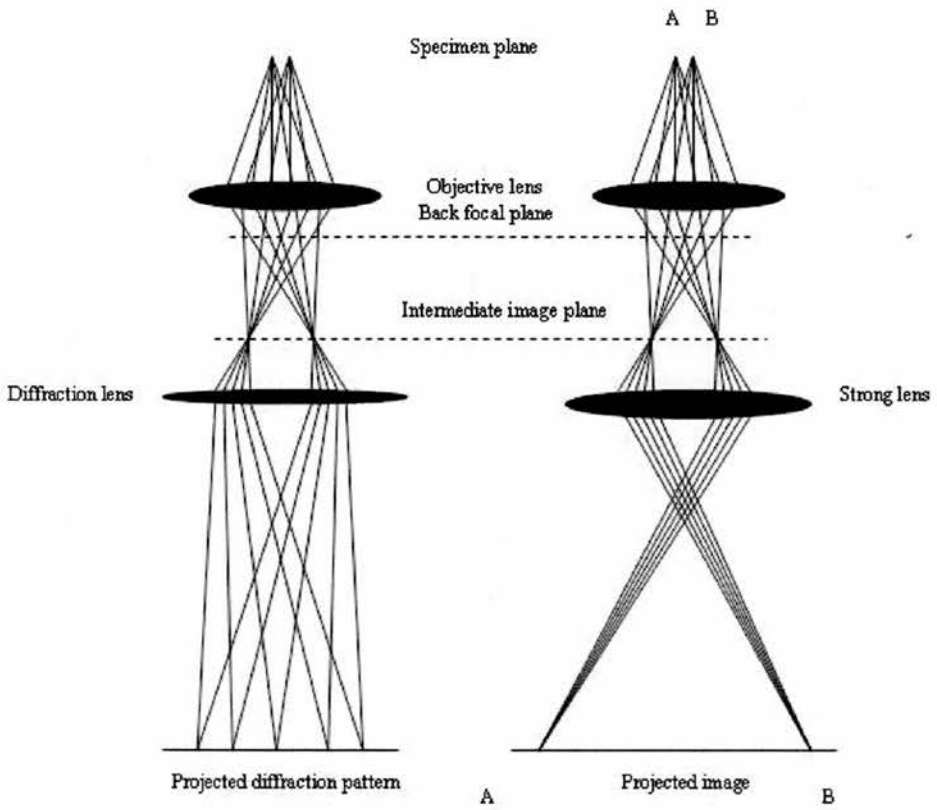

Fig. 2.2 Schematic diagram of the modes of microscope operation.

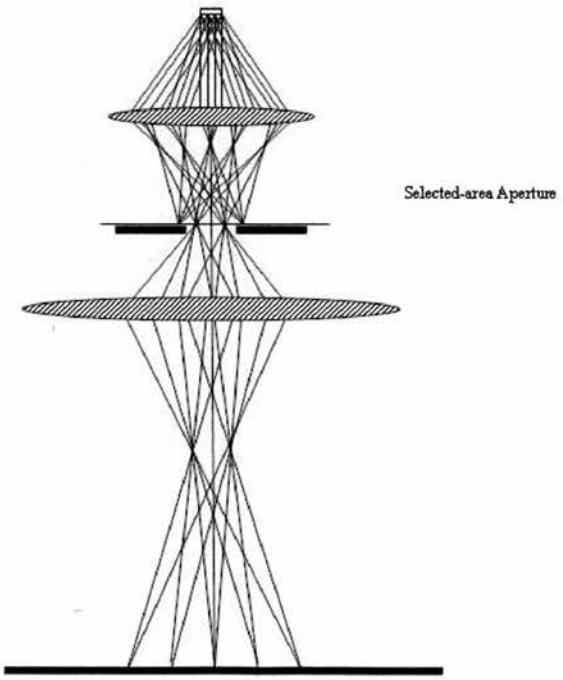

Fig. 2.3 Schematic diagram of selected area electron diffraction.

Determination of the unit cell

A SAED pattern can be regarded as a two-dimensional projection of the reciprocal lattice of a crystalline specimen. Since the Ewald sphere (diffraction sphere) is large, with a radius of $1/\lambda$, the set of diffraction spots obtained along one zone axis is an almost undistorted picture of the zero level of the reciprocal lattice. Consequently, distances can be measured directly from the recorded negative film of a SAED pattern and the corresponding vectors in the reciprocal lattice can be calculated from these distances using the camera length, L, as shown in Fig. 2.4. The angle related to two spots on the SAED pattern is the direct projection of that in the reciprocal lattice.

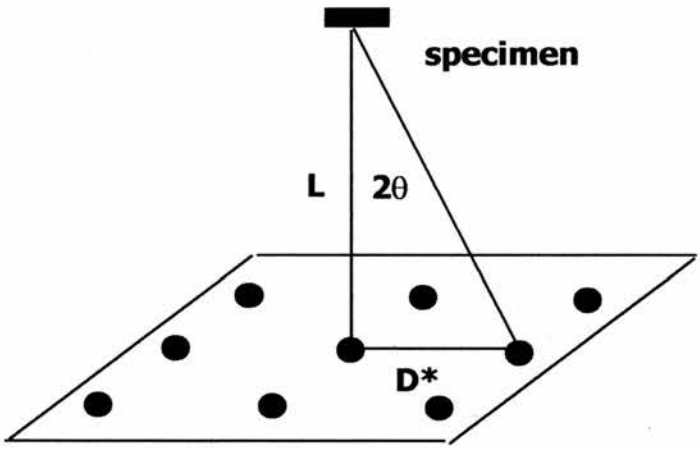

Fig. 2.4 Schematic drawing of relationship between camera length and direct measurement on the SAED pattern

$$2\theta = \frac{D^*}{L} \qquad 2.2$$

The distance in reciprocal space corresponding to that measurement, denoted d*, is given by:

$$d^* = \frac{2\sin\theta}{\lambda} = \frac{D^*}{L\lambda} \qquad 2.3$$

as $\sin\theta \approx \theta$, if θ is small and measured in radians.

A SAED pattern normally gives only a magnified 2D reciprocal lattice. The first level in addition to the zero level of a reciprocal lattice may be observed and information about the third dimension may be obtained. A more practical method is to record many SAED patterns along various zone axes from different crystallites if the specimen is monophasic or from the same crystallite by tilting. Combination of these SAED patterns leads to an enlarged 3D reciprocal lattice. The reciprocal unit cell parameters, a*, b* ,c* ,α* ,β* ,γ* can then be calculated. The volume of the reciprocal cell is given by:

$$V^* = 2a^*b^*c^*\left[\sin(s^*)\sin(s^*-\alpha^*)\sin(s^*-\beta^*)\sin(s^*-\gamma^*)\right]^{1/2} \qquad 2.4$$

where $s^* = \frac{1}{2}(\alpha^* + \beta^* + \gamma^*)$

Real space unit cell parameters can be calculated by the relations:

$$a = \frac{b^*c^*\sin\alpha^*}{V^*} \qquad b = \frac{c^*a^*\sin\beta^*}{V^*} \qquad c = \frac{a^*b^*\sin\gamma^*}{V^*} \qquad 2.5$$

$$\alpha = \cos^{-1}\left[\frac{\cos\beta^*\cos\gamma^* - \cos\alpha^*}{\sin\beta^*\sin\gamma^*}\right]$$

$$\beta = \cos^{-1}\left[\frac{\cos\alpha^*\cos\gamma^* - \cos\beta^*}{\sin\alpha^*\sin\gamma^*}\right]$$

$$\gamma = \cos^{-1}\left[\frac{\cos\beta^*\cos\alpha^* - \cos\gamma^*}{\sin\beta^*\sin\alpha^*}\right]$$

Electron specimen interactions

The transmission function of the sample, $\psi_0(r)$ can be expressed in terms of the specimen potential, $\phi(r)$, which disturbs the electron waves as they pass through the specimen:

$$\psi_o(r) = \exp\{i\sigma\phi(r) - \eta(r)\} \qquad 2.6$$

where $\phi(r)$ is the projected electrical potential within the specimen, σ the interaction parameter and $\eta(r)$ is a physical absorption coefficient. The electrical potential term describes how the phase of the electron beam is altered by the specimen. The physical absorption coefficient incorporates the electrons lost due to inelastic scattering giving rise to X-ray emission and other processes.

When the interaction between the electron beam and the specimen is weak (i.e. σ is small) the exponential can be expanded and only the first two terms, which are linear, need to be considered. Therefore the expression for the object transmission function becomes

$$\psi_0(r) \approx 1 + i\sigma\phi(r) - \eta(r) \qquad 2.7$$

This is known as the weak phase object approximation and is valid if both the phase change and the physical interaction coefficient are small. This is similar to the kinematic approximation for x-rays and is permissible only if the scattering is very weak.

The amplitude of the beam in the diffraction plane, $\psi_D(S)$, is a Fourier transform of the object transmission function.

$$\psi_D(S) = \delta(0) + i\sigma V(S) - \Omega(S) \qquad 2.8$$

where $\delta(0)$ represents the undiffracted primary beam, V(S) is the Fourier transform of $\phi(r)$ and $\Omega(S)$ is the Fourier transform of $\eta(r)$. Assuming there are no contributions from lens effects or defocus, the amplitude of the electron waves in the image plane is the inverse Fourier transform of the diffracted beam amplitude:

$$\psi_I(r) = 1 + i\sigma\phi(r) - \eta(r) \qquad 2.9$$

The interaction of electrons with the specimen is much stronger than with X-rays. This leads to the interaction parameter for electrons with matter:

$$\sigma = \left(\frac{2\pi}{\lambda}\right)\left(\frac{1}{E[1+(1-\beta^2)^{1/2}}\right) \qquad 2.10$$

where E is the accelerating voltage, λ is the electron wavelength and β is the ratio of the electron velocity to the speed of light. From this equation it can be seen that decreasing the accelerating voltage leads to a greater interaction between the electron beam and matter. Relativistic effects altering wavelength at higher accelerating voltages also affect this interaction. Due to the strong interaction of the electrons with matter only small amounts of specimen are required to produce diffraction which allows the collection of information from submicron sized crystals. The strong interaction can also be problematic as it means that experiments need to be carried out in a vacuum, as the electron beam would be scattered by gas molecules.

The weak phase object approximation is a gross over simplification of the situation occurring when the electron beam passes through the sample. Multiple scattering accounts for this.

Multiple scattering

One of the most important effects of the strong electron-matter interactions is multiple scattering. In other words, the scattered electrons might be scattered again before emerging from the other side of the specimen. This is shown in Fig. 2.5. The amplitude of the diffracted beams are still the Fourier transform of the object wave function, $\psi_0(r)$, but $\psi_0(r)$ has become a complicated function with a complex relationship to the object potential. This results in the diffraction intensities, and thus the image formed by recombination of the diffracted beams, being difficult to interpret. The intensities of the diffraction spots are no longer simply related to the structure, they can be affected by the specimen thickness. It is possible to generate diffracted beams

which are normally forbidden by the rules of space-group symmetry. Consequently, extracting space-group information from the intensities of spots in SAED patterns is fraught with difficulty.

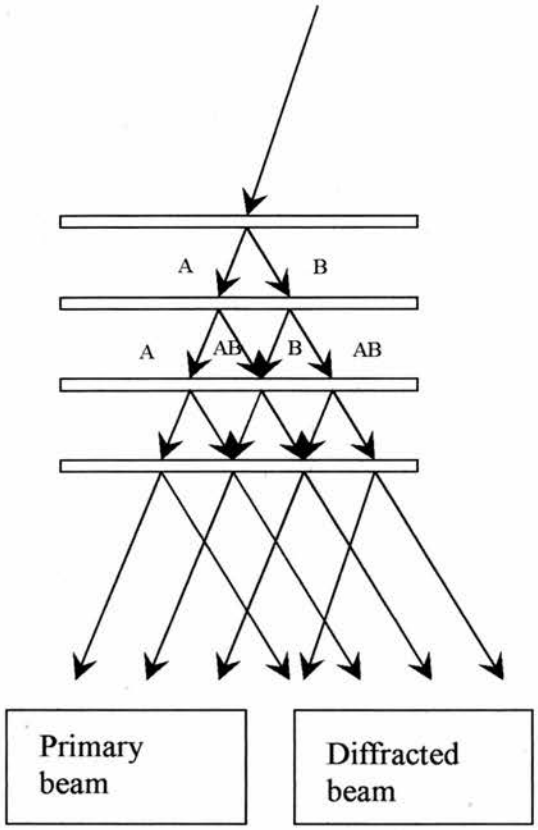

Fig. 2.5 A schematic diagram of two-beam dynamic scattering

We must consider the case where a single incident beam is diffracted by successive planes in a crystal. After diffraction there will be the remainder of the incident beam and one diffracted beam. If the specimen is considered to be layers of atoms, or planes of electronic potential, with an interlayer spacing of Δz then it is possible to consider the scattering due to each successive layer. Supposing that after diffraction by the first layer the amplitude of the incident, or primary beam, A_P, is reduced to A, and the amplitude of the diffracted beam, A_D, is B. As these two beams progress and encounter the second plane, part of the primary beam will be diffracted and add amplitude to the

diffracted beam, and part of the diffracted beam will itself add to the primary beam. After the second layer the resultant primary and diffracted beams are made up as follows:

$$A_P = \left(A^2 + B^2\right)\mathbf{exp}(i\delta) \qquad A_D = 2AB\mathbf{exp}(i\delta) \tag{2.11}$$

The exp($i\delta$) term is the phase factor arising from the propagation of the wave between the layers.

After n layers, the primary and diffracted beams can be expressed as:

$$A_P = 1/2\left[(A+B)^n + (A-B)^n\right]\mathbf{exp}\{(n-1)i\delta\} \tag{2.12}$$

$$A_D = 1/2\left[(A+B)^n - (A-B)^n\right]\mathbf{exp}\{(n-1)i\delta\}$$

These amplitudes express the dynamic inter-exchange of energy between the primary and the diffracted beam as the electron wave propagates through the crystal and gives rise to the name dynamic theory. For energy to be conserved the sum of the intensities of the primary and the diffracted beams must be unity.

$$|\mathrm{A_P}|^2 + |\mathrm{A_D}|^2 = 1 \tag{2.13}$$

Therefore $\mathrm{A} = \cos\omega$ and $\mathrm{B} = i\sin\omega$

Consideration of how the electron wave is altered by the electric potential in the planes allows the object transmission to be expressed as:

$$\psi_0(x,y) = \mathbf{exp}\{i\sigma\phi(x,y)\Delta z\} \tag{2.14}$$

where $\phi(x,y)\Delta z$ is the projected electrical potential in the layer.

If the scattering by this single layer is small then we can expand the exponential and only consider the linear terms. In other words we assume kinematic scattering but only for one layer. Consequently the total amplitude of the wave after diffraction, $\psi_D(h,k)$, by the plane is:

$$\psi_D(h,k) = \delta(0,0) + i\sigma F(h,k)\Delta z\delta(h,k) \tag{2.15}$$

where F(h,k) is the Fourier transform of $\phi(x,y)$ and δ(0,0) is a point function of unit weight at the origin. Thus δ(0,0) represents the primary beam and F(h,k)Δz represents the diffracted beam.

Assuming that when ω is small cos(ω)→1 and sin(ω) → ω means that the wave function of the diffracted beam can be rewritten as:

$$\psi_D(h,k) \approx \cos[\sigma F(h,k)\Delta z]\delta(0,0) + i\sin[\sigma F(h,k)\Delta z]\delta(h,k) \qquad 2.16$$

Thus A and B can be written as:

$$A = \cos[\sigma F(h,k)\Delta z] \quad B = i\sin[\sigma F(h,k)\Delta z] \qquad 2.17$$

After the beams have passed through n layers of atoms in the crystal, the primary beam amplitude, A_P, is:

$$\begin{aligned} A_p &= \frac{1}{2}\left[(\cos(\sigma F(h,k)\Delta z) + i\sin(\sigma F(h,k)\Delta z))^n + (\cos(\sigma F(h,k)\Delta z) - i\sin(\sigma F(h,k)\Delta z))^n\right]\exp\{(n-1)i\delta\} \\ &= \frac{1}{2}\left[(\exp i\sigma F(h,k)\Delta z))^n + (\exp\{-i\sigma F(h,k)\Delta z)\})^n\right]\exp\{(n-1)i\delta\} \\ &= \frac{1}{2}[\cos(n\sigma F(h,k)\Delta z) + i\sin(n\sigma F(h,k)\Delta z) + \cos(n\sigma F(h,k)\Delta z) - i\sin n(\sigma F(h,k)\Delta z)]\exp\{(n-1)i\delta\} \\ &= \cos\{\sigma F(h,k)t\}\exp\{(n-1)i\delta\} \end{aligned}$$

2.18

where t = nΔz is the crystal thickness. The diffracted beam amplitude, A_D, can be expressed as:

$$A_D = i\sin\{\sigma F(h,k)t\}\exp\{(n-1)i\delta\} \qquad 2.19$$

As the electron beam passes through the crystal, the primary beam will gradually diminish and the diffracted beam will increase. This will continue until a limit is reached where the primary beam is no longer present at the exit face of the crystal. This point is known as the extinction distance and occurs when t = π/2σF(h,k). Under these conditions the diffracted beam amplitudes are related to the F(h,k)'s by a very complex relationship.

This approach can be extended to the situation where the incident beam is not inclined to the planes and then to the situation where many beams are dynamically scattered.

2.2.2 HRTEM

The products were studied using the JEOL JEM-2000FX and JEOL JEM-2011 electron microscopes. A small amount of product was ground to a fine powder using a mortal and pestle. A few drops of acetone were added to form a suspension of particles. Using a Pasteur pipette a drop of the suspension was placed on a carbon film supported on a copper grid. The sample was inserted into the microscope and examined using an accelerating voltage of 200 kV. The electron source in the JEM-2000FX microscope is a tungsten filament, whereas in the JEM-2011 microscope it is a LaB_6 crystal.

An electron microscope essentially consists of an electron source and a group of electromagnetic lenses. Electrons from either a thermionic source, such as a tungston wire or LaB_6 crystal, or a field emission gun are accelerated across a potential difference, in the microscopes used this value was 200 kV. A diagram of a TEM is shown in Fig. 2.6. The important factors in an electron source are brightness (how much radiation is emitted) and coherence (how parallel the beam is)[114].

The condenser lenses then focus the electrons into a parallel beam and the beam strikes the very thin sample mounted on a perforated carbon film. The electron beam reacts with the sample whereupon the transmitted and diffracted electrons recombine and are focused by the objective lens. The beams then diverge and are focused by the projector lens, hitting a fluorescent screen resulting in a structural image. The image can be recorded on a photographic plate or be captured by a CCD camera.

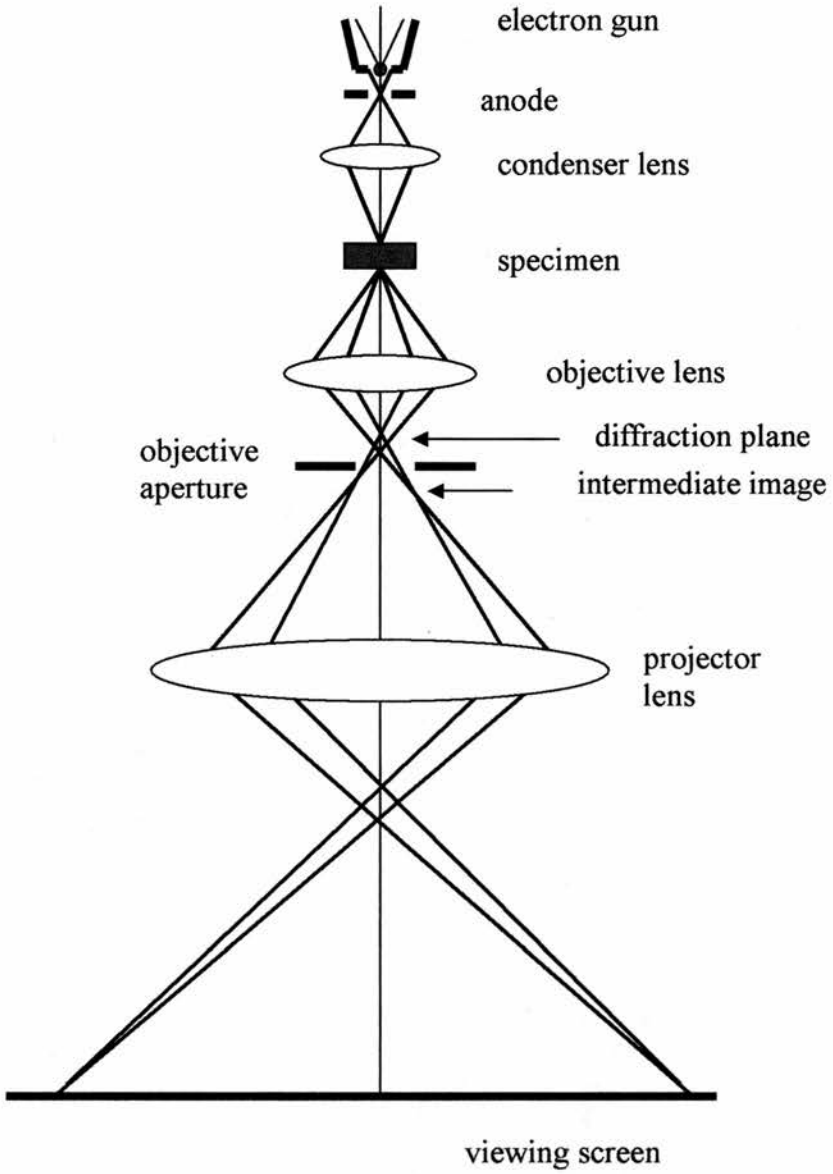

Fig. 2.6 A schematic diagram of a TEM.

An electron leaves the filament with high potential and thermal kinetic energy, and arrives at the anode with high kinetic energy and no potential energy. The principal of energy conservation applied to an electron of charge –e, mass m and velocity v using the De Broglie relationship, $p = mv = \frac{h}{\lambda}$ gives

$$eV = \frac{1}{2}mv^2 = \frac{p^2}{2m} = \frac{h^2}{2m\lambda^2} \qquad 2.20$$

where p is the electron momentum and h is Planck's constant. Thus,

$$\lambda = \frac{h}{\sqrt{2meV}} \qquad 2.21$$

When the accelerating voltage, V, is very large, v is comparable with the speed of light, c, and the relativistic corrections in mass of the electron and in accelerating voltage should be taken into account,

$$\lambda = \frac{h}{\sqrt{2meV_r}} = \frac{h}{\sqrt{2m_o eV_o\left(1+\frac{eV_o}{2m_o c^2}\right)}} \qquad 2.22$$

where m_o is the electron rest mass and V_o is the accelerating voltage before the relativistic correction. $V_r = V_o + \left(\frac{e}{2m_o c^2}\right)V_o^2$ is often called the relativistic accelerating voltage. Therefore with an accelerating voltage of 200 kV, the electron wavelength λ = 0.0251 Å.

Spherical aberration

The resolution of the image in HRTEM is partly dependant on the optical characteristics of the objective lens. This lens recombines the diffracted beams from the sample to form the initial image. Spherical aberration is the most significant of these factors, it introduces a phase difference in the individual diffracted beams and this can lead to confusion in the contrast when the real image is synthesised[114].

Spherical aberration is caused when rays at different distances from the optic axis fail to converge to the same point. This effect can be countered to some extent by defocusing the beam. If we consider a perfect lens the two rays should intersect at a point on the Gaussian image plane, however if spherical aberration is present the non-axial ray reaches the Gaussian image plane at an amount, Δr, from the optic axis, where Δr is the radius of the disc of least confusion, given by:

$$\Delta r = MC_s\alpha^3 \qquad 2.23$$

where M=b/a is the magnification of the lens and C_s is the coefficient of spherical aberration and α is the scattering angle between the two rays.

The angular deviation of the non-axial ray caused by the spherical aberration can be expressed as:

$$\varepsilon_s = \frac{\Delta r}{b} = \frac{MC_s\alpha^3}{b} \approx \frac{C_s R^3}{F^4} \qquad 2.24$$

where F is the focal length of the lens. This effect is illustrated in Fig. 2.7.

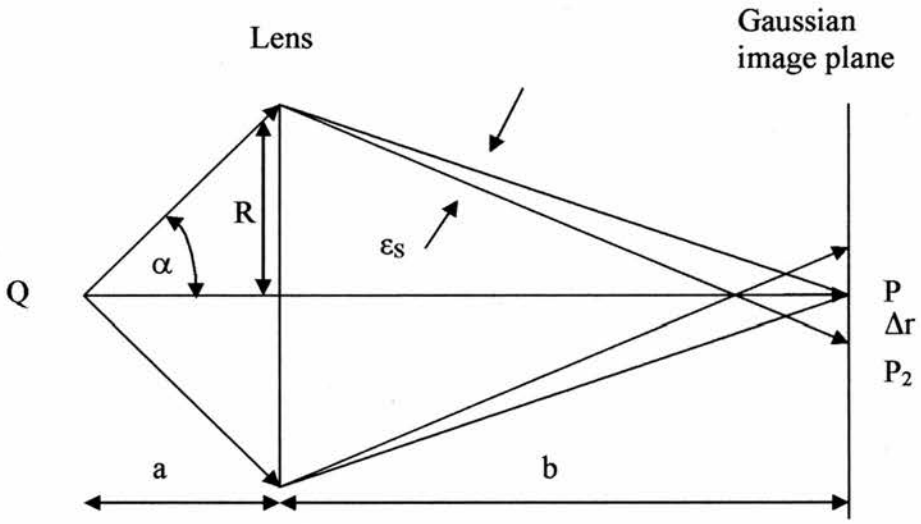

Fig. 2.7 Ray Paths in a Lens subject to Spherical Aberration.

If we now consider two non-axial rays, shown in Fig. 2.8, one at a distance R from the lens centre and the other at a distance of R +dR then the path difference, ds, arises from the extra deviation ε_s and is given by:

$$ds = \varepsilon_s dR \qquad 2.25$$

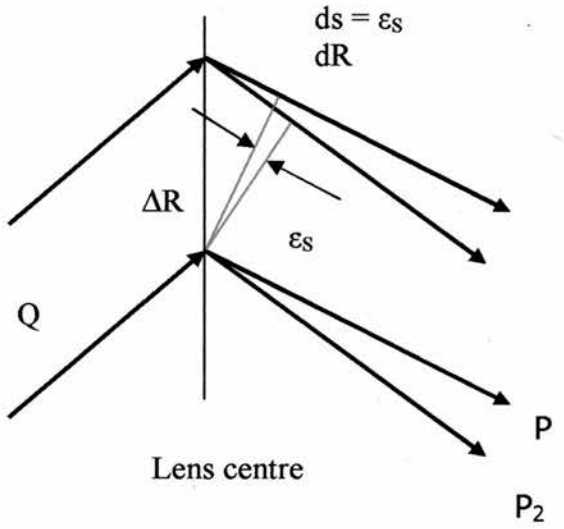

Fig 2.8 Ray Paths for two non-axial rays in a lens subject to spherical aberration.

The total path difference $W_s(\alpha)$ between the non-axial ray and one along the optic axis is:

$$W_s(\alpha) = \frac{2\pi}{\lambda}\Delta = \frac{2\pi}{\lambda}\int_0^R ds = \frac{2\pi}{\lambda}\int_0^R \frac{C_s R^3}{F^4} dR = \frac{2\pi}{\lambda}\frac{1}{4}\frac{C_s R^4}{F^4} = \left(\frac{2\pi}{\lambda}\right)\frac{1}{4} C_s \alpha^4 \qquad 2.26$$

Defocus effect

Increasing the focal length by an amount ΔF causes a non-axial ray to be brought to the optic axis further from the specimen, increasing the image distance, Δb. This effect is shown in Fig. 2.9. The angular deviation, ε_f, is given by:

$$\varepsilon_f = \frac{\Delta b \beta}{b} = \frac{\Delta b R}{b^2} = \frac{\Delta F R}{F^2} \qquad 2.27$$

The phase difference between axial and non-axial rays is:

$$W_s(\alpha) = \frac{2\pi}{\lambda}\int_0^R \varepsilon_f dR = \frac{2\pi}{\lambda}\int_0^R \frac{\Delta F R}{F^2} dR = \left(\frac{2\pi}{\lambda}\right)\frac{1}{2}\Delta F \alpha^2 \qquad 2.28$$

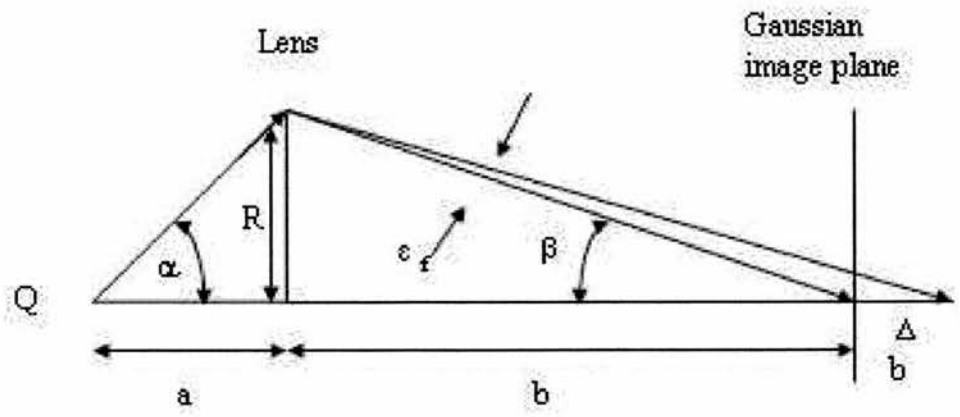

Fig. 2.9 Ray paths in a lens with increased focal length.

As spherical aberration and the defocus effect have opposite signs, the complete phase shift is given by :

$$\chi(\alpha) = \frac{2\pi}{\lambda}\left[\frac{1}{2}\Delta F\alpha^2 - \frac{1}{4}C_s\alpha^4\right] \qquad 2.29$$

which is the Scherzer's formula. If S is defined such that $|S| = 2\sin\theta/\lambda \approx \alpha/\lambda$ when α is small, then:

$$\chi(S) = \frac{2\pi}{\lambda}\left[\frac{1}{2}\Delta F\lambda^2|S|^2 - \frac{1}{4}C_s\lambda^2|S|^4\right] \qquad 2.30$$

$\chi(S)$ is normally referred to as the Phase Contrast Transfer Function (PCTF). This function describes the way in which the phase shifts are introduced into the diffracted beams and converts the phase difference into an amplitude difference in the image intensity. This introduces contrast into the image.

Since $\chi(S)$ depends on ΔF, the image contrast will consequently change with ΔF. In an image formed from a series of fringes the relative amplitudes of the fringes will be determined not only by the structure but also by the lens defocus. If the lens defocus causes reversal of the contrast of some fringes the image may not look like the specimen producing it. The terms in the PCTF involving ΔF and C_s have opposite

signs, thus ensuring that for a limited range of S values there will be a defocus position where they approximately cancel. This defocus is referred to as the Scherzer focus. All beams lying within the range from S_1 to S_2 will be imaged with approximately the same relative contrast. The spacing corresponding to S_2 is called the interpretable resolution limit. The form of sin $\chi(S)$ at the Scherzer focus is shown in Fig.2.10.

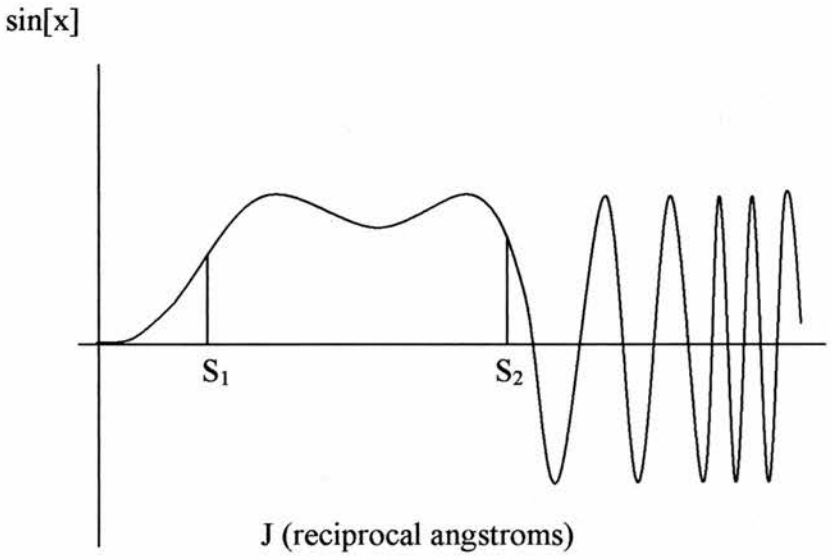

Fig. 2.10 sin[x] part of phase contrast transfer function at the Scherzer focus (ΔF = -380 Å) for a microscope operating at 200 kV with C_s = 0.41 mm.

Chromatic aberration and beam divergence

Two other important factors effect resolution, these are chromatic aberration and beam divergence. Chromatic aberration is caused because the focal length of the magnetic objective lens is dependent on the energy of the electrons. The electron beams that pass through the sample are not monochromatic, they have a range of energies and wavelengths. The primary cause is the fluctuation in the energy of electrons leaving the filament. This arises from slight oscillation in the accelerating voltage (ΔV) and variations in the electron energies owing to thermal effects (ΔE). Both of these effects

cause minor variations in scattering angle for a given diffracted beam and also change the focal length of the objective lens. The second cause of chromatic aberration lies in fluctuations in the current of the objective lens coils (ΔI). This also changes the focal length of the lens. Finally there are energy loss processes in the specimen. These are not normally too serious because electrons which have suffered a diminution in energy by, for example, giving rise to X-ray emission, are then emitted incoherently by the specimen and are assumed to form a constant background scattering. Consequently, the three effects give a focal spread for the microscope, δF, which is defined as:

$$\delta F = C_C\left[\left(\frac{\Delta V}{V}\right)^2 + \left(\frac{\Delta E}{V}\right)^2 + 2\left(\frac{\Delta I}{I}\right)^2\right]^{1/2} \qquad 2.31$$

where C_C is the coefficient of chromatic aberration, V the accelerating voltage and I the objective lens coil current. Due to these fluctuations in electron energy for any given value of defocus, ΔF, the real value will be $\Delta F \pm \delta F$.

Beam divergence, or spatial incoherence, occurs because the filament is not a point source and consequently the beam incident upon the object is never exactly parallel. The electron beam tends to be focused onto the specimen in order to produce bright enough illumination, therefore when the beam passes through the condenser aperture the aperture is incoherently illuminated. This creates a cone of illumination and the image intensity is an average over a small circular range of beam inclination angles, or an average over a range of δS values.

The effect of this incoherence on the image can be calculated by integrating over the range of illumination angles. This means that for different values of defocus the interpretable region of the overall transfer function (which incorporates the beam divergence and chromatic aberration envelope functions) will be at different values of S. The result of this is that at higher values of defocus finer detail can be observed in

the image. The overall affect of the chromatic aberration and beam divergence envelopes on the PCTF is shown in Fig 2.11.

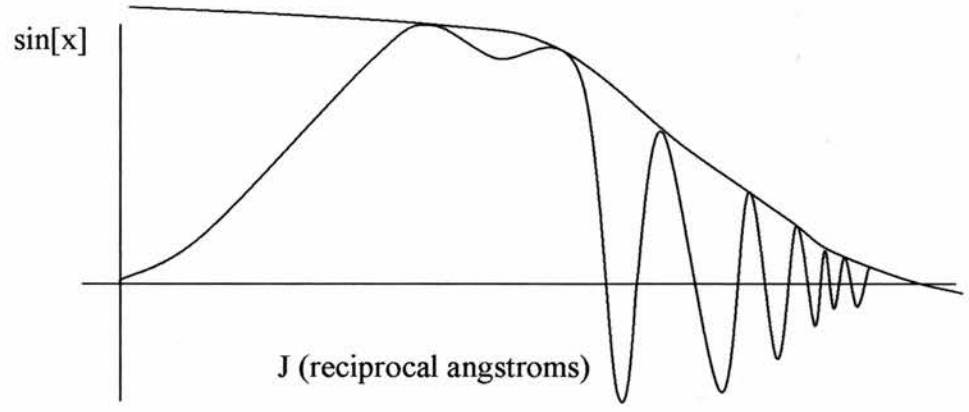

Fig. 2.11 sin[x] part of the phase contrast transfer function with the chromatic and beam divergence envelopes (ΔF = -380 Å) for a microscope operating at 200 kV with C_s = 0.41 mm.

2.2.3 EDX

The composition of the samples was investigated using energy dispersive X-ray spectroscopy (EDX). EDX can analyse individual crystals and can therefore detect impurities that may be present in concentrations too low to be detected by powder X-ray diffraction. Energy dispersive X-ray spectroscopy measurments were carried out on a JEOL 2010 electron microscope using an Oxford Link EDX system and on a JEOL 5600 scanning electron microscope using an Oxford Inca EDX system.

X-rays are generated by bombarding the sample with a beam of high energy electrons. The electrons in an atom occupy different quantum levels, each having a definite energy. Starting with the shell closest to the nucleus these shells are termed K, L, M, N etc. Excitation of an electron can cause it to be ejected from the atom, causing an electron from a higher level to drop down to fill the hole. Due to the laws of

conservation of energy a quantum of radiation will be emitted from the atom corresponding to the energy difference between the levels. These quanta of radiation (x-rays) are detected and as each atom has its own characteristic energy levels, serve as a fingerprint to identify elements present within a crystal and the composition of the sample can be determined. The X rays are detected and displayed as a spectrum against energy level.

The energies of the emitted X-rays are characterised according to which shells are involved. The notation used is as follows:

K_α corresponds to a L to K transition

K_β corresponds to a M to K transition

There are several technical problems that could affect the quality of an EDX spectrum. The most important of these is the absorption problem. If the X-rays that are detected are generated deep in a thick crystal they could be absorbed by the rest of the crystal. The absorption is dependent on the wavelength, which is characteristic of each element misleading data can be observed. Absorption may also occur from crystals near the area under examination, causing a lowering of intensities which also leads to misleading composition results. The specimen grid contains grid bars, which also cause absorption. The grid bars also generate X-rays by fluorescence. These effects can be avoided or reduced to a minimum by collecting spectra from relatively thin crystals (around 30 nm) and selecting a good examination area in a particle positioned away from the grid bars, thus limiting re-absorption.

To analyze a spectrum the area of each peak must be compared. Spectra from standards of known composition are then compared to the experimental data to obtain composition information. A good approximation is that for a thin sample (<100 nm) the concentration ratio of two types of atoms, x and y, can be written:

$$\frac{C_x}{C_y} = K_{xy} \frac{I_x}{I_y} \qquad 2.32$$

where I_x and I_y are the intensities of the main X-ray emission lines and K_{xy} is a constant obtained from a standard containing x and y. With the experimental conditions well controlled the accuracy of the EDX results is still low ($>\pm$ 5% on elemental ratios). Therefore it is necessary to analyse many particles, 20 to 30, and take an average value of the results to obtain elemental compositions.

2.2.4 SEM

A small amount of sample is crushed into a fine powder using a mortar and pestle. A small piece of adhesive carbon film is stuck on the mount and the fine powder applied to the other side of the film. Excess powder is blown off using pressurised inert gas, leaving a fine dusting of sample on the film. The mounted sample is placed in the specimen holder and using the JEOL 5600 SEM software digital images are obtained.

When an electron beam hits a sample, electrons are ejected from atoms, these secondary electrons have a lower energy than the incident beam. It is these electrons, as well as back scattered electrons are of interest in scanning electron microscopy (SEM). The technique is used to investigate surface morphology. Magnetic contrast and local electrostatic potential can also be seen using SEM. A diagram of a SEM is shown in Fig. 2.12.

The intensities and energies of these electrons carry information about the morphology of the surface under investigation. As can be seen from Fig. 2.13, the electrons from D are more likely to be detected than A, thus giving a morphology contrast in the image. Magnetic contrast can be observed if, for example, one part of the sample is ferromagnetic and another is non-ferromagnetic, as more electrons will

escape from one type than the other, giving a contrast. Different crystal orientations may also result in a contrast. The number of secondary electrons leaving the specimen surface is different from the number of electrons striking it in the primary beam. For the sample to remain at equipotential the extra charge must pass through to the earth plate. If the specimen is an insulator this cannot happen and the sample charges. This effects image quality, to remedy it the sample can be coated in a conducting material or the voltage can be altered to give better images. Coating a sample can be problematic. If the coating is too thick the detailed structure of the surface can be lost, and if the sample has many steps coating may not be complete, which will still give charging problems.

The principal of SEM is similar to that of a light microscope. The advantages of SEM include great depth of focus and much higher resolution.

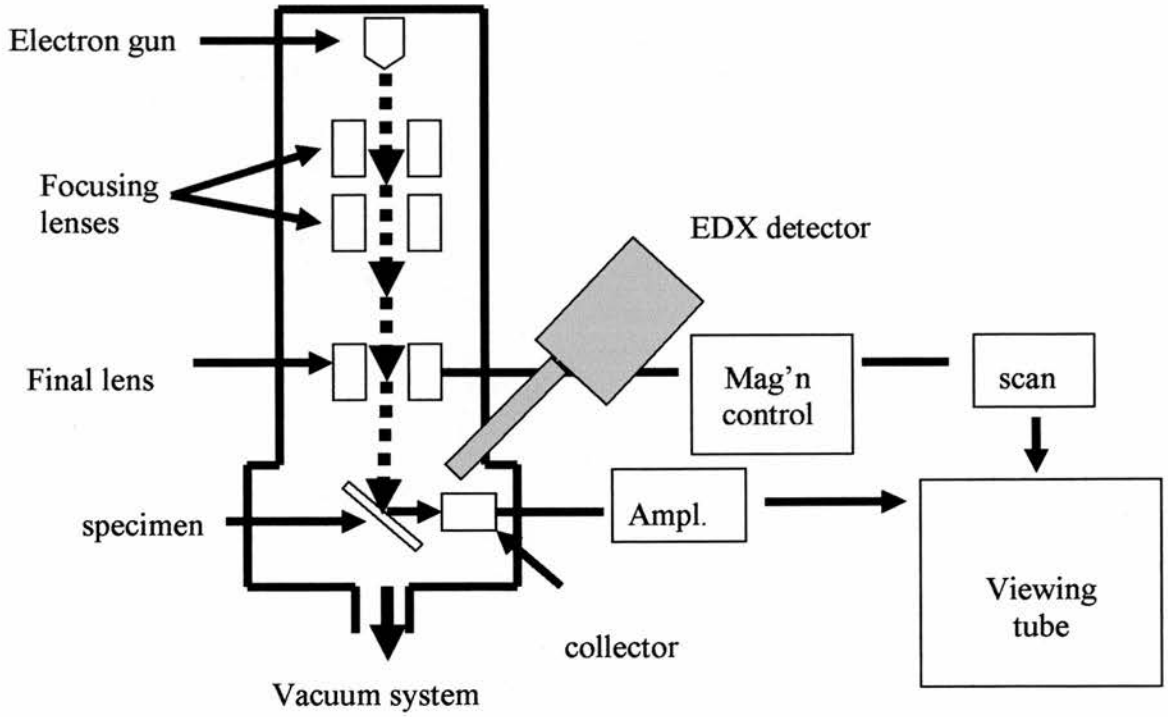

Fig. 2.12 Diagram of SEM

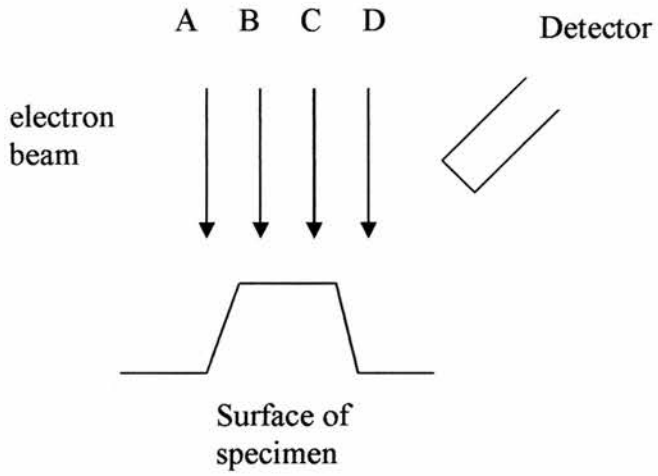

Fig. 2.13 SEM image formation

The picture element is the region on the specimen to which the beam is addressed and from which information is transferred to a single spot on the cathode ray tube (pixel). The minimum cathode ray tube spot size diameter is usually 0.1mm.

$$\text{Picture element diameter} = \frac{0.1mm}{magnification} \qquad 2.33$$

When the magnification is increased the picture element diameter decreases. Hollow magnification may occur when the magnification is increased and no additional information can be obtained due to overlapping of picture elements. The SEM image will appear in focus if the sampling volume is smaller in diameter than the picture element. Resolution of an image is affected by beam size.

The depth of field depends upon the electron beam divergence angle, which is defined by the diameter of the objective lens aperture and the distance between the specimen and the aperture. Depth of field is increased by reducing the beam divergence angle, which can be done by increasing the working distance or decreasing the aperture

diameter, or by decreasing the magnification. The depth of field is the area of the image in effective focus, as shown in Fig. 2.14.

$$D/2 = r/\alpha \qquad 2.34$$

Combining equations 2.33 and 2.34 gives:

$$D = \frac{2r}{\alpha} = \frac{0.2mm}{\alpha M} \qquad 2.35$$

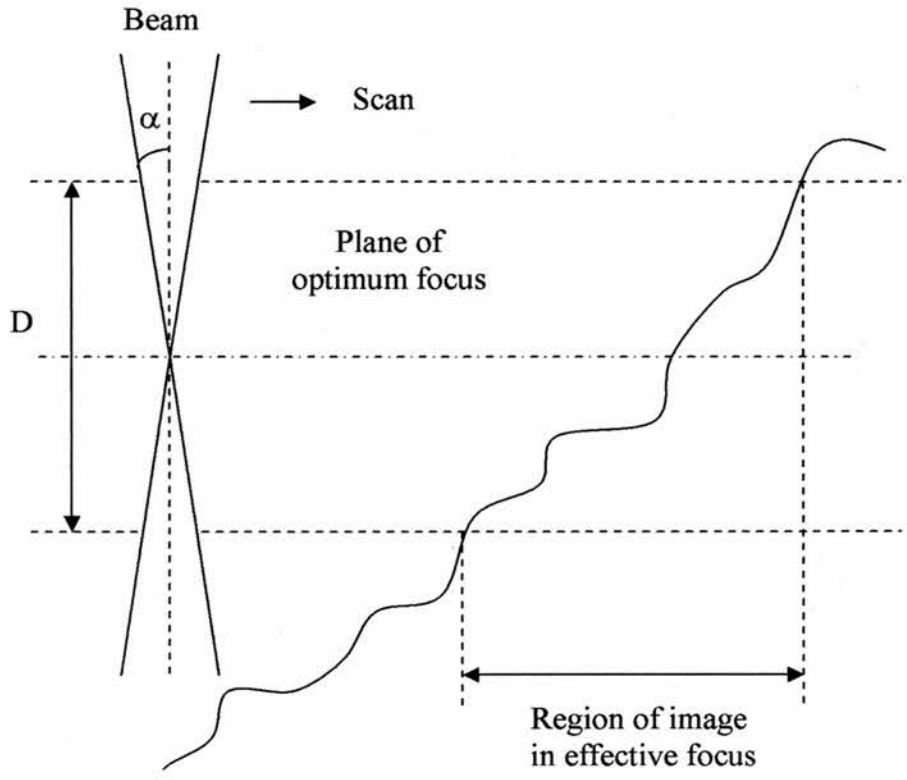

Fig. 2.14 Depth of field in SEM.

2.2.5 Powder XRD

Powder X-ray diffraction is an invaluable method for the characterisation of polycrystalline material. It is a routine method of characterisation for powder specimens as each compound has a unique powder pattern that can be used as a fingerprint allowing easy identification of crystalline phases.

A diffraction pattern is obtained from crystalline samples according to the Bragg's Law:

$$n\lambda = 2d\sin\theta \qquad 2.36$$

Peaks are obtained at each allowed d value (according to Bragg's Law), depending on the crystal structure. Diffraction patterns represent scattering from parallel planes and depend on type and location of atoms in the unit cell. A schematic diagram is shown in Fig. 2. 15.

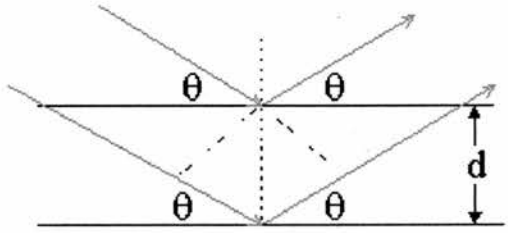

Fig. 2.15 X-Ray diffraction.

In a powder X-ray diffraction experiment the angle, θ, is altered and the resultant intensities plotted in the form of a powder pattern.

Symmetry within the structure can lead to systematic absences which aid the determination of space group and therefore the determination of structure.

When an incident beam of X-rays is diffracted by a three-dimensional body the phase and amplitude of the X-rays is altered, as shown in Fig. 2.16.

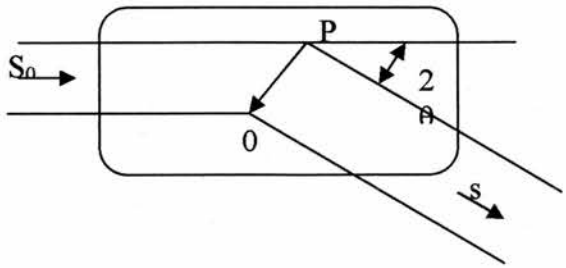

Fig. 2.16 Diffraction from a three-dimensional body

The amplitude of the diffracted beam in the direction **s** can be expressed by setting an arbitary origin at O, and considering a point P a distance and direction **r** from O. The path lengths which the diffracted beam must travel are dependant on whether the beam is diffracted from point O or P. In vector notation the path difference, δ, is given by:

$$\delta = \mathrm{r.s}_0 - \mathrm{r.s} \qquad 2.37$$

where $\mathbf{s}_0$ is the incident beam and **s** is the diffracted beam. There will also be a phase difference between the beams diffracted at different points due to the difference in path lengths. This phase difference is:

$$\frac{2\pi\delta}{\lambda} = \left(\frac{2\pi}{\lambda}\right)(\mathrm{r.s} - \mathrm{r.s}_0) \qquad 2.38$$

The amplitude of the beam (A) diffracted by a volume element dVr at P is:

$$A = \psi_0(\mathrm{r})\exp\left(\frac{2\pi i(\mathrm{r.s} - \mathrm{r.s}_0)}{\lambda}\right)\mathrm{dV_r} \qquad 2.39$$

where $\psi_0(\mathrm{r})$ is the transmission function of the object, which describes the amount of radiation scattered by the object.

Defining a scattering vector, **S**, as:

$$\mathrm{S} = \frac{1}{\lambda}(\mathrm{s} - \mathrm{s}_0) \text{ where } |\mathrm{S}| = \frac{2\sin\theta}{\lambda} \qquad 2.40$$

as shown in the vector diagram Fig. 2.17:

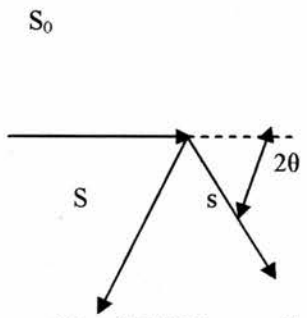

Fig. 2.17 Vector diagram

Rewriting equation 2.39, we obtain:

$$A(S) = \psi_0(r)\exp 2\pi i r.S dV_r \qquad 2.41$$

summing this expression over all volume elements to get the total diffracted amplitude:

$$\Psi(S) = \sum \psi_0(r)\exp(2\pi i r.S).dV_r \qquad 2.42$$

If dVr becomes infinitely small then the summation can be replaced by an integral.

$$\Psi(S) = \int \psi_0(r)\exp(2\pi i r.S).dV_r \qquad 2.43$$

This is a Fourier Transform function that can be written as:

$$\Psi(S) = FT[\psi_0(r)] \qquad 2.44$$

This means that the total diffracted amplitude, $\Psi(S)$, is the Fourier Transform of the transmission function, $\psi_0(r)$, of the sample. The transmission function can be expressed in terms of the electron density by which the beam is diffracted., because the X-ray beam is diffracted by the electrons in the atom, therefore:

$$\psi_0(r) = \exp i\sigma\rho(r) \qquad 2.45$$

where σ is the interaction parameter and $\rho(r)$ the electron density. Due to the relatively weak interaction of X-rays with the electrons in the atoms this equation can be simplified. By expanding the exponential we need only consider the first two linear terms, the higher order terms can be disregarded. This is known as the kinematic approximation and is valid only if the scattering is very weak. Therefore:

$$\psi_0(r) \approx 1 + i\sigma\rho(r) \qquad 2.46$$

Considering how the phase change varies with **r**, we can define a modified diffraction amplitude as:

$$F(S) = \frac{\Psi(S)}{i\sigma} = FT[\rho(r)] \qquad 2.47$$

$$F(S) = \int \rho(r)\exp(2\pi i\, r.S).dV_r \qquad 2.48$$

Or expressed in modulus argument form:

$$F(S)=|F(S)|\exp i\Phi(S) \qquad 2.49$$

In a powder X-ray diffraction experiment the angle, θ, is altered and the resultant intensities plotted in the form of a powder pattern. The intensity is the square of the modulus of the diffracted beam:

$$I(S)=|F(S)|^2=|FT[\rho(r)]|^2 \qquad 2.50$$

This information gives us the modulus but not the sign, or phase part of F(S). This is known as the crystallographic phase problem. The crystal structure can only be solved if we know both the modulus and the phase terms. This is normally done by direct methods. The phase is determined directly from the intensities by statistical methods.

In this project, all the X-Ray powder diffraction patterns were collected on the Philips –1 machine using Cu K α wavelength 1.54A

2.2.6 Raman Spectroscopy

Raman spectroscopy measures the vibrational energies of molecules[115]. For a transition to be Raman active, there must be a change in polarizability of the molecule. The size of the induced dipole, μ, depends on the magnitude of the applied field, E, and on the ease with which the molecule can be distorted:

$$\mu=\alpha E \qquad 2.51$$

When the photons from the incident beam collide with the sample molecules, radiation is scattered. If this radiation has a frequency lower than that of the incident beam it is referred to as Stokes' radiation. The radiation of a higher frequency is referred to as anti-Stokes' radiation. Stokes' radiation is generally more intense, however the total

radiation scattered is small so sensitive apparatus is needed. Raman spectra were recorded on a Perkin-Elmer System 2000 FT/IR/Raman Spectrometer.

Chapter 3 Trititanate Nanotubes

3.1 Trititanate nanotubes from TiO_2

The aim of this series of experiments is to investigate the mechanism of formation of trititanate nanotubes from the hydrothermal reaction of rutile TiO_2 and 10 M NaOH solution. The conditions used were 140 °C for 72 h. Nanotubes have been shown to form from 110 °C up to 190 °C. Higher temperatures and higher NaOH concentration produces nanowires. TiO_2-B nanowires were produced at 170 °C and 15M NaOH solution. As the temperature is raised above 170 °C the yield of tubes is reduced. If a temperature of 170 °C is used the conversion to nanotubes is around 60%. The conditions used are by no means the optimum condition for nanotube production, but are adequate for the mechanistic experiments.

To investigate the formation mechanism experiments were run using a 1:2.5 molar ratio of TiO_2 to NaOH, which was in a 10 molar solution with water.

Reactions were run at two hour intervals from 2 to 24 hours and the products were subsequently viewed using the JEOL 2000-FX and JEOL 2011 microscopes. It has been found previously that a high yield of nanotubes can be produced after 72 hours of reaction. After this time most of the material has been converted from rutile to nanotubes without leaving many clues as to the mechanism of reaction. The reaction was stopped after short periods of time using the same conditions and reactant amounts to investigate the path of the reaction.

The samples showed 4 phases present:

In the sample reacted for 2 hours the material was almost exclusively polyhedral rectangular-like titanium dioxide starting material, shown in Fig. 3.1. The structure of the starting material has been confirmed as rutile by XRD pattern (Fig. 3.2), a ceramic crystalline material which consists of distorted hexagonally close-

packed oxide layers in which half of the octahedral holes are filled by oxygen. The reaction time was not long enough for any substantial reaction to have taken place. This is to be expected as the reaction takes 72 hours to produce a good yield. As the reaction is done in a static autoclave the reaction will require a period to reach the temperature of the oven and for the reactants to become mobile, and after 2 hours no significant reaction had occurred.

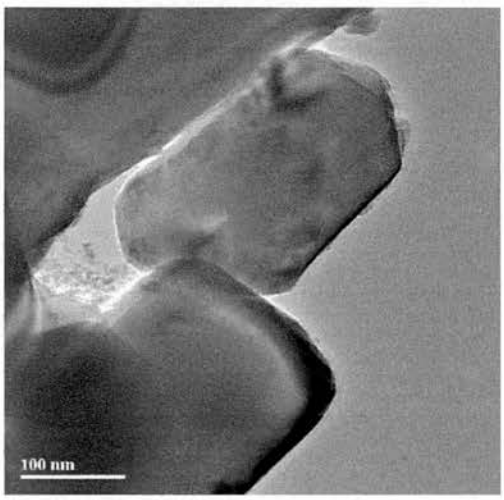

Fig. 3.1 TEM image of the material present after 2 h reaction time, crystalline TiO_2.

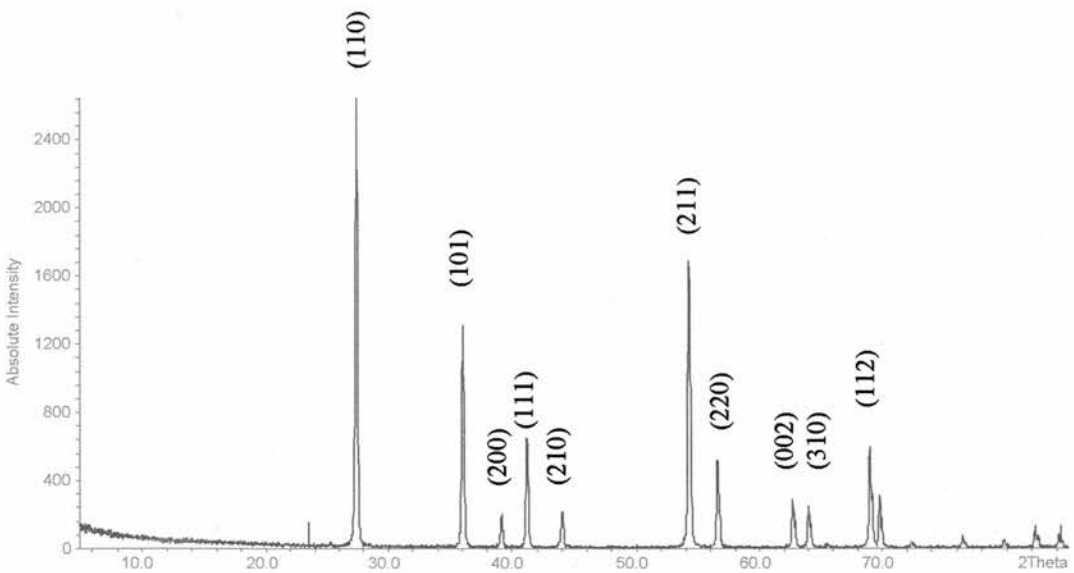

Fig. 3.2 XRD of starting material, indexed as rutile TiO_2.

After 4 hours the product was mainly unreacted starting material, with small areas of amorphous material present. This amorphous material contains sodium, oxygen and titanium in a disordered state, shown by EDX results on both scanning (Fig. 3.3) and transmission electron microscopes. An image of the amorphous material is shown in Fig. 3.4.

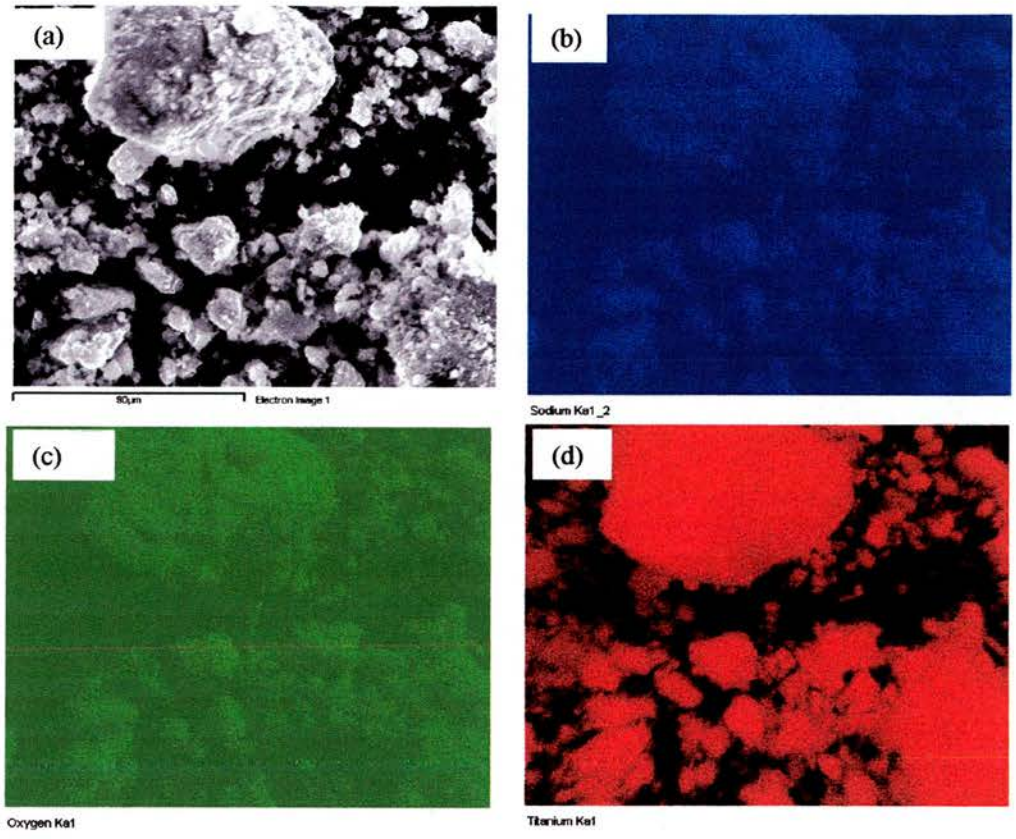

Fig. 3.3 SEM elemental mapping of a sample of TiO_2 reacted for 4 h with 1o M NaOH. The image is shown in (a), with the sodium map shown in (b), the oxygen map in (c) and the titanium map in (d).

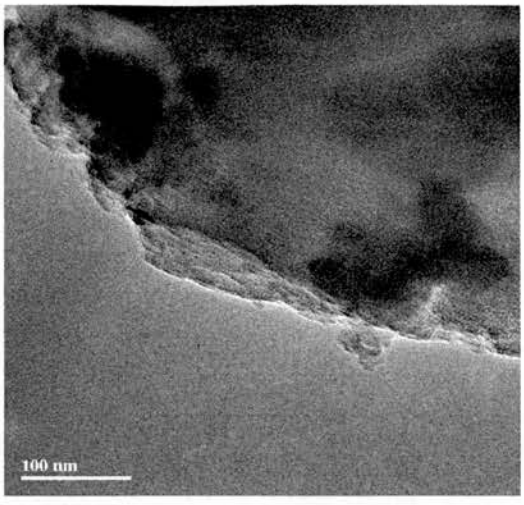

Fig. 3.4 TEM image of amorphous material from a specimen of TiO_2 after 6 h reaction with NaOH.

In an attempt to show the nature of the amorphous material, a sample was washed excessively with water. The sodium in the amorphous phase leached out and was washed out along with the excess base. This shows that the sodium is not bound to the Ti or O in the amorphous phase and probably exists as free ions, weakly physically attached to the amorphous material. When a sample is washed for a shorted period of time Na ions can be seen in the amorphous phase. The harsh reaction conditions of high temperature, pressure and NaOH solution concentration result in the breaking some of the strong Ti-O bonds to produce fragments of material containing TiO_6 octahedra and results in a phase containing titanium, oxygen and sodium. The hydrogen present could not be detected by EDX.

The sample heated for 6 hours still contained a large amount of crystalline material- greater than 50%- and a large amount of amorphous material, in areas of varying size. This sample also contained a small percentage of nanotubes, which were randomly orientated, and in many cases attached to amorphous material. It is believed that this is due to the high viscidity of the tubes, which are attached to each other in high yield samples. Thin plates of material of varying layer thickness were also seen in

this sample. The difference in transparency to the beam of these plates showed the different layer thickness.

As the reaction time increased to 24 hours- a third of the overall reaction time- the percentage of crystalline starting material decreased, with the percentage of nanotubes increasing. The amorphous material and plates were also present in all of these samples.

The next stage of the reaction is the formation of thin plates of trititanate, $H_2Ti_3O_7$, which are produced when single layers extrude out of the amorphous phase and couple together to form plates of varying thickness, shown in Fig. 3.6. The observed d spacing of 1.88 Å is indexed as the (020) plane of $H_2Ti_3O_7$. Fragments of titanate present in the amorphous second phase may couple together through electrostatic interactions, with the negatively charged plates held close together by positively charged sodium ions, the end groups of these fragments may link together through covalent bonding to form sheets of trititanate. These layers of trititanate couple together to form thin plates, which are seen in the reaction mixture. Due to the high concentration of sodium ions in the solution, there may be sodium ions intercalated between the layers. From the thin plates single layers peel off to form nanotubes. Titanium dioxide and titanates all exhibit similar structures, being based around TiO_6 octahedra. In TiO_2 these TiO_6 units are linked by two edge-sharing octahedra and eight corner-sharing octahedra in the case of anatase with four edge-sharing octahedra and four corner-sharing octahedra in the case of rutile. In $H_2Ti_3O_7$ the structure contains stepped sheets of three edge sharing TiO_6 units, which is shown in Fig. 3.5. The stepped structure is created through corner sharing. Trititanate plates recrystallising from the amorphous phase show that some of the bonds in TiO_2 are

broken, but that the building blocks of titanate related structures are present, and that under the reaction conditions the material is re-ordered into $H_2Ti_3O_7$.

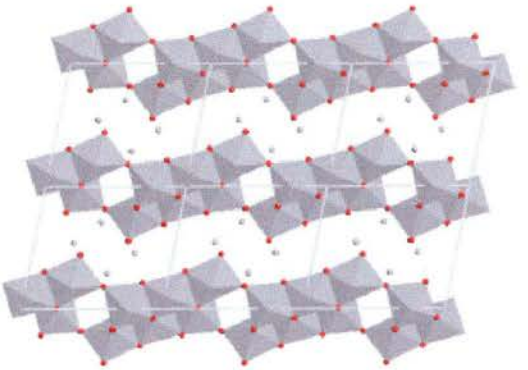

Fig. 3.5 Structure model of $H_2Ti_3O_7$. Grey spheres are H^+ ions, red spheres O atoms and grey polyhedron are TiO_6 octahedron.[84]

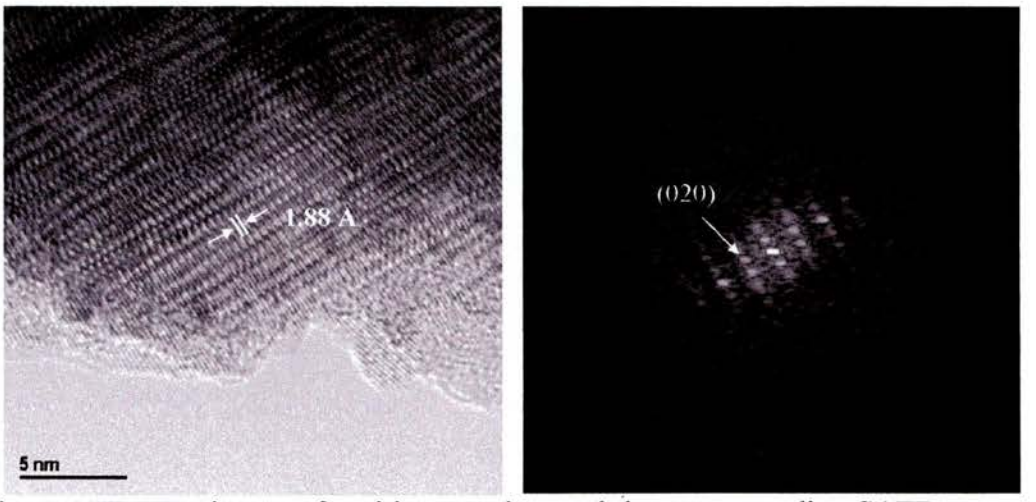

Fig. 3.6 HRTEM image of a trititanate plate and the corresponding SAED pattern.

The final step in the reaction is the production of nanotubes from thin plates. A single nanotube is shown in Fig. 3.7. The structure of the nanotubes has been shown to be trititanate by XRD, Raman and HRTEM. EDX done on a single nanotube has shown that the nanotubes contain only Ti and O and no Na. Hydrogen can not be detected by EDX. The nanotube phase is a mixture of monoclinic $H_2Ti_3O_7$, with a = 1.603, b = 0.375, c = 0.919 nm and $\beta = 101.45^{\circ}$, and unreacted rutile TiO_2 as shown by XRD in

Fig. 3.8. The sodium ions present in the reaction can be washed out of the tubes without the loss of tubular structure. Therefore sodium is not necessary for the stabilisation of tubular structure; they just balance the charge from the $Ti_3O_7^{2-}$ plates.

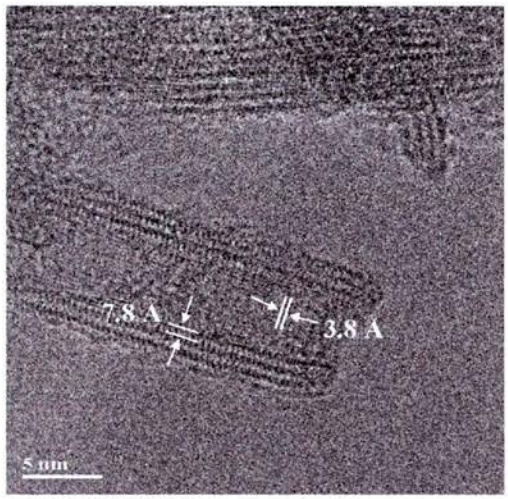

Fig. 3.7 HRTEM image of trititanate nanotube.

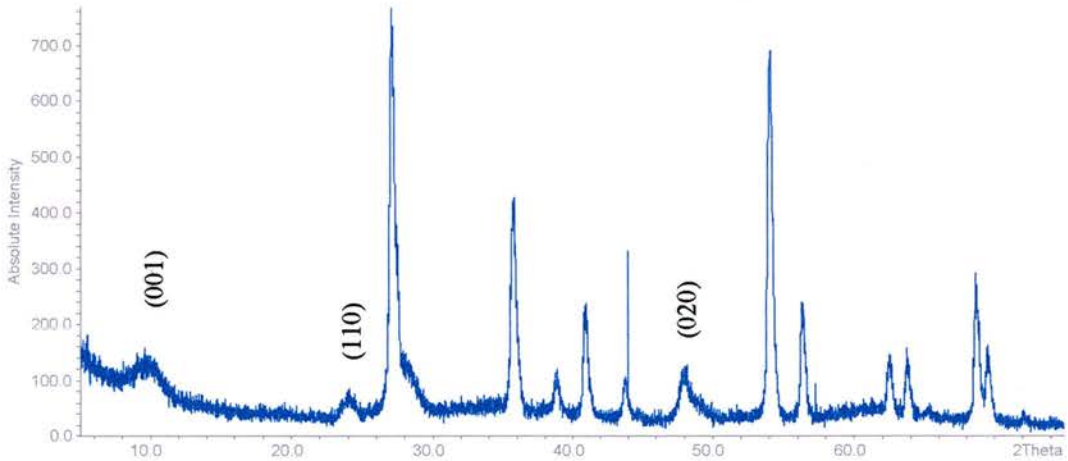

Fig. 3.8 XRD pattern of the nanotube product indexed as $H_2Ti_3O_7$. The other peaks are rutile TiO_2.

The nanotubes have a scroll structure, shown by an end on image of a tube, Fig. 3.9. The number of shells in a single tube is ordinarily 4, with an outer diameter of 8 nm and an inner diameter of 4.5-5 nm. The tubes are hollow, with an intershell spacing of 0.78 nm that corresponds to the (200) spacing in $H_2Ti_3O_7$. The d spacing measured

along the tube axis is 0.38 nm, which corresponds to the (010) plane, which is systematically absent in the XRD. This is evidence that the tubes are composed of $Ti_3O_7^{2-}$ sheets scrolled along the [001] direction. The range in diameter and number of shells is small, as can be seen from Fig.3.10. This narrow distribution suggests that there is a specific mechanism governing the size of the nanotubes. Due to the scroll structure of the tubes the number of layers on either side may differ by one. The nanotubes had a wide range of lengths, mainly in excess of 200 nm and up to a few micrometers.

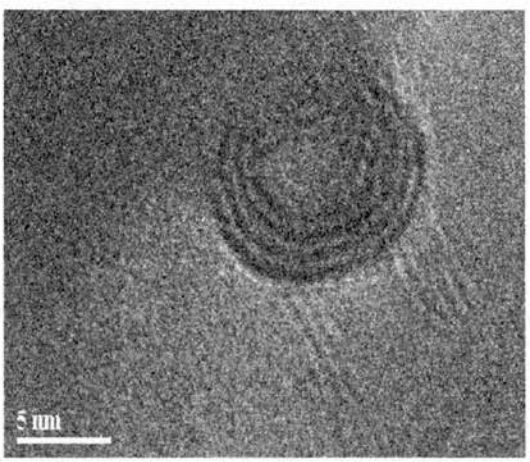

Fig. 3.9 HRTEM image of end-on nanotube, exhibiting a scroll structure.

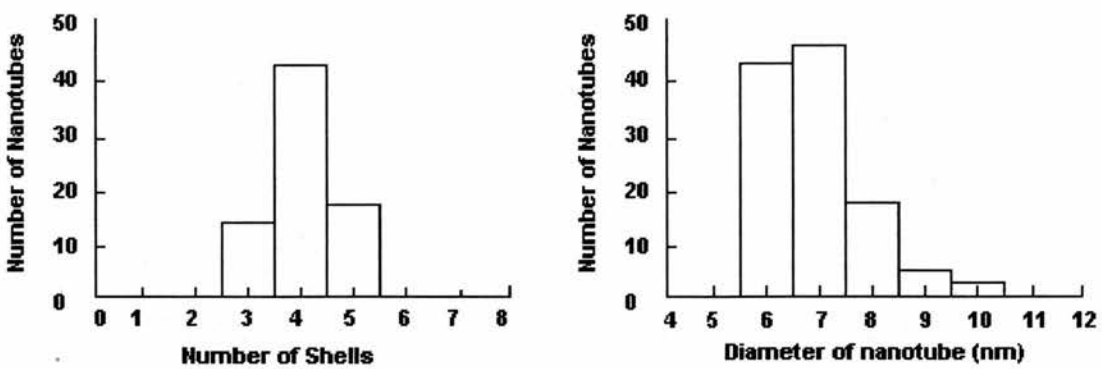

Fig. 3.10 Shell and diameter distribution of trititanate nanotubes.

A crystal sheet of $H_2Ti_3O_7$ is symmetric in hydrogen ion concentration in a bulk crystal. In the reaction medium the concentration of sodium and hydroxide ions from the 10 molar base is very high. The concentration of ions in contact with the top of the surface layer is higher than that of the bulk side of the top layer. Therefore the side in contact with the solution undergoes more frequent collisions with the Na^+ and OH^- ions. The energy gain for an OH^- ion to remove a H^+ ion from the crystal surface to form a H_2O molecule is very high, ~2 eV. It is therefore likely that hydrogen ions will be removed, resulting in an asymmetric sheet.

Through a collaboration with Peking University and the Beijing Laboratory of Electron Microscopy in Beijing[116], ab initio calculations have been performed on $H_2Ti_3O_7$ structures and it has been shown that removing surface hydrogen ions will result in the contraction of the relevant Ti-O bond on the top surface.

These calculations are based on the density function theory (DFT) and performed using the CASTEP computer code implemented in Cerius 2 software and ultrasoft pseudopotentials. The cut-off of the plane wave basis was set at 300 eV. Exchange and correlation effects were included through the generalised gradient approximation, and the Brillouin zone of the unit cell was sampled via a 3 x 7 x 3 mesh. The validity of the cut-off energy and mesh density was inferred from test calculations on anatase phase TiO2 crystal. For this structure we obtained lattice constants a = 0.380 nm and c = 0.989 nm, in an excellent agreement with experimental values and recent first-principles FLAPW calculations[117].

As the calculation involves nearly 100 atoms it is difficult for the calculations to converge using the CASTEP method for configurations far away from the ground state, therefore FastStructure code in Cerius 2 software was used to optimize the atomic configurations and to calculate the total energy values. FastStructure is an *ab initio*

software package specifically designed to determine the structures of molecules, solids, and surfaces by calculating the energy and forces acting on the nuclei and determining the nuclear locations corresponding to the energy minimum.

The Na^+ in solution, which is weakly bound to the surface, balances the charge. The surface strain induced by the removal of the hydrogen ion will result in the sheet curving. When the average number of hydrogen loss per formula unit (δ) approaches 1, the surface strain becomes larger than the coupling energy between the adjacent layers (0.24eV per formula unit). The outcome of this is that the surface layer may peel off from the surface of the plate. This is shown schematically in Fig. 3.11.

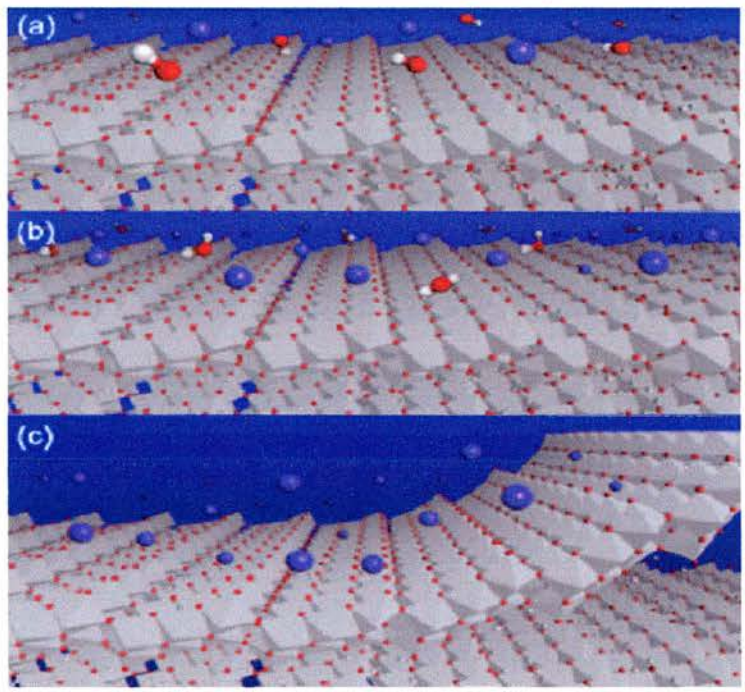

Fig. 3.11 Schematic model of the reaction showing, a) A $H_2Ti_3O_7$ surface in contact with OH^- and Na^+ ions, b) Several H^+ ions on the surface have been removed by OH^- ions, producing H_2O molecules, and c) when the surface hydrogen loss exceeds a critical value the surface strain energy becomes so large that the surface layer may overcome the coupling with the beneath layer and peel off from the plate. White balls are O, red balls H, purple balls Na and grey octahedron TiO_6 units.

A curved fragment of $H_{2-\delta}Ti_3O_7$, where δ is the hydrogen loss per formula unit, is considered in the ab initio calculations, the fragment consisted of eight $H_{2-\delta}Ti_3O_7$ units. The total energy of the fragment was calculated as a function of the radius of curvature R and is plotted in Fig. 3.12. It can be shown to a reasonable approximation that the total energy of a single trititanate layer can be written as:

$$E_{total} = E_{elastic} + E_{tension} + E_0$$
$$= \frac{a}{R^2} + b\delta\left(\frac{\cos\theta}{R} - \frac{\delta}{R_0}\right)^2 + E_0 \qquad 3.1$$

where θ is the chiral angle (the angular deviation from the [001] direction in a single sheet of trititanate and a, b, R_0 are constants and E_0 is the total energy of a flat trititanate layer.

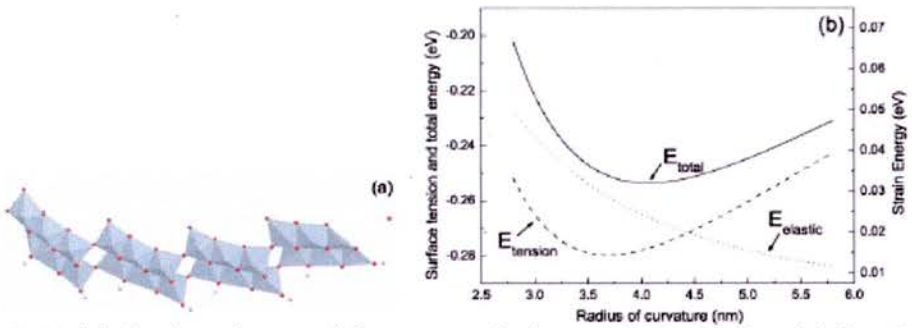

Fig. 3.12 (a) A relaxed curved fragment of a layer of $H_{2-\delta}Ti_3O_7$ with $\delta = 1$ giving R = 4.16 nm. (b) First principle calculations of different forms of energy contributing to the curvature of a trititanate fragment.

The term $E_{elastic}$ is the elastic strain energy of a bent crystalline plate, which, as in the case of a carbon nanotube, has the form $E_{elastic} \propto 1/R^2$. The $E_{elastic}(R)$ curve in Fig. 3.12 was calculated for a fragment with $\delta = 0$. The term $E_{tension}$ is the surface tension resulting from the disparity in H^+ ion content on the two sides of the surface

layer. The $E_{tension}(R)$ curve in Fig. 3.12 was calculated for a fragment with $\delta = 1$. [Using the curves in Fig. 3.12 the constants in equation 3.1 and the total energy as a function of δ can be obtained. The coupling energy is not sensitive to δ so a value of 0.24 eV can be used to find a critical value of δ, which is 0.95 H^+ ions per $H_2Ti_3O_7$ unit.] For a single walled tube, the optimum radius for minimum strain energy was calculated by minimising the total energy with respect to R, as 4.3 nm, which is a good agreement with the observed.

For multiwalled spiral tubes additional factors have to be taken into account.

As a tube scrolls coupling between the layers results in a decrease in energy of the sheet. The radius of curvature of the shells will deviate from the optimum level when the shell number increases. This is, however, small in comparison to the coupling energy. The crystal layer is negatively charged in solution, which will result in a positive Coulomb repulsion energy, $E_{coulomb}$, when the layer scrolls into a tube. This is partially compensated by the sodium ions in solution, but as the shell number increases, so does the Coulomb repulsion.

The shell coupling energy, E_{coupl}, and electrostatic Coulomb energy, $E_{coulomb}$, are plotted as functions of shell number in Fig. 3.13.

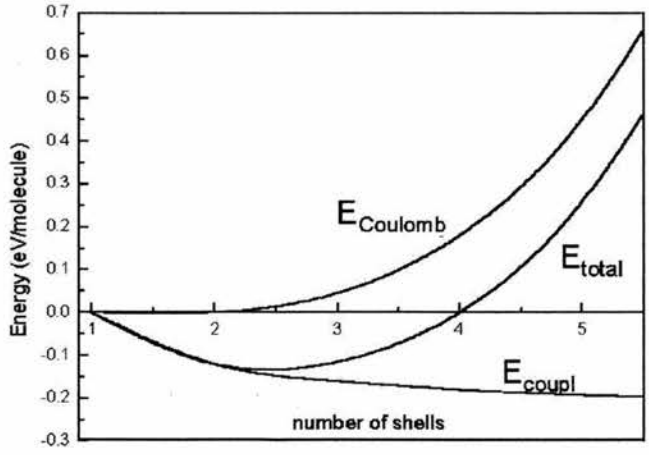

Fig. 3.13 Energy contributions to the total energy as functions of the number of shells in a multiwalled nanotube.

When a nanotube has two or three shells the coupling energy dominates the total energy and drives the scrolling process. As the shell number increases the Coulomb energy increases rapidly and at four shells the total energy becomes positive, halting the rolling process. The offset of these energies results in the termination of scrolling at 4 shells, which also agrees with the observed results. This shows that a narrow distribution of diameter and shell number is expected, which agrees with the experimental evidence. A schematic image of a nanotube formed from scrolled sheets of $H_2Ti_3O_7$ is shown in Fig. 3.14.

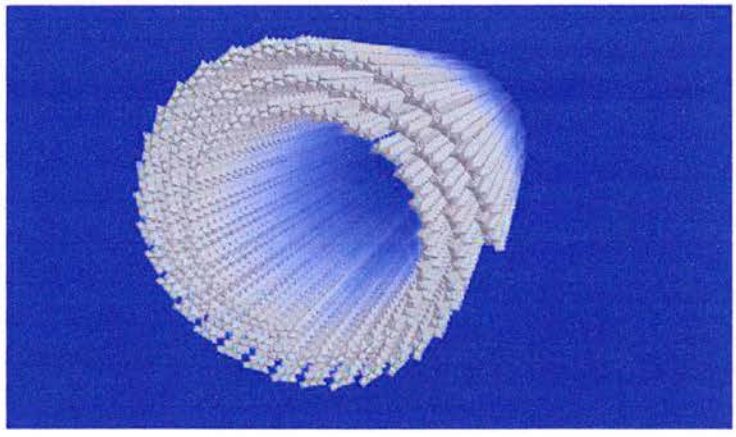

Fig. 3.14 Schematic image of a trititanate nanotube formed by rolling a sheet along the [001] direction.

We have seen many cases of incompletely scrolled tubes. This may be due to structural defects in the sheet, which release surface tension and abort the scrolling process. When more than one sheet of trititanate attempts to scroll together rather than individually, the flexibility of several layers is less than that of one individual layer and the physical constraint of this process may lead to the termination of scrolling, giving areas like Fig. 3.15. Another common occurrence is bent layers- a plate containing 4 or 5 layers which has a kink in it, this is also thought to be a result of more than one layer going through the same process which results in nanotubes for single layers. These

areas may be due to the release of enough strain energy to halt the exfoliation reaction at this time, however as areas like this are not seen in the final product given time nanotubes would have been formed from these bent plates.

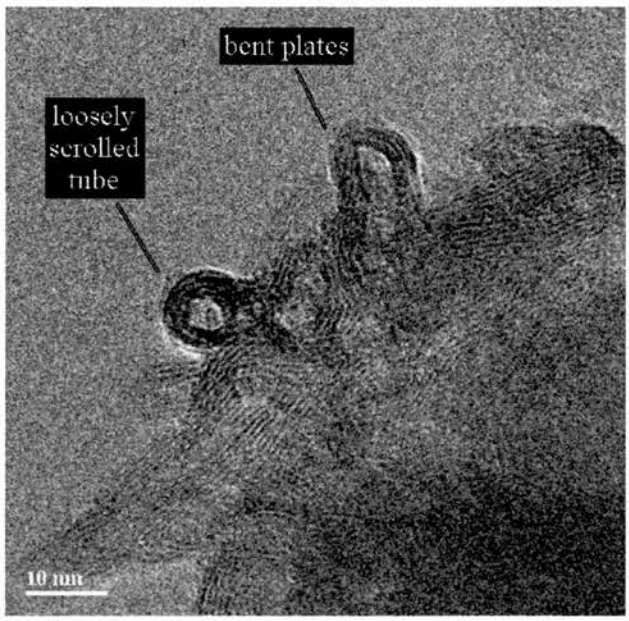

Fig. 3.15 TEM image of areas of incompletely scrolled nanotubes of trititanate.

In the sample heated for 24 hours a loosely scrolled tube was seen (Fig. 3.15). This may have occurred due to some physical constraint during scrolling, as above, or may be a complete tube whose hydrogen bond strengthening of the scroll structure has been disrupted, or may be a less entropically stable phase from which a tightly scrolled tube will result.

Thermogravimetric analysis (TGA) was done on a sample containing trititanate nanotubes, shown in Fig. 3.16. The sample exhibited a weight loss of 8.128 wt % between 64.73 °C and 163.4 °C. Up to 100 °C the loss is 3.01 wt %, and between 100 and 163.4 °C the loss is 5.12 wt %. There is some evidence of an inflection in the weight trace in the range of 60-100 °C. The weight loss up to 100 °C is asigned as water absorbed on the surface of the nanotubes. The weight lost at temperatures in excess of

100 °C is attributed to water contained within the nanotube structure, i.e. between the layers.

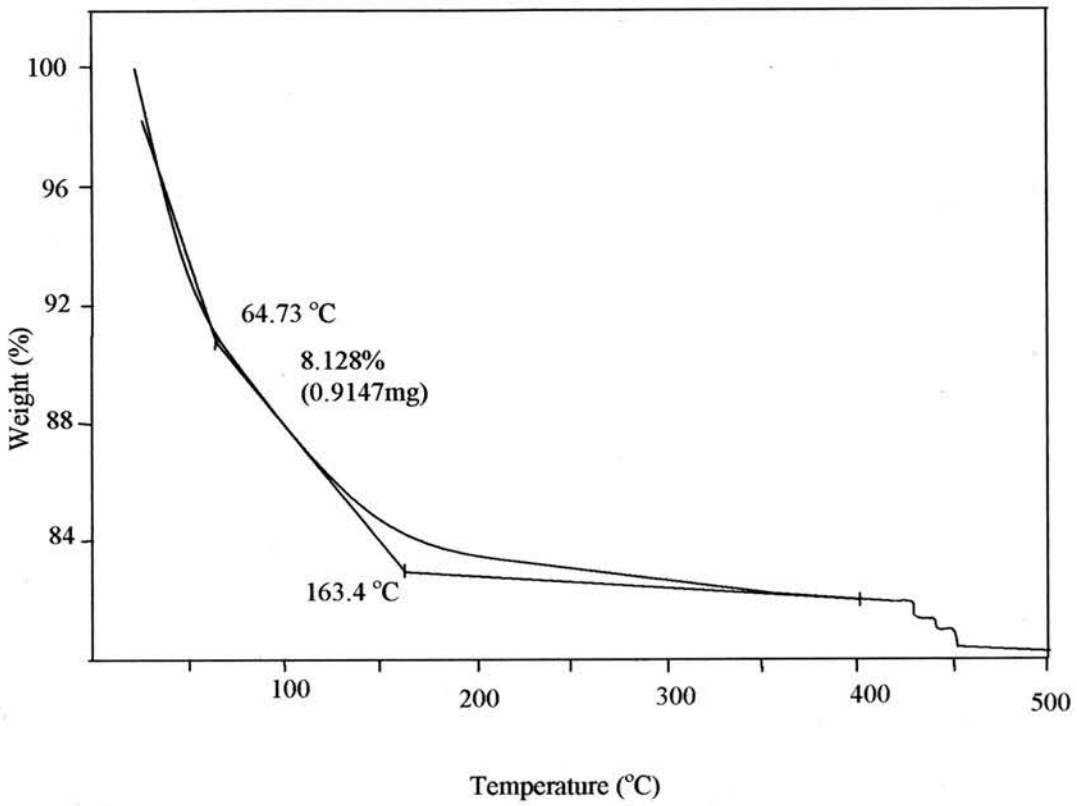

Fig. 3.16 TGA of sample containing trititanate nanotubes.

Trititanate nanotubes contain structural protons and water molecules intercalated between the layers of the tubes. The trapped water molecules may help to stabilise the tubes through hydrogen bonding with the H^+ ions attached to the titanate layers. There is no sodium directly present in the tubes so the hydrogen ions must balance the negative charge of the $Ti_3O_7^{2-}$ plate locally. When the sodium is washed away the tubes do not unscroll due do electrostatic repulsion so the hydrogen must be balancing the charge.

When the reaction time was increased up to and beyond 72 hours a small percentage of nanorods were formed. When the temperature was increased beyond 170

°C, the length of reaction was increased or the concentration of NaOH was increased TiO_2-B nanorods became the dominant feature[118].

The Raman spectrum of a sample of trititanate nanotubes was taken, shown in Fig. 3.17. The sample exhibited peaks at 280.9, 449.5 and 708.6 cm^{-1}. The peak at 450 cm^{-1} can be attributed to a Ti-O-Ti pure framework vibration. The peaks at 281 and 709 cm^{-1} are assigned to Ti-O-H vibrations.

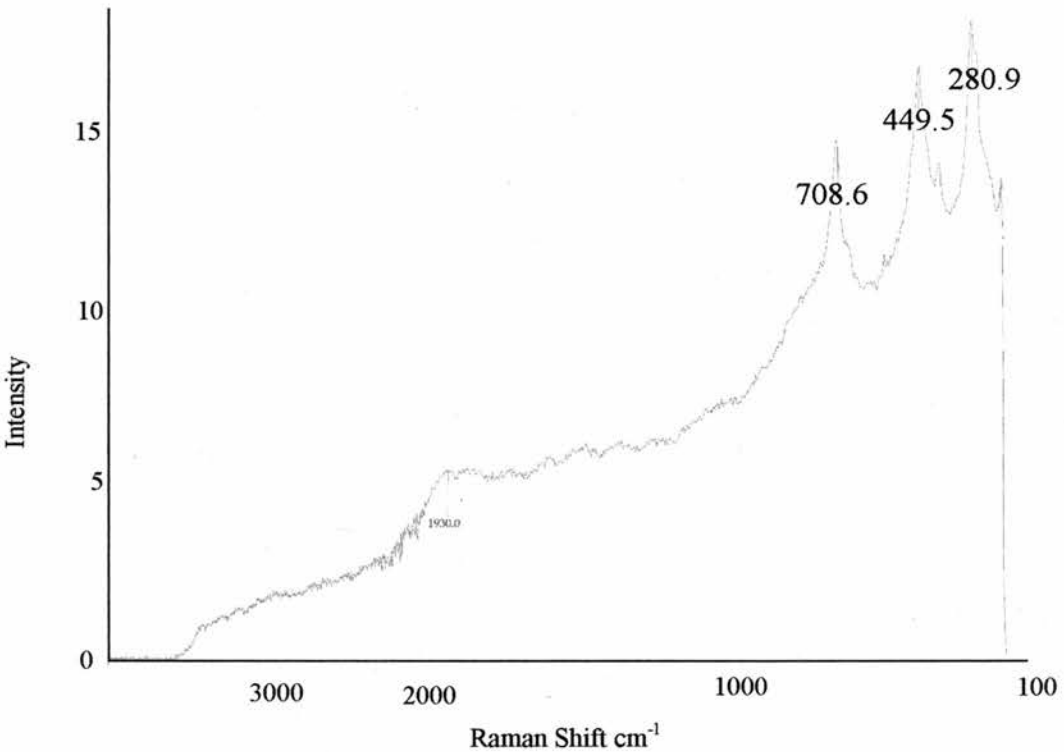

Fig. 3.17 Raman spectrum of a sample containing trititanate nanotubes.

The Raman spectrum of the starting material, rutile TiO_2, was taken, shown in Fig. 3.18. The sample exhibited peaks at 179, 444, 519 and 625 cm^{-1}. The peak at 444cm^{-1} is the E_g mode of rutile. The peak at 625 cm^{-1} is assigned as the A_{1g} mode of rutile. The peak at 519 cm^{-1} is the B_{1g} mode of anatase. The Raman shows that the starting material contains the rutile and a small amount of the anatase phase of TiO_2. The XRD, taken two years previously shows the starting material to be purely rutile, so

a small amount of rutile may have converted to anatase. The amount of anatase present is small, however this does not affect the reaction, as both anatase and rutile are converted to nanotubes[23].

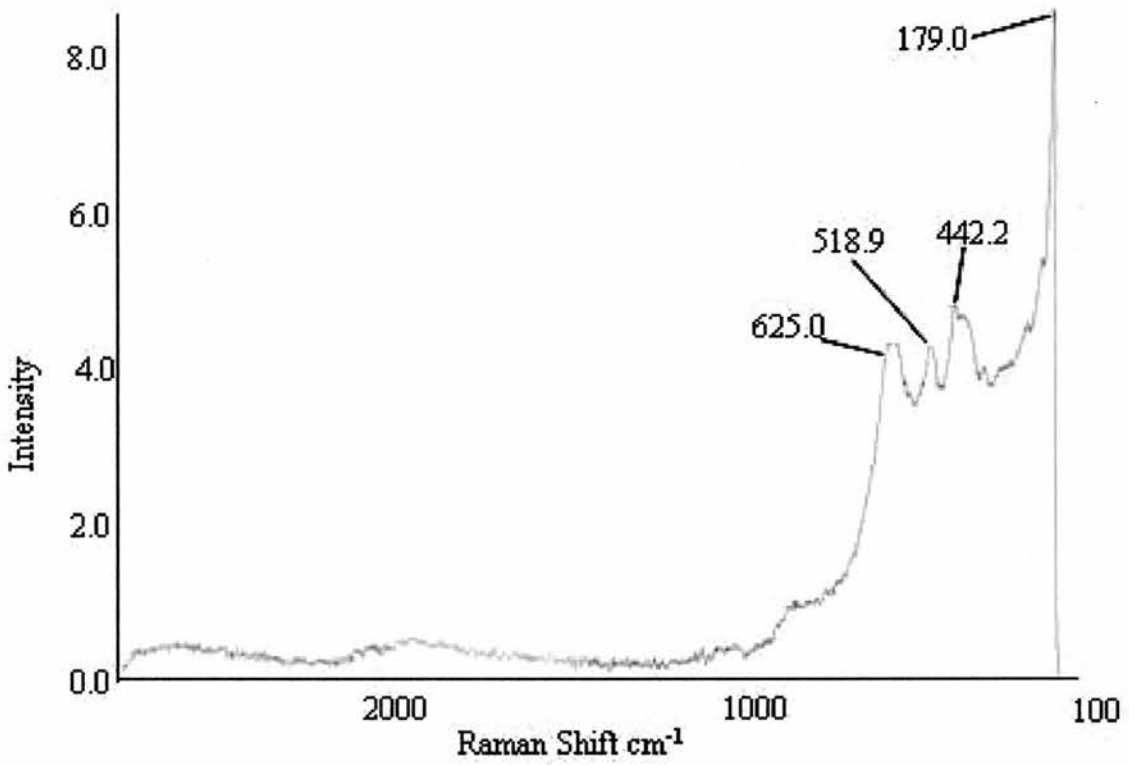

Fig. 3.18 Raman spectrum of TiO_2 starting material.

The peak at 179 cm^{-1} in the starting material has a corresponding peak in the spectrum of the nanotube phase at 186 cm^{-1}. This peak has been blueshifted by 7 cm^{-1}. This may be due to an oxygen deficiency in the nanotubes compared to the TiO_2 starting material. The peak at 444 cm^{-1} is also blueshifed to 450 cm^{-1}. The two peaks also appear in the spectrum of $H_2Ti_3O_7$, which exhibits a stronger Raman spectrum than TiO_2 due to the lower symmetry, at 462 and 190 cm^{-1}. Staring from $H_2Ti_3O_7$ the peaks are redshifted in forming the nanotube phase. This shift may be due to the change in

morphology of the material in going from a layer to tubes, and thus changing the frequency of the mode.

The rutile peaks at 519 and 625 cm^{-1} are not present in the nanotube spectrum. This shows that the nanotubes are not rutile or anatase, but some other titanium-containing phase.

The nanotube phase has two peaks that do not appear in the spectrum of TiO_2, 281 and 708 cm^{-1}. Both peaks are present in $H_2Ti_3O_7$, at 263 and 676 cm^{-1}. This blue shift is explained as an oxygen deficiency. The peaks are assigned as a Ti-O-H vibration in the framework. The shift may also be due to the change in phase, going from a flat layered structure to a curved sheet changing the frequency of the vibration. As the peak is thought to be Ti-O-H, the shift may be due to the creation of hydrogen bonds with water, stabilising the tubes.

Raman spectra of $Na_2Ti_3O_7$ and $H_2Ti_3O_7$, Fig. 3.19 and Fig. 3.20, show more peaks than the nanotube phase due to the more complex crystallinity of the samples. The spectrum of $Na_2Ti_3O_7$ exhibits a strong peak at 885 cm^{-1} and a less intense peak at 848 cm^{-1}. In the spectrum of the nanotubes, rutile and the titanates the peak around 200-300 cm^{-1} is the most intense peak of the spectrum. In $H_2Ti_3O_7$ there is a peak at 832 cm^{-1}, however it is broad and of low intensity compared to the rest of the spectrum. In the case of $Na_2Ti_3O_7$, the peak at 885 cm^{-1} is very intense. The nanotube phase spectrum has no peak signal above 708 cm^{-1}, which is more in-tune with the $H_2Ti_3O_7$ than $Na_2Ti_3O_7$. The Raman scattering of the two titanates are noticeably different from each other, unlike the corresponding XRD maps. It has been shown through EDX that the tubes do not contain sodium and the Raman spectrum agrees with this result.

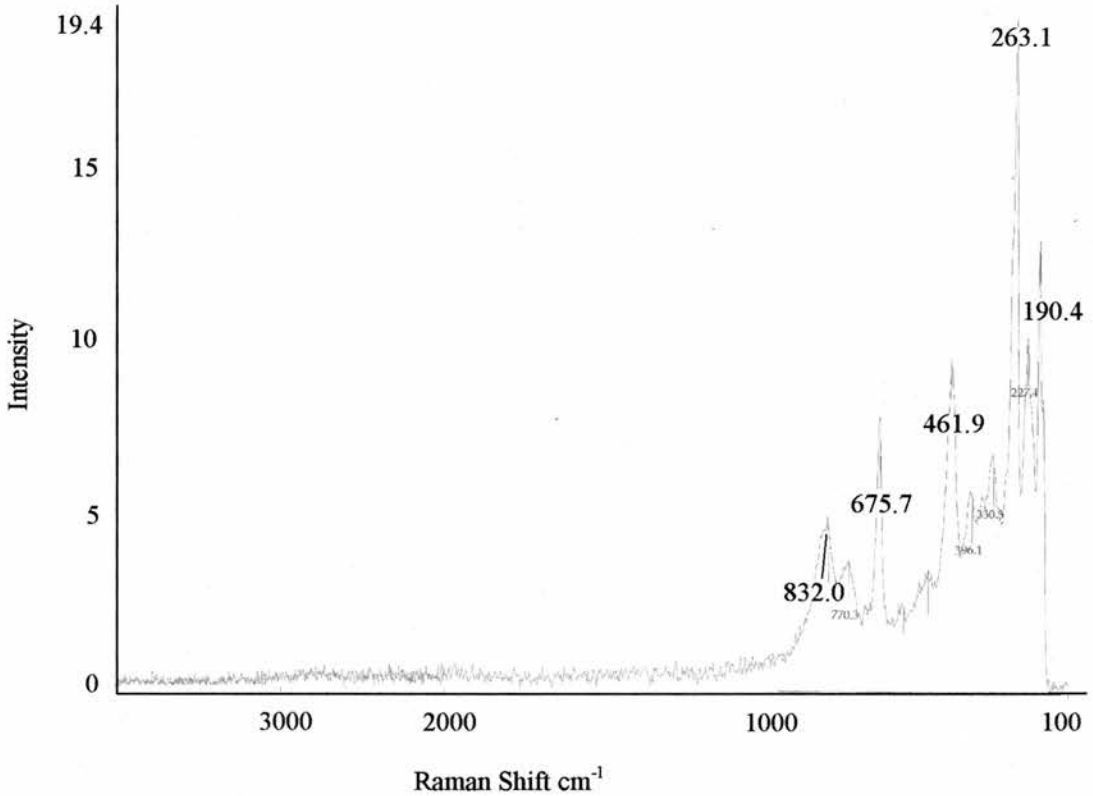

Fig. 3.19 Raman spectrum of bulk $H_2Ti_3O_7$.

The area above 708 cm^{-1}, where a peak is expected at 900 cm^{-1}, and trititanate contains a peak at 832 cm^{-1}, has been broadened by the presence of water. The sample had been dried in an oven to remove surface water. This broadening indicates the presence of structural water, which agrees with TGA.

As the structure of TiO_2 and trititanate are similar, and both contain TiO_6 units, the Raman spectra contain some of the same peaks, however, the spectrum of the nanotubes is clearly more related to $H_2Ti_3O_7$ undergoing a morphology change than TiO_2.

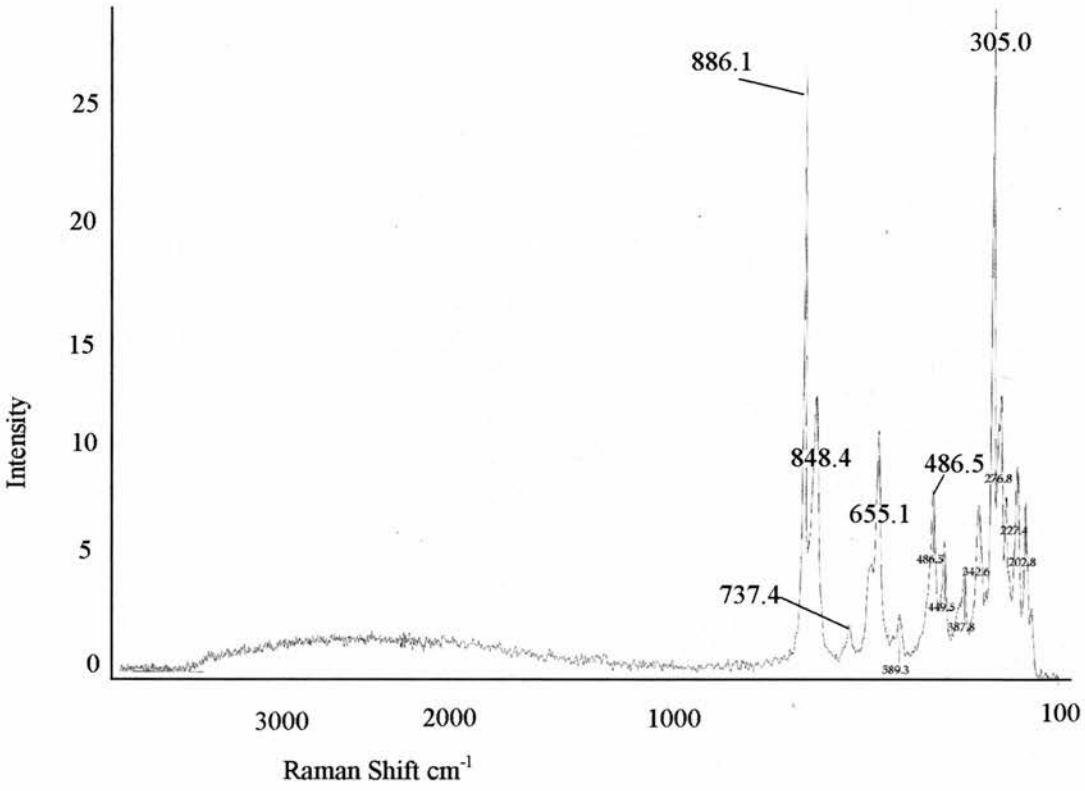

Fig. 3.20 Raman spectrum of $Na_2Ti_3O_7$.

The proposed mechanism of formation of trititanate nanotubes is TiO_2 particles react with 10 molar NaOH to form a disordered amorphous phase. Single sheets of trititanate extrude from this phase, forming thin plates with several layers of $H_2Ti_3O_7$. These layers scroll up to form nanotubes due to an asymmetry of hydrogen concentration on the surface sheet. The tension in the layer is the driving force for the forming of the trititanate nanotubes.

3.2 Nanotubes directly from titanates

From our characterisation results we have shown that the structure of the nanotubes formed from TiO_2 is $H_2Ti_3O_7$, trititanate. We believe it is layers of this material, peeled off from thin plates, which scroll up to form nanotubes. To gain further evidence of our proposed mechanism bulk trititanate was produced and was reacted

with 10 molar sodium hydroxide at 160^{0}C of 72 hours. A precursor in the formation of trititanate, $Na_2Ti_3O_7$, was also reacted with the base. Conversion of $Na_2Ti_3O_7$ to $H_2Ti_3O_7$ is achieved by stirring in HCl at room temperature, and was confirmed by XRD, shown in Fig. 3.21 and Fig. 3.22.

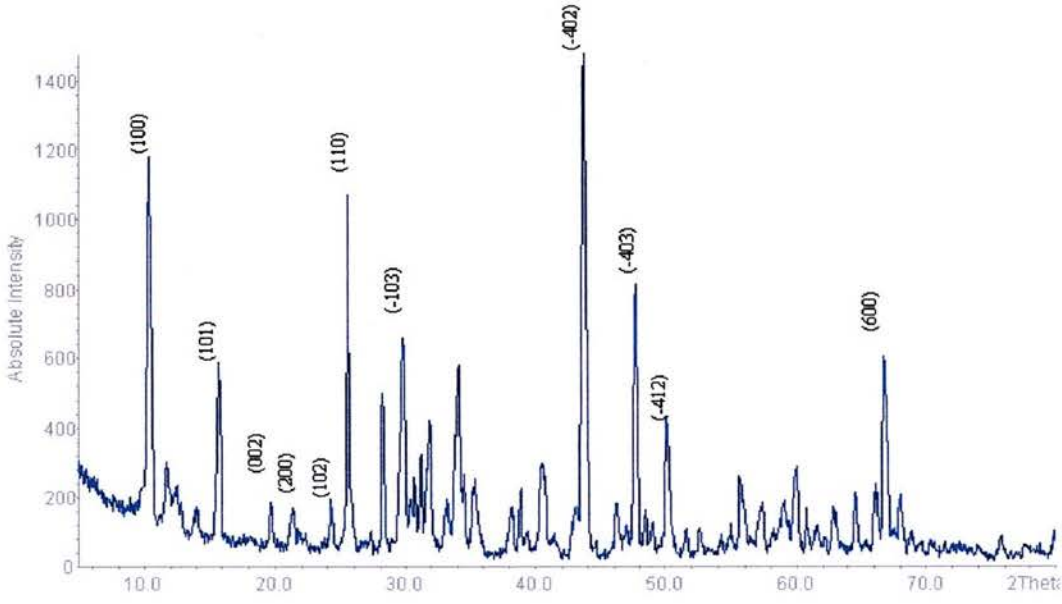

Fig. 3.21 XRD pattern of $Na_2Ti_3O_7$.

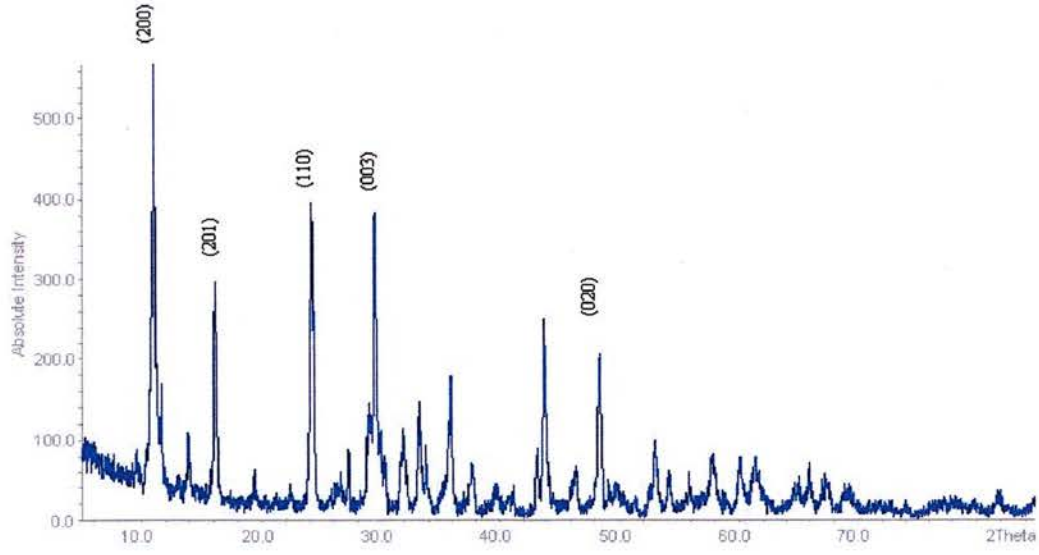

Fig. 3.22 XRD pattern of $H_2Ti_3O_7$.

The sodium between the layers is replaced with H^+ ions in a simple ion exchange reaction. Nanotubes were formed from both titanate reactions. The percentage of nanotubes formed was low (around 5-10 %). The reaction was done at the same temperature and concentration of NaOH as the reactions with TiO_2, however the amount of titanate used in the reaction was lower than the amount of rutile. As a high concentration of NaOH is required for the reaction, and only the last step of the overall reaction was being attempted, the same ratio of Ti:NaOH was not used, and the NaOH was in a large excess. It was not thought that the amount of concentrated NaOH would affect the reaction from our postulated mechanism.

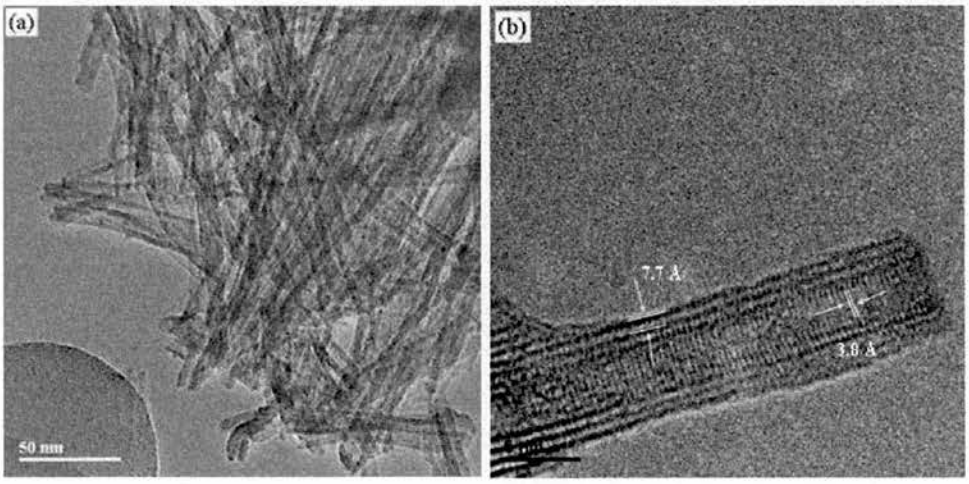

Fig. 3.23 a) TEM image of nanotubes formed from $H_2Ti_3O_7$ and b) HRTEM image of a nanotube.

The nanotubes produced have similar diameters and the same scroll structure as the tubes produced from rutile. Images of the nanotubes produced from $H_2Ti_3O_7$ and $Na_2Ti_3O_7$ are shown in Figs 3.23 and 3.24 respectively. In both the cases of $H_2Ti_3O_7$ and $Na_2Ti_3O_7$ the number of layers in a single tube is ordinarily 4, with an outer diameter between 7 and 10 nm and an inner diameter of 3.5-6 nm. The tubes are hollow, with an intershell spacing of 0.77 nm that corresponds to the (200) spacing in

$H_2Ti_3O_7$. The d-spacing measured along the tube axis is 0.38 nm, which corresponds to the (010) plane. This is evidence that the tubes are composed of $Ti_3O_7^{2-}$ sheets scrolled along the [001] direction.

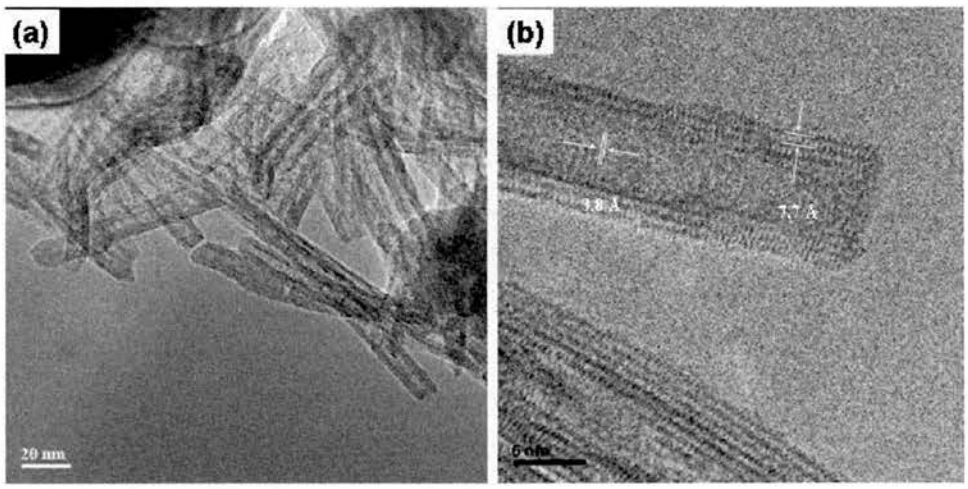

Fig. 3.24 a) TEM image of nanotubes formed from $Na_2Ti_3O_7$ and b) HRTEM image of a nanotube.

The range of lengths of the tubes is large, with most greater than 200 nm, and some up to a few micrometers long. The range in diameter and number of shells is small, as can be seen from Fig. 3.25.

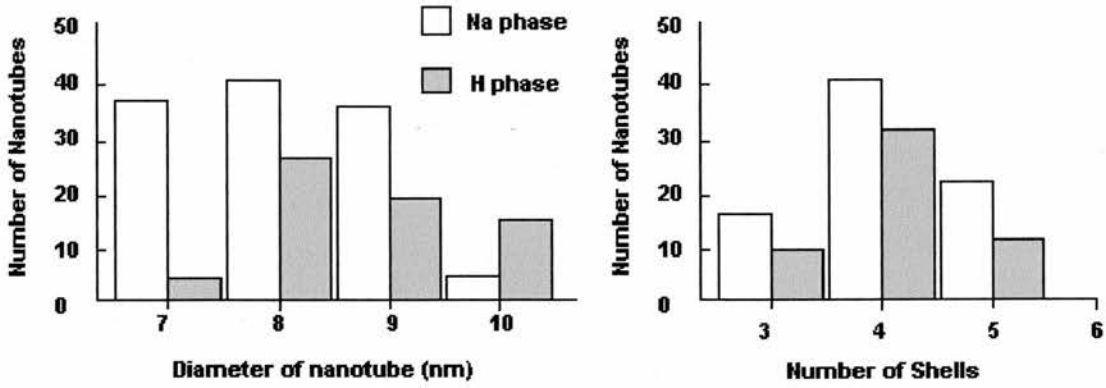

Fig. 3.25 Diameter and shell distributions of nanotubes produced from $H_2Ti_3O_7$ and $Na_2Ti_3O_7$.

The mechanism of formation of nanotubes from $H_2Ti_3O_7$ is thought to be the same as the last step in the formation of tubes from rutile TiO_2. The tubes formed had the same dimensions and composition. The hydrogen ions on the top surface of the crystal plate are removed by OH^- ions. This contracts the Ti-O bond, causing the sheet to curve. When a sufficient number of H^+ ions are removed the sheet overcomes the coupling between the layers and is exfoliated. The tension in the single layered sheet is the driving force in the scrolling to form nanotubes[117].

$H_2Ti_3O_7$ was thought to be an intermediate in the production of nanotubes from rutile TiO_2. Reacting this material directly with 10 M NaOH did produce nanotubes, confirming that the reaction did go through plates of trititanate. In the reaction with rutile thin plates of trititanate are thought to extrude out of an amorphous phase. The $H_2Ti_3O_7$ used as a starting material in the reaction was thick and contained many layers by comparison. This may have resulted in the low yield of tubes, as the reaction conditions are not ideal for reaction of these thicker plates.

The tubes produced directly from $Na_2Ti_3O_7$ and NaOH had the same dimensions and structure as those from rutile, however the exfoliation of monolayers of titanate may be achieved by a slightly different method. Hydrogen ions will be present in the reaction mixture, and these ions could intercalate into the layers of the starting material. In which case the reaction would go by the same mechanism and a low yield would be expected. However $Na_2Ti_3O_7$ is comprised of sheets of edge sharing TiO_6 octahedra with Na^+ ions between the layers and under hydrothermal conditions water molecules intercalating between the layers could replace the sodium ions. As the H_2O molecules are larger than the Na^+ ions the interlayer space is increased resulting in weakened interaction between neighbouring sheets. As a result monolayers of titanate are exfoliated and these sheets scroll into tubes. In the previous reactions the sheets of

trititanate are already curved as they are removed from the bulk and there is a driving force to scroll: to relieve strain. In this case, with much less H^+ present, this driving force is not present, however, work done by Wei et al[97] has shown that the hydrothermal reaction between $Na_2Ti_3O_7$ and H_2O results in the production of nanotubes through the exfoliation of monolayers. These tubes are 30 nm in diameter and are thought to have a TiO_2 composition. The reaction lasts from 5 to 18 days, much longer than the reaction reported here. TiO_2 nanorods are produced if the reaction of rutile and NaOH is allowed to proceed for that length of time. The trititanate nanotubes are not thermally stable enough to still exist after 5 days reaction. However, from this reaction we can see that there is a driving force to produce tubes from exfoliated sheets of $Ti_3O_7^{2-}$. The driving force for the scrolling of the monolayer may be an asymmetry in the $Ti_3O_7^{2-}$ layer, which exists without the presence of hydrogen ions. A titanate sheet in the strongly basic environment may also spontaneously scroll.

The tubes produced from both forms of titanate contain only titanium and oxygen, with no sodium present, as shown in Fig. 3.26. The sodium ions can be washed out of the tubes and are not necessary for tubular structure; they just balance the charge from the negatively charged $Ti_3O_7^{2-}$ plates. The only other positively charged species present is H^+, therefore H^+ ions must have become incorporated into the sheets with the Na^+ ions.

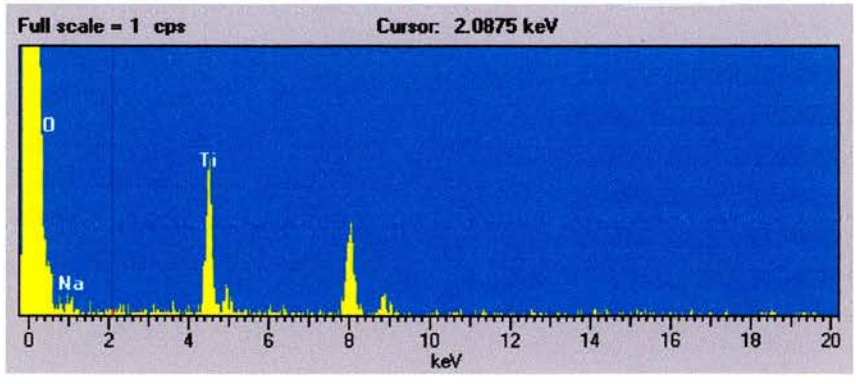

Fig. 3.26 EDX spectrum of nanotubes from $Na_2Ti_3O_7$.

Due to the low percentage conversion to nanotubes the purity of the titanate was examined using XRD. The titanates were made using TiO_2, which when reacted with sodium hydroxide will produce a high yield of nanotubes. From the XRD in Fig. 3.27 it can be seen that there is no TiO_2 present and that all the peaks can be identified as $Na_2Ti_3O_7$. The large peaks expected for TiO_2 are not present, however, both materials exhibit peaks at similar values because their structures are related.

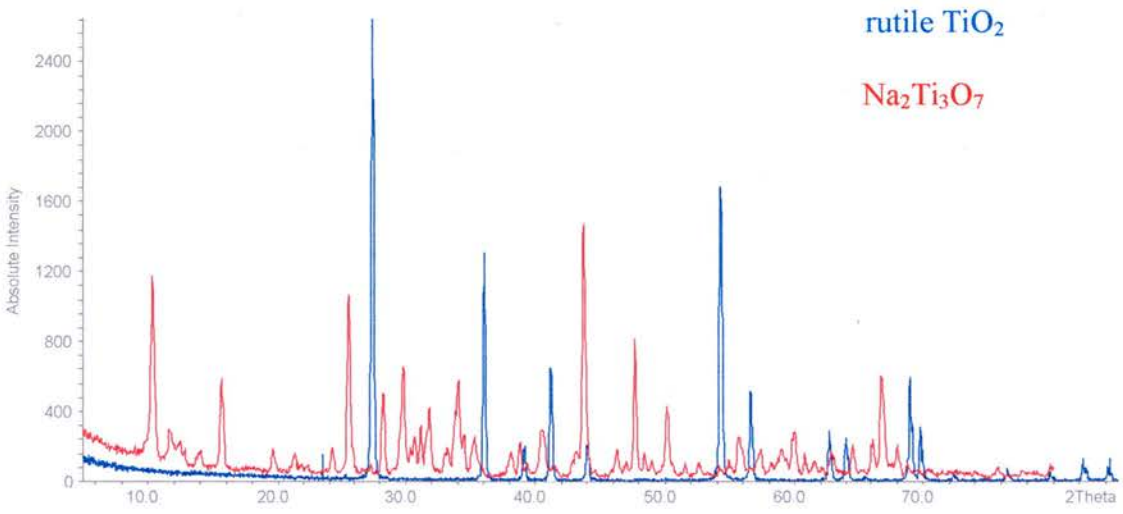

Fig. 3.27 XRD pattern of $Na_2Ti_3O_7$ and rutile TiO_2.

The reaction time was increased from 72 hours to one week as it was thought this would promote higher yields, however similar percentages of nanotubes were observed. The particle size was reduced by grinding the sample in a ball mill. This resulted in decomposition of the starting material, with a mainly amorphous product formed. The material in the autoclave after the reaction was a white slurry, rather than the solid produced from the untreated starting material. The reaction product is normally a sticky solid, however when the particle size was reduced the material retained the consistency of the starting mixture. The titanate had decomposed and no nanotubes were produced.

The temperature of the reaction was increased to 190 °C when no grinding had taken place; this also resulted in decomposition of the starting material. Above 250 °C $H_2Ti_3O_7$ is unstable[119] and along with the harsh basic reaction conditions, the starting material has decomposed, resulting in amorphous material. The sodium form appeared stable at higher temperatures, however it also decomposed at 160 °C after grinding.

The low yield of nanotubes may have been as a result of the low thermal stability of the starting material at these harsh reaction conditions. The temperature of the reaction was lowered to 100^0C. If nanotubes were formed early in the reaction, 72 hours may result in the formation and subsequent degradation of tubes, so the reaction time was also reduced.

The yield of nanotubes produced at 100 °C for 72 h reaction time was 15 – 20 %, higher than the reaction at 160 °C. However after 6 h reaction time at 100 °C the yield was similar, so no more reaction occurred after the first 6 hours.

The tubes aggregate together, much like in the rutile reaction. It would appear from this observation that once one layer has been exfoliated all the layers of that crystal form tubes, and that some crystals do not undergo any exfoliation at all. In the rutile reaction after 72 hours no plates are observed- all material that forms plates is converted into tubes.

An area that appears to be an exfoliated monolayer scrolling from both ends is observed in this sample (Fig. 3.28). From the low magnification image it can be seen that scrolling has occurred on the left and right of the sheet. The sheet is a single layer of trititanate, as can be seen from both the low and high magnification images. Due to the orientation of the scrolling, the ends meet and this terminates the scrolling process. If the reaction had proceeded longer this plate may have formed a tube, as the tube conformation would contain less strain.

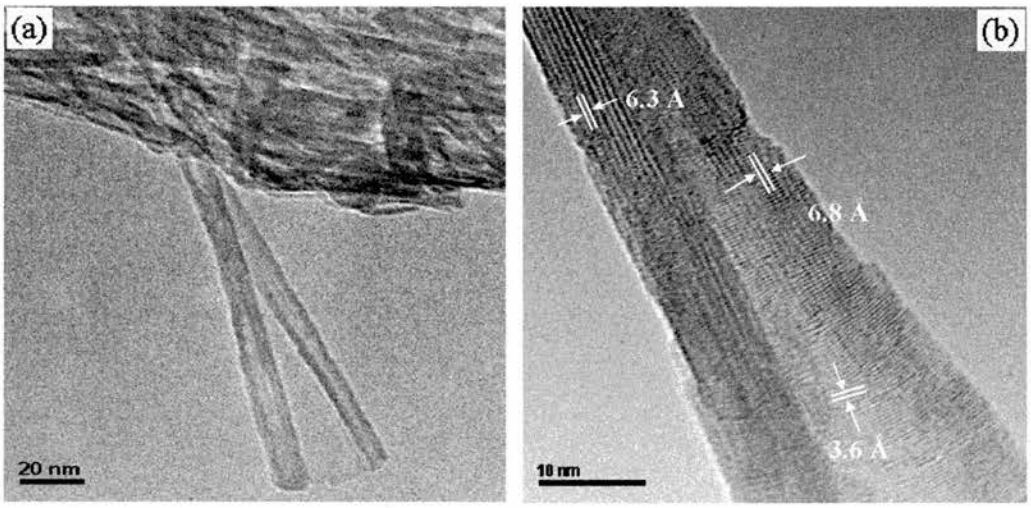

Fig. 3.28 (a) TEM image of a trititanate plate scrolling from both ends. (b) a higher magnification image of same layer.

A d-spacing of 3.6 Å is observed in the middle of the sheet, as shown in Fig. 3.28 (b), this spacing corresponds to the (010) plane in $H_2Ti_3O_7$, which is the same spacing observed in completely scrolled nanotubes (see Fig. 3.6). From this observation we can surmise that the sheet of trititanate is in the correct orientation to produce a nanotube, however the spacings observed in the partially scrolled areas of the sheet, 6.3 and 6.8 Å, are indexed as (201) and (-101) respectively. Therefore, the scrolling process did not start from the normal point and consequently a tube is not formed and scrolling is terminated.

The low yield of nanotubes implies that large sheets of $[Ti_3O_7]^{2-}$ are required to form nanotubes, and that the formation of trititanate sheets from the bulk amorphous phase is an important step in the reaction.

We have therefore been unable to alter the reaction conditions to produce a higher yield of nanotubes.

Conclusion

In order to elucidate the formation mechanism of trititanate nanotubes, the hydrothermal reactions of titanium dioxide and 10 M sodium hydroxide solution were run at 2-hour intervals up to 24 hours. A high yield of nanotubes is formed after 72 hours, however after 24 hours many tubes are present.

In the samples four phases were found. The first phase is the crystalline starting material, rutile titanium oxide. This material is polyhedral and crystalline with a large size range.

The second phase is the amorphous material. This phase contains Ti, O and Na in a disordered state, as shown by EDX. When a sample was washed excessively no sodium was found in the amorphous phase. This shows that the sodium ions are weakly bound to the Ti and O. The harsh reaction conditions have broken the strong Ti-O bonds to create an amorphous phase.

The third phase contains thin plates of trititanate, $H_2Ti_3O_7$. These plates are formed when single sheets of trititanate extrude out of the amorphous phase and couple to form layered plates. It is these layers that scroll to form the nanotubes.

The nanotubes have a scroll structure. The number of shells in a single tube is ordinarily 4, with a diameter of ~8 nm. The tubes are hollow, with an intershell spacing of 0.64 nm.

The concentration of hydroxide ions is higher on the surface of the top layer than it is between the layers. Therefore the side in contact with the solution undergoes much more frequent collisions with the sodium and hydroxide ions. The energy gain for an OH^- ion to remove a H^+ ion from the crystal surface is high, as much as 2 eV, so it is very likely that the H^+ ion will be neutralised to form a water molecule. The sodium ions in solution balance the charge on the surface layer. The hydrogen content

of the crystal sheet is now asymmetric. When hydrogen is bonded to the surface the relevant Ti-O bond is lengthened. When the hydrogen is removed the bond will contract and this will cause the surface to curve. The strain in the layer will eventually overcome the interlayer coupling and the single sheet will peel off and scroll to form nanotubes, with the tension in the layer being the driving force in this formation.

The dimension of the nanotube is controlled by the surface tension and with interlayer coupling energy and Coulomb force.

The structure of the nanotubes is confirmed by XRD, Raman and HRTEM. Due to the closely related structures of TiO_2 and other titanate compounds similarities with the starting material are seen in the spectra, however the results may be more closely indexed as trititanate.

To gain further evidence of this mechanism, we reacted bulk $H_2Ti_3O_7$ and $Na_2Ti_3O_7$ specimens with 10 molar sodium hydroxide. Nanotubes were produced from both reactions. The starting material was shown to contain no TiO_2 through XRD.

Chapter 4: Nanotubes from $K_{4-x}H_xNb_6O_{17}$

4.1 Nanotubes from $K_{4-x}H_xNb_6O_{17}$

In previous work nanotubes from the partially exchanged niobate were first made using tetra(n-butyl)ammonium hydroxide in water[109]. Other work has shown that nanotubes can be formed using straight chain amines as intercalation agents[98]. The aim of this work was to produce nanotubes using different intercalation materials in an attempt to further understand the mechanism of formation of these and trititanate nanotubes.

The reactions were all run using potassium hexaniobate that had been stirred in HCl for 4 days to promote ion exchange. The potassium ions exist in two distinct crystallographic sites in between the $(Nb_6O_{17})_n$ layers of the compound. At room temperature one site undergoes ready exchange, with H^+ ions replacing the larger K^+ ions. This results in a partially ion exchanged layered compound, $K_{4-x}H_xNb_6O_{17}$.

Potassium hexaniobate was produced by a solid state method, reacting niobium oxide and potassium carbonate at 1050 °C in a crucible. The synthesis of $K_4Nb_6O_{17}$ produced a product with no starting material detected; this was shown through XRD, Fig. 4.1. The XRD pattern of the product is indexed based on an orthorhombic unit cell with a = 0.783 nm, b = 3.321 nm and c = 0.646 nm. The ion-exchanged material was also characterised by XRD, Fig. 4.2. The pattern is indexed as a $K_4Nb_6O_{17}$ like unit cell, with the peaks between 22 and 32 down shifted by 0.2, caused by the slightly different structure after ion-exchange. The peak at 10.6°, indexed as (040) is the interlayer spacing for the $K_4Nb_6O_{17}$ material.

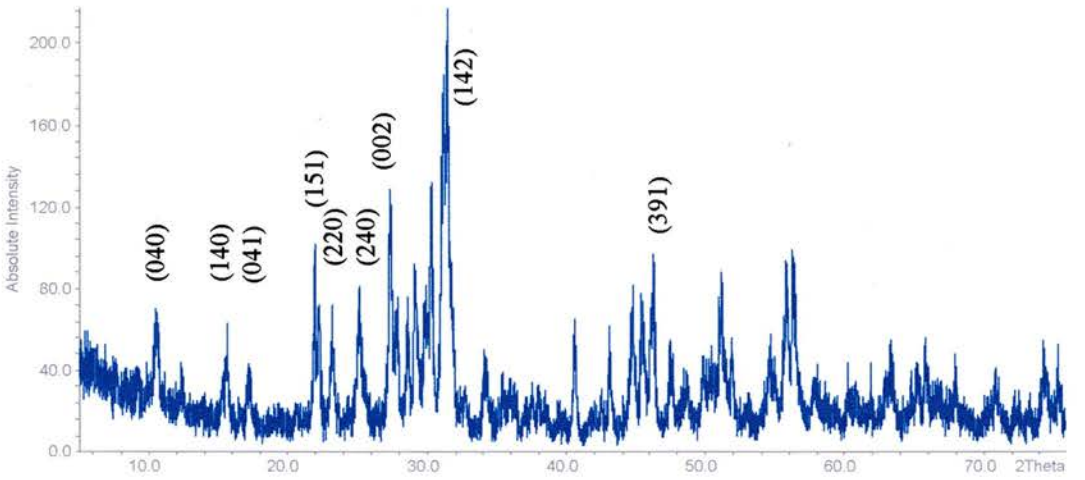

Fig. 4.1 XRD pattern of $K_4Nb_6O_{17}$.

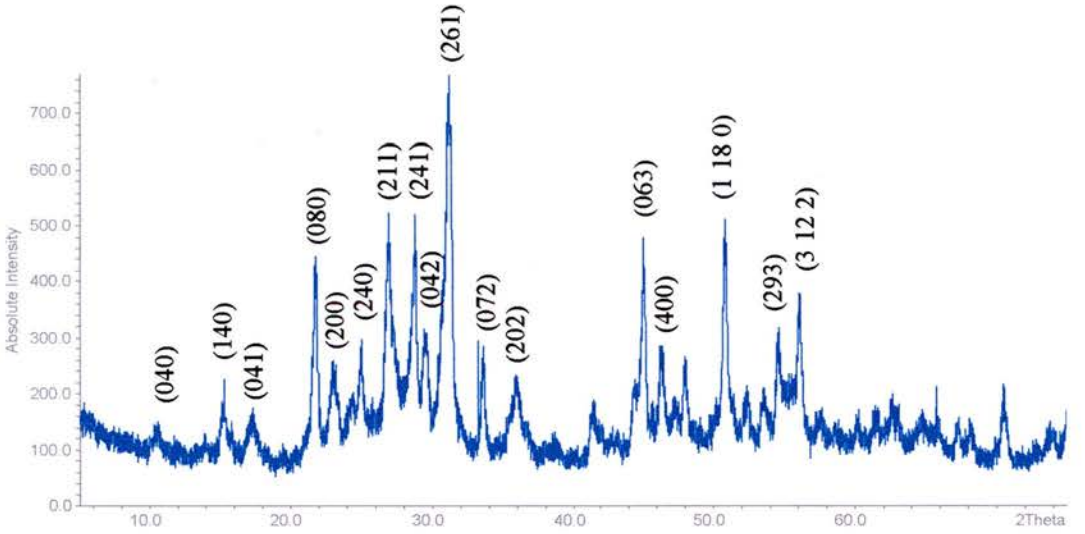

Fig. 4.2 XRD pattern of $K_{4-x}H_xNb_6O_{17}$.

Ion exchanged niobate was stirred with butyl amine in water at room temperature for 3 days. This produced a high yield of nanotubes. The tubes are of a scroll structure, with an intershell spacing of 1.9 nm and an outer diameter of 20 nm, shown in Fig. 4.3. This agrees with the work done by Zhang et al[98].

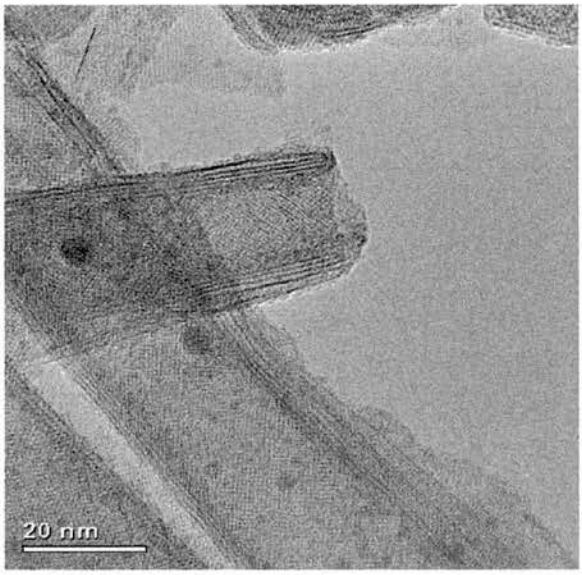

Fig. 4.3 TEM image of nanotube from $K_{4-x}H_xNb_6O_{17}$ using butyl amine as an intercalating agent.

Experiments were done with di and tri substituted amines in an attempt to further tailor the interlayer spacings of the nanotubes.

The reactions were done at room temperature, following the literature method. The yields for all the reactions were high. As the amines used were volatile and yields were good the reaction was not done at higher temperatures or in an autoclave.

4.1.1 Diethyl amine

The ion exchanged niobate was stirred with diethyl amine in water at room temperature for 3 days. This produced scroll nanotubes, as shown in Fig. 4.4, with intershell spacings of 0.94 nm and 1.7 nm and an average outer diameter of 29 nm, shown in Fig. 4.5. The number of shells in each tube was predominantly 5/6. The nanotubes had good stability under the beam and no decomposition was evident. The

diameter and shell number distributions are shown in Fig. 4.6. The yield of tubes was ~ 70 %.

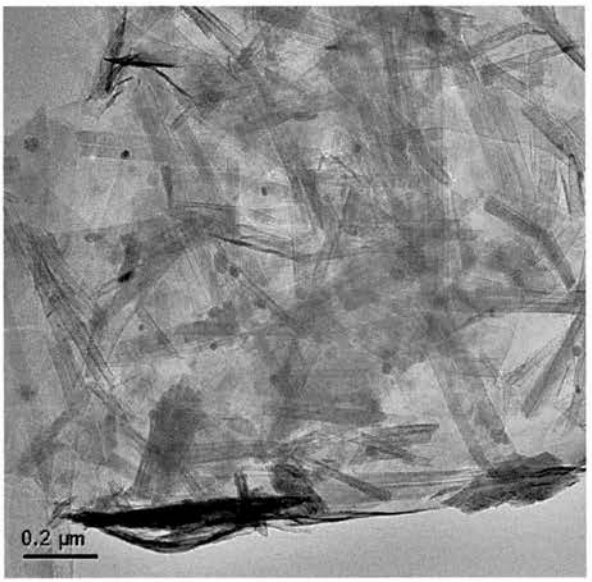

Fig. 4.4 TEM image of $K_{4-x}H_xNb_6O_{17}$ nanotubes formed using diethyl amine as an intercalating agent.

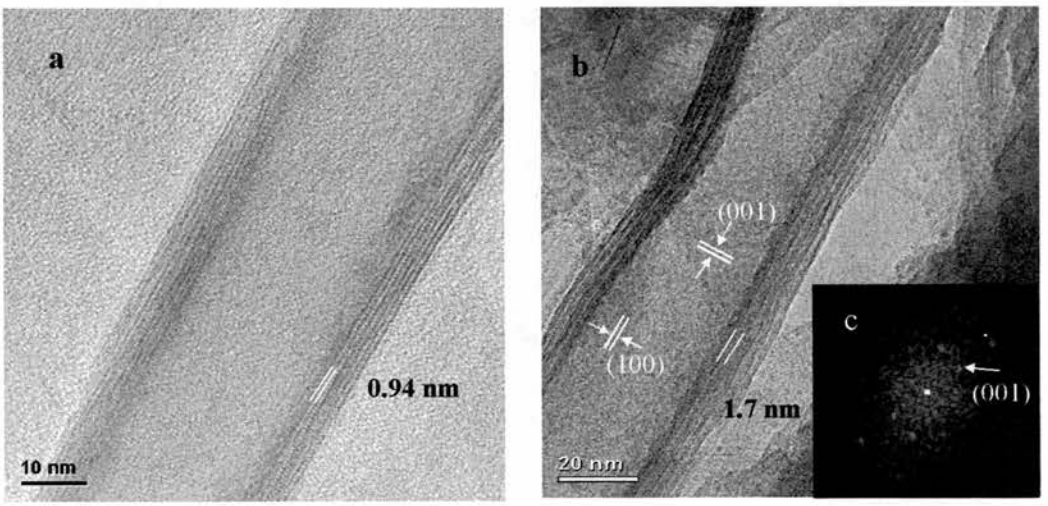

Fig. 4.5 HRTEM images of nanotubes from $K_{4-x}H_xNb_6O_{17}$ using diethyl amine as an intercalating agent: (a) with an intershell spacing of 0.94 nm and outer diameter of 34 nm, (b) with an intershell spacing of 1.7 nm and outer diameter of 40 nm. The inset (c) is the corresponding SAED pattern of the nanotube.

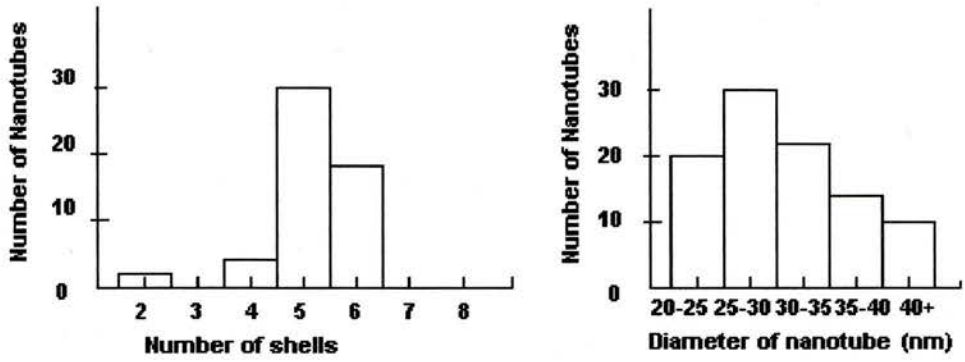

Fig. 4.6 Diameter and shell distributions for niobate nanotubes prepared with diethyl amine.

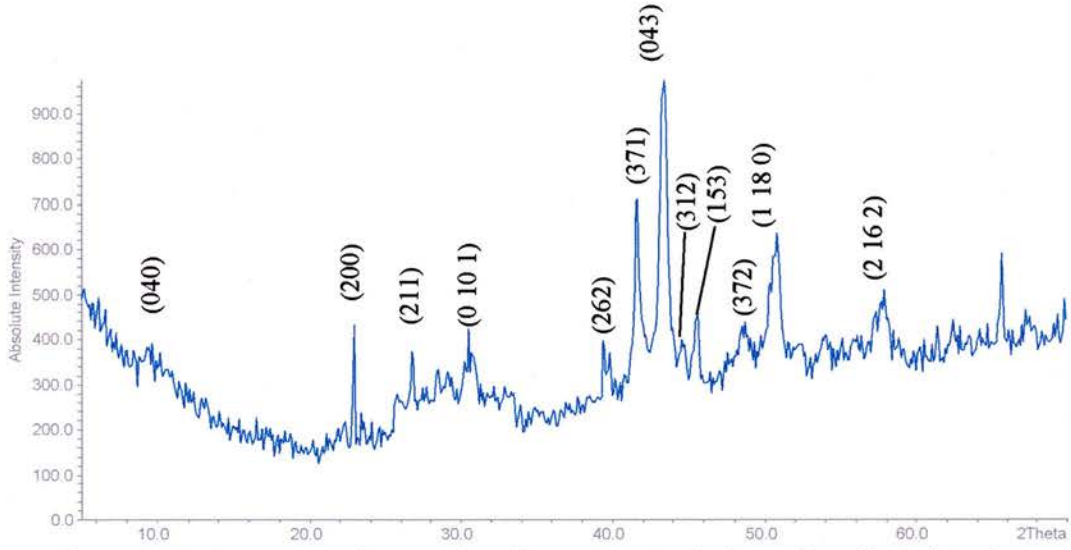

Fig. 4.7 XRD pattern of nanotubes from $K_{4-x}H_xNb_6O_{17}$ using diethyl amine as an intercalating agent.

The XRD pattern of the $K_{4-x}H_xNb_6O_{17}$ nanotubes, shown in Fig. 4.7, is indexed based on orthorhombic $K_4Nb_6O_{17}$ with a = 0.783 nm, b = 3.321 nm and c = 0.646 nm and shows good agreement. The (040) peak in the XRD, which corresponds to the interlayer spacing in the nanotube, appears at 0.83 nm in the parent material. This peak

appears at 9.3°, which corresponds to a d-spacing of 0.95 nm, which is in agreement with the observed interlayer spacing in TEM studies. Another peak is expected at 2.6°, corresponding to the observed d-spacing of 1.7 nm, however the equipment used can only scan to 3°. The SAED pattern of the nanotube is shown in Fig. 4.5c. A spacing of 0.649 nm corresponds to the (001) plane, which runs perpendicular to the long axis of the nanotube. The (100) plane lies parallel to the tube axis, with an observed spacing of 0.799 nm. This confirms that the nanotubes are scrolled monolayers, which have scrolled across the (001) direction.

4.1.2 Triethyl amine

The ion exchanged niobate was stirred with triethyl amine in water at room temperature for 3 days. This produced spiral nanotubes, as shown in Fig. 4.8, with intershell spacings of 0.74 and 2.18 nm and an average outer diameter of 34 nm. The number of shells in each tube was predominantly 4. The diameter and shell number distributions are shown in Fig. 4.9. The yield of tubes was around 70 %.

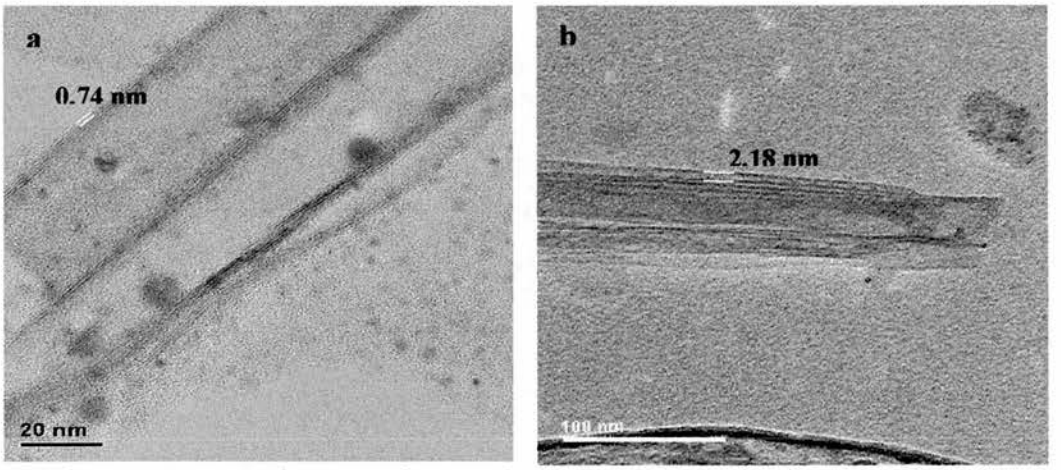

Fig. 4.8 HRTEM images of nanotubes from $K_{4-x}H_xNb_6O_{17}$ using triethyl amine as an intercalating agent: a) with an intershellspacing of 0.74 nm and b) with an intershell spacing of 2.18 nm.

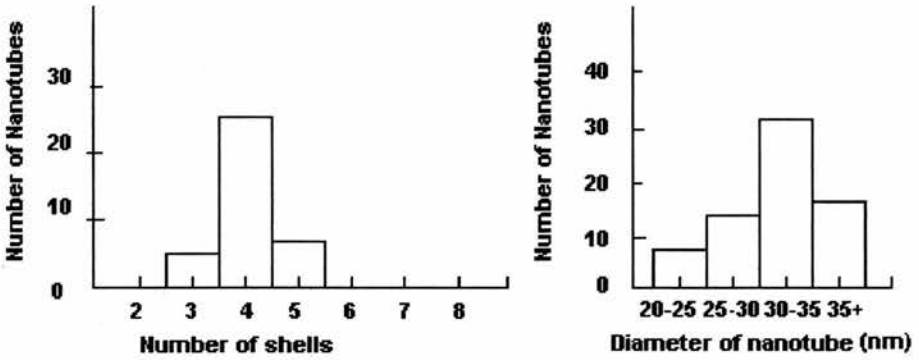

Fig. 4.9 Diameter and shell distributions for niobate nanotubes prepared with triethyl amine.

4.1.3 Mechanism

When amine is intercalated between the layers of the $K_{4-x}H_xNb_6O_{17}$ crystal, the amine molecules are much larger than the ions they are replacing and the interlayer spacing itself, the sheets are exfoliated. The monolayer does not have an inversion symmetry, it is asymmetric, and an intrinsic tension exists which curves the sheet to release the strain and produce tubes. The lack of inversion symmetry is due to both sides of the sheet being different, one side is more sterically crowded than the other[98]. When the crystalline sheet is composed of more than one layer it may be symmetric and a tube would not be produced. If the sheet contains many layers and is still asymetric, the flexibility of the sheet will be less than that of one individual layer and the physical constraint may lead to the termination of the scrolling process.

The amine molecules became protonated by the H^+ ions in the niobate structure and are bound to both sides of the negatively charged niobate layer, $(-Nb_6O_{17}-)_n$, due to strong electrostatic interactions.

The sizes of the particles of ion exchanged niobate are not uniform throughout the sample and this results in a large distribution in size of nanotubes.

The dimensions of the interlayer space are dependent on the type of amine used in the reaction. The interlayer spacing of the (040) plane is 0.83 nm in the parent compound. When no molecules are intercalated between the layers of the tube, or the molecules are smaller than 0.83 nm, the interlayer spacing of the tube will be 0.83 nm, as is the case when tertiary butyl ammonium hydroxide is used as a template. These tubes do not contain any amine molecules[109].

When diethyl amine was used as the organic template two distinct intersell spacings were observed, 0.93 nm and 1.7 nm, as shown in Fig. 4.5. The proposed amine configuration in the interlayer space for a nanotube with a spacing of 0.93 nm is shown in Fig. 4.10. The dimensions of a diethyl amine molecule are such that if the nitrogen of the amine were attached to the tube wall, then a distance of 0.61 nm would protrude[98]. If the molecules were arranged in a staggered formation, as can be seen in Fig. 4.10, then a spacing of 0.93 nm could be achieved.

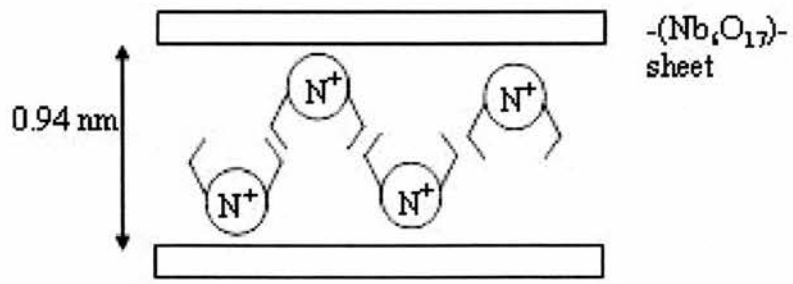

Fig. 4.10 Amine configuration for interlayer spacing of 0.93 nm.

The proposed amine configuration in the interlayer space for a nanotube with a spacing of 1.7 nm is shown in Fig. 4.11. The width of a diethyl amine molecule is 0.85 nm. Two molecules lying as depicted in Fig. 4.11, would give a span of 1.7 nm.

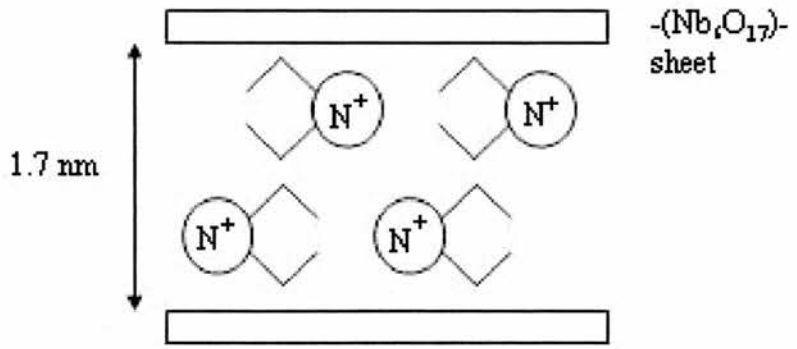

Fig. 4.11 Amine configuration for interlayer spacing of 1.7 nm.

Two configurations were also observed in the tubes produced with triethyl amine. One set of tubes had an interlayer spacing of 0.73 nm, less than the free standing layer separation. This contraction may be due to a decrease in energy provided by packed amine molecules between the layers. The proposed configuration of amine molecules is shown in Fig. 4.12. The positive charge on the nitrogen atom will be attracted to both negatively charged sheets, which could also result in a contraction.

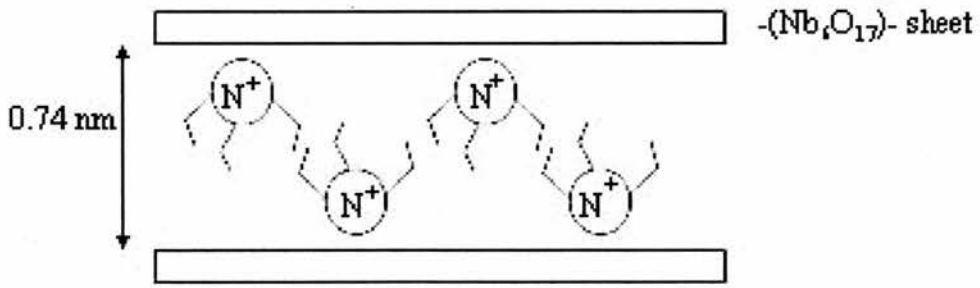

Fig. 4.12 Amine configuration for interlayer spacing of 0.74 nm.

The other interlayer spacing exhibited when using triethyl amine was 2.18 nm. The proposed configuration of amine molecules is shown in Fig. 4.13. The three molecules would give a separation of around 2.1 nm, but with repulsion this may increase it to

~2.18 nm. The triethyl amine is more sterically hindered than diethyl amine, which may explain why no arrangement like that seen in Fig. 4.11 is seen.

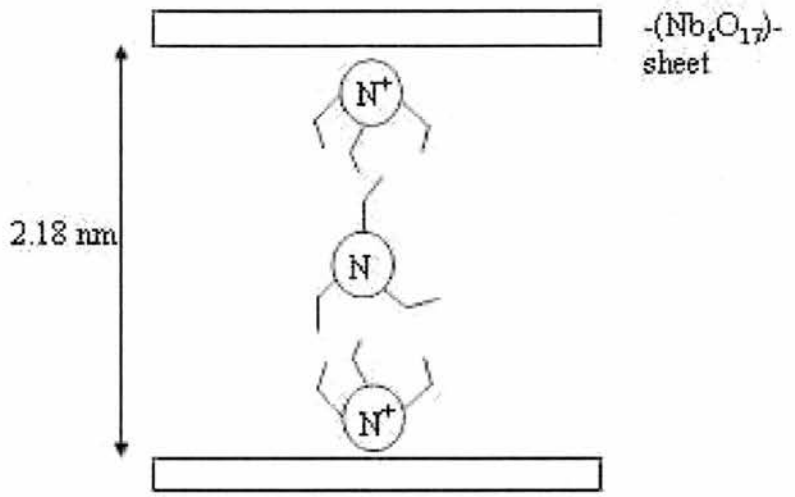

Fig. 4.13 Amine configuration for interlayer spacing of 2.18 nm.

Diethyl amine is more basic than triethyl amine, so more stable in the protonated form, however the difference is small[120], with diethyl amine having a pK_a of 10.98 and triethyl amine 10.76. The effect on the reaction would be minimal.

TGA DATA

Thermal gravimetric analysis done on a sample of nanotubes formed using diethyl amine shows that there is a small weight loss between 80 and 140 °C, which is attributed to residual water in the sample. Between 151.75 °C and 214.15 °C a weight loss of 14.29 % is seen. This weight loss is due to loss of diethyl amine in the nanotubes. The boiling point of diethyl amine is 56 °C. The large difference in boiling point and temperature at which the molecules leave the sample show that the amine is bound to the layers of $K_{4-x}H_xNb_6O_{17}$ and requires more energy to release it. This shows that the amine is incorporated between the shells of the nanotubes.

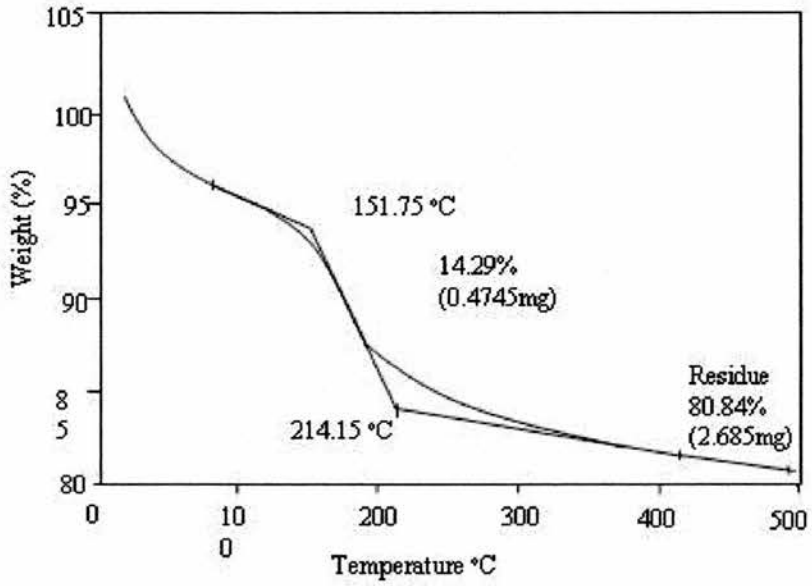

Fig. 4.14 TGA of $K_{4-x}H_xNb_6O_{17}$ nanotubes formed using diethylamine as an intercalating agent.

After a portion of the nanotube sample was subjected to thermal gravimetric analysis it was examined under TEM and it was found that the nanotubular character of the sample was lost. It appears that the nanotubes have unscrolled and the monolayers of $K_{4-x}H_xNb_6O_{17}$ have been attracted together, and aggregated, as can be seen in Fig. 4.15.

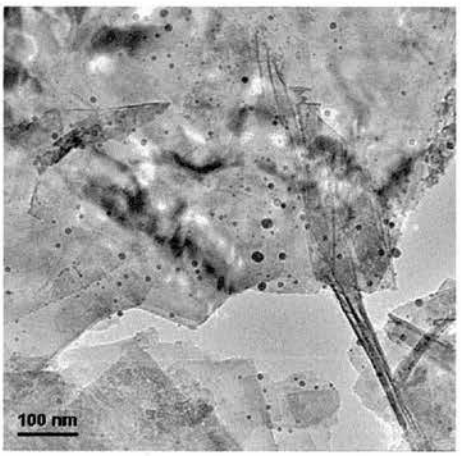

Fig. 4.15 TEM image of a sample of $K_{4-x}Nb_6O_{17}$ nanotubes with diethyl amine as the intercalating agent after undergoing thermal gravimetric analysis.

After 1 year a sample of nanotubes formed with diethyl amine was looked at again. The sample contained many unaltered nanotubes, however, some of the tubes had started to decompose. A high yield of tubes is produced in the reaction with diethyl amine, however on examining the sample after a year many of the tubes had completely unscrolled and layered plates of material was observed.

The tube in Fig. 4.16 (a) is tight on one side, however on the other side it has loosened much like a hanging scroll of paper. A diagrammatic representation is shown in Fig. 4.16 (b). It would appear that amine molecules have leached out of one side of the tube, which has released the attraction/hold link between the layers and caused the relaxation of the structure. Whilst the amine intercalation into $K_{4-x}H_xNb_6O_{17}$ results in the production of nanotubes, the amine does not stabilise the tubes to any great extent. The tubes are not thermally stable and may also unroll on their own volition after time.

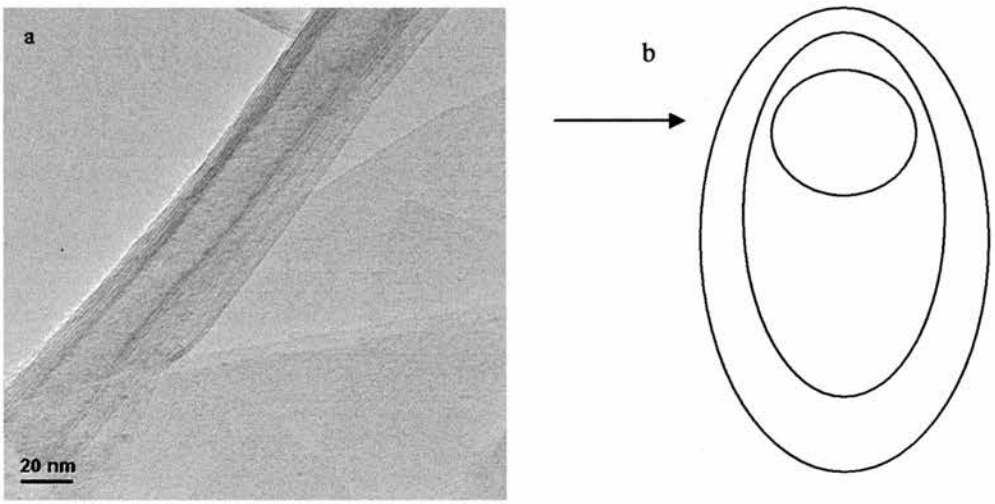

Fig. 4.16 (a) TEM image of partially unscrolled tube and (b) diagrammatic form of image.

Some tubes also collapsed inwards. Fig. 4.17 shows a tube with an outer diameter of 22 nm, however it is comprised of 8 layers and the inner diameter is only

4.8 nm. A tube with this number of layers would have an expected diameter of around 50 nm. The interlayer spacing is 0.75 nm, which corresponds with earlier results, so it is the inner hollow that has collapsed and not the layer spacing. The strain from the large tube- 8 layers is not a very common conformation- must have become too much and the tube collapsed inwards to give the observed tube with the small inner hollow. This shows that the nanotubes are not as stable as the titanate tubes and that the balance between layer coupling and Coulombic repulsion does not have as marked an effect on tube dimensions as it does with trititanate nanotubes.

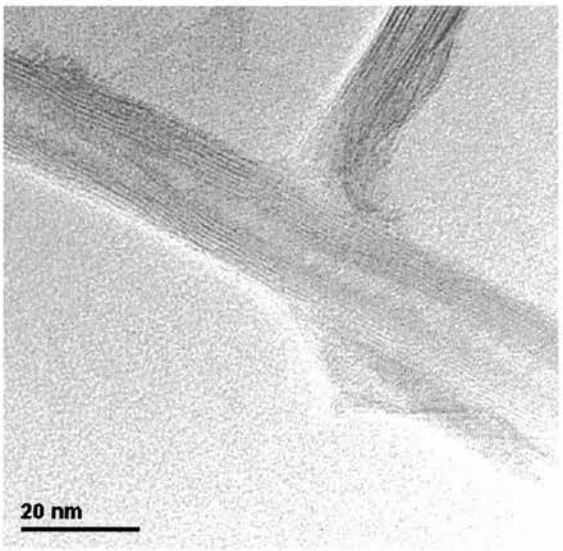

Fig. 4.17 TEM image of a collapsed $K_{4-x}H_xNb_6O_{17}$ nanotube formed with diethylamine as an intercalating agent.

4.2 Other intercalation compounds

Other compounds were looked at as intercalation materials. Quaternary ions, monoamines and di and tri substituted amines all produced nanotubes when intercalated between the ion exchanged niobate. The nitrogen of the amine is thought to be attracted to the niobate sheet, with the tail of the molecule hanging between the layers. The size

of the molecular tail should determine the interlayer spacing of the nanotubes. The interlayer spacing of the tubes shows that when straight chain amines are used as the structure-directing agent, a bilayer of amine molecules separates the layers of the tubes. The size and shape of the amine will also affect the packing of the molecules in between the layers of niobate. For these reasons small straight chain alcohols and thiols were used as intercalation materials to investigate whether the properties of nitrogen were necessary for the production of nanotubes

The reaction was repeated using pentanethiol as opposed to an amine. No nanotubes were produced. There were some areas where thin plates had been exfoliated, shown in Fig. 4.18.

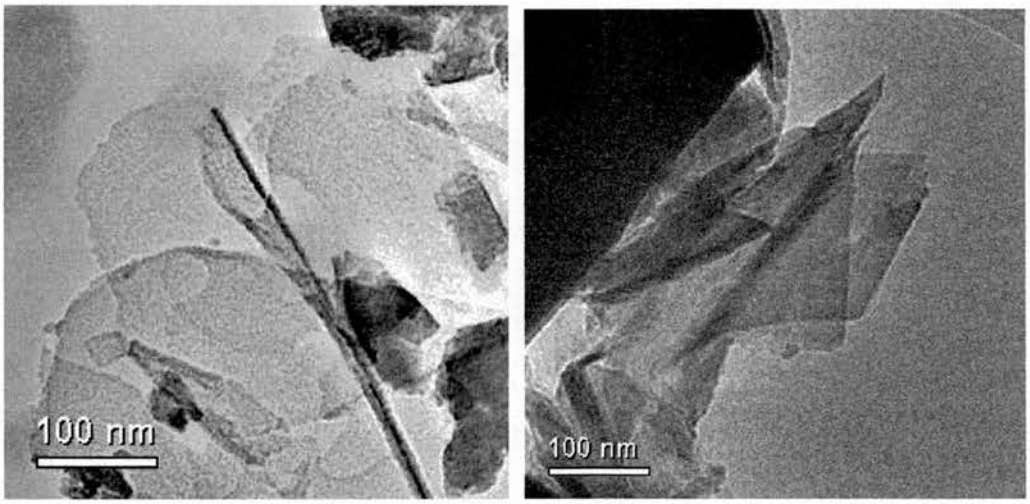

Fig. 4.18 TEM images of exfoliated layers of $K_{4-x}H_xNb_6O_{17}$ produced from the reaction with pentanethiol.

When the reaction was repeated using ethanol thin plates were formed. Some areas of rods were also formed, shown in Fig. 4.19. When a longer alcohol, butanol, was reacted with the ion-exchanged niobate only thin plates were formed.

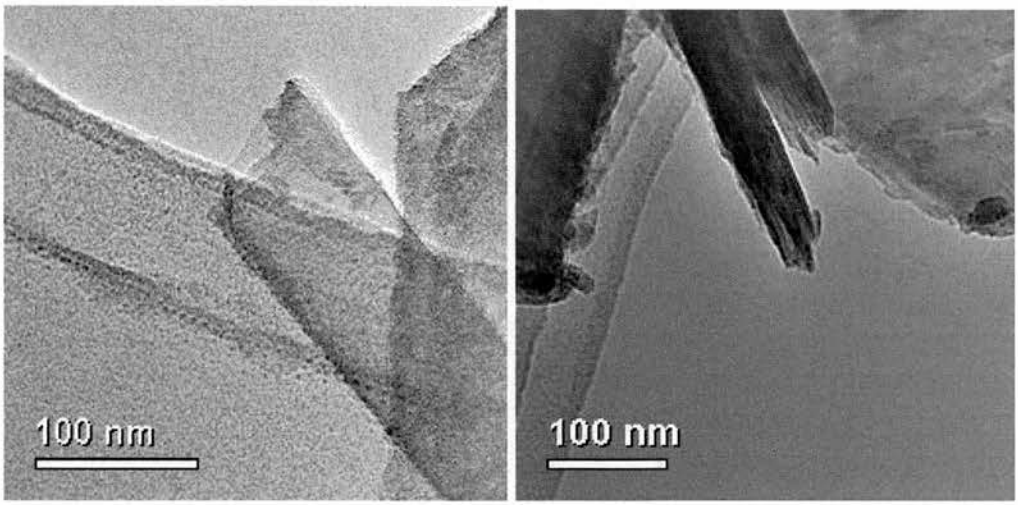

Fig. 4.19 TEM images of nanorods produced from the reaction of ethanol and $K_{4-x}H_xNb_6O_{17}$.

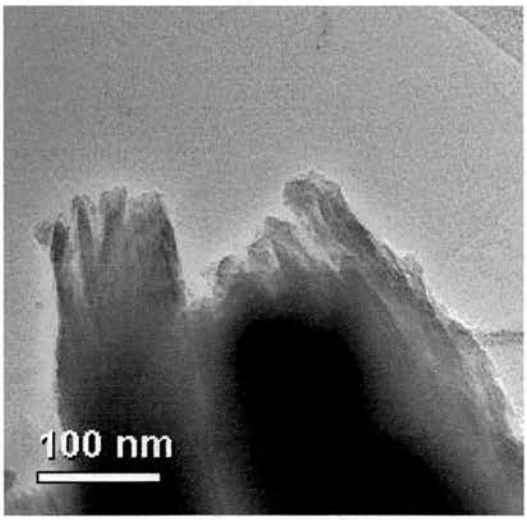

Fig. 4.20 TEM image of a $K_{4-x}H_xNb_6O_{17}$ particle breaking into nanorods after a treatment with ethanol.

The image in Fig. 4.20 shows a particle of $K_{4-x}H_xNb_6O_{17}$ breaking up into nanorods. This is evidence of the postulated mechanism of formation of the nanorods, that the alcohol molecules are intercalated into the structure and cleave off portions of the bulk material.

The SAED pattern of a nanorod is shown in Fig. 4.21, and is indexed based on an orthorhombic $K_4Nb_6O_{17}$ unit cell with parameters of a = 0.783 nm, b = 3.321 nm and c = 0.646 nm. The lattice spacing of 0.558 nm corresponds to the (060) plane, which runs parallel with the long axis of the nanorod. A spacing of 1.14 nm was also observed, which corresponds to the (030) plane of $K_4Nb_6O_{17}$. These observations show that the (010) planes run parallel to the nanorod long axis, which agrees with the postulated mechanism.

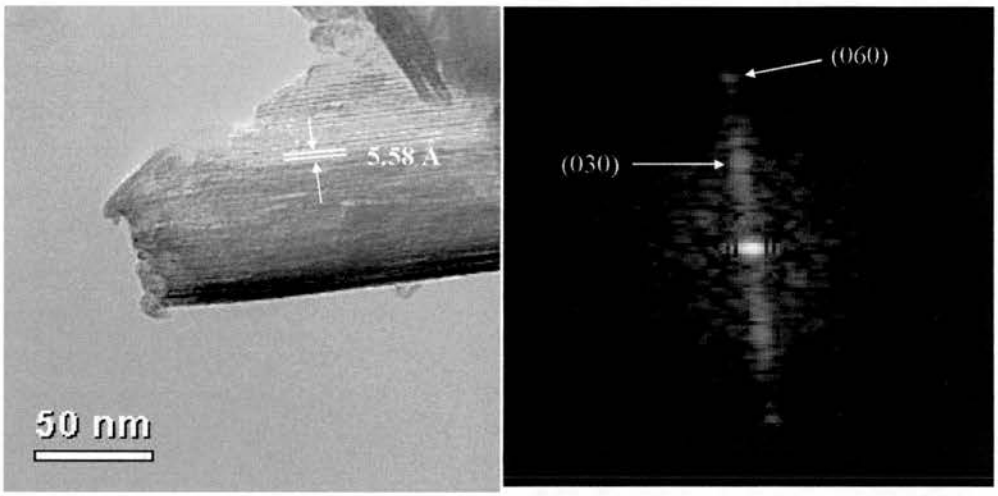

Fig. 4.21 TEM image of a nanorod produced from the reaction of ethanol and $K_{4-x}H_xNb_6O_{17}$ and the corresponding SAED pattern.

The reaction was also done using tetra-n-butlyphosphonium bromide. It was thought that a positively charged phosphorus would perform the same role as nitrogen in the reaction- coupling to the niobate layer and causing scrolling to form nanotubes. The reaction was unsuccessful in producing nanotubes, however rods with diameters of 100 to 200 nm were formed, shown in Fig. 4.22. The same mechanism of formation as for the reaction with ethanol is postulated.

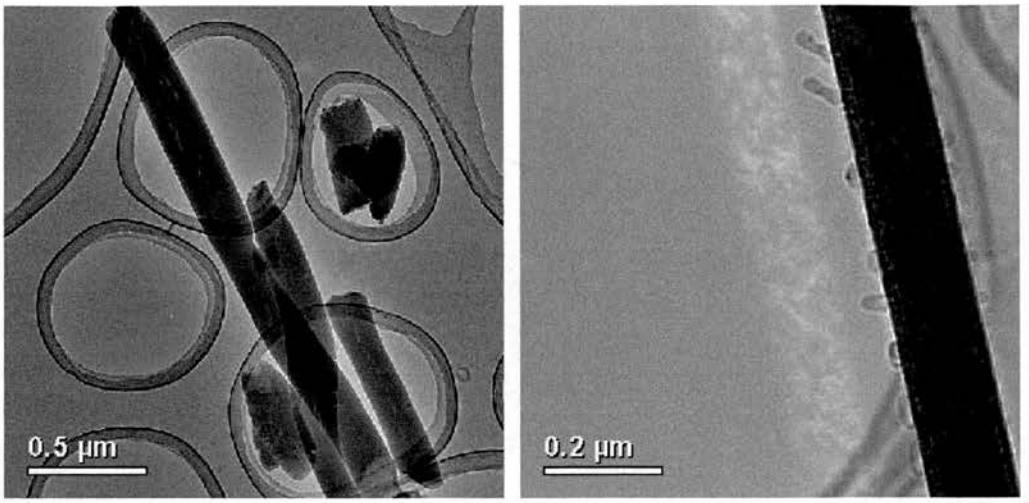

Fig. 4.22 TEM images of rods formed from the reaction of tetra-n-butlyphosphonium bromide and $K_{4-x}H_xNb_6O_{17}$.

When molecules of a similar size to butylamine were intercalacted between the layers of $K_{4-x}H_xNb_6O_{17}$ exfoliation of layers of the niobate occurred. Intercalation of ions or molecules into the lamellar space of potassium hexaniobate is common. The reaction results in the ions or molecules residing between the crystal layers. Under hydrothermal conditions this process can result in exfoliation of large bilayers. When the potassium ions are partially exchanged with H^+ the exfoliation reaction occurs at room temperature. When amines are used as the intercalation material into $K_{4-x}H_xNb_6O_{17}$ the product contains nanotubes. When alcohols and thiols are used no nanotubes are produced however exfoliation does occur. This means the properties of amines are imperative for the production of $K_{4-x}H_xNb_6O_{17}$ nanotubes. Amines are stonger bases than alcohols, so the protonation step will occur more readily. Therefore not enough butanol was protonated, so only exfoliation could occur as the attraction to the niobate sheet wasn't high enough. An alcohol will have a stronger hydrogen bonding network than an amine, which will make it less available for the tube forming

step, however exfoliation can occur. The alcohols and thiols have two lone pairs, whereas the amines only have one.

4.3 Conclusions

In previous work straight chain amines were used as intercalation and exfoliation materials in the reaction with partially ion exchanged potassium hexaniobate, $K_{4-x}H_xNb_6O_{17}$, to create nanotubes. The number of layers in the wall is typically 4, but can be between 3 and 8. When tetrabutylammonium hydroxide is used the intershell spacing is 0.83 nm. The intershell spacing can be altered using di and tri substituted amines. When diethyl amine is used the spacing is increased to 0.93 and 1.4 nm. The diameter of the tubes is 20 nm with a wide range of lengths.

Changing the intercalation agent to triethyl amine increased the spacing to 2.18 nm, and the outer diameter to 40 nm. Nanotubes with a decreased spacing of 0.74 nm are also observed. These results are summarised in Fig. 4.23.

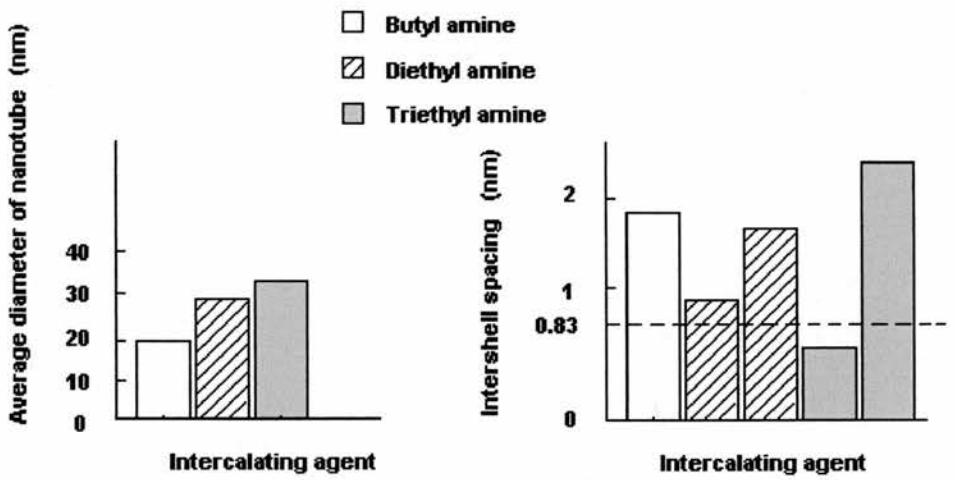

Fig. 4.23 Average diameter and intershell spacing of niobate nanotubes

When an amine is intercalated between the layers of the crystal the top layer can cleave off, and as the monolayer is asymmetric an intrinsic tension exists which curves the sheet to release the strain and produce tubes. When the $K_4Nb_6O_{17}$ has not been acid treated the intercalation results in the exfoliation of large bilayers and multilayers.

It can be seen that altering the intercalating amine results in nanotubes of different intershell spacing and consequently, different diameters. This may be useful in catalytic reactions, where the tube size may affect activity and in the many instances where amines are used as templates in nanoscale synthesis. These results show that, rather than just cleave the layer off and scroll independently, the amine molecules are incorporated into the nanotube and affect its size.

When the amine is replaced with other similar molecules no nanotubes are produced, however in the case of ethanol and tetra-n-butlyphosphonium bromide, nanorods are produced.

Chapter 5: Nanorods and nanotubes of other metal and non metal oxides

5.1 Introduction

As nanotubes were formed from the hydrothermal reaction of titanium dioxide and 10 molar sodium hydroxide the same reaction was carried out using other metal oxides. Tantalum and tungsten oxide were chosen due to their position in the periodic table, tantalum is positioned directly below niobium and tungsten is diagonally below niobium and titanium. Both elements had previously produced dichalcogenide nanotubes. Both metal oxides have an octahedral configuration similar to titanium dioxide.

Aluminium and silicon oxides were also subjected to the hydrothermal reaction with strong base. Nanotubes of Al and Si oxide have previously been prepared by various techniques, including deposition and templating[13,48,92].

The aim of these experiments was to create nanotubes of various metal and non-metal oxides using the synthesis method previously described for titanium dioxide.

5.1.1 Tungsten oxide nanorods

Nanotubes of tungsten chalcogenides have already been described in chapter 1. The layered structure of these compounds makes it feasible for the production of tubular structures. Tungsten oxide is a light green powder that is used as a glaze in ceramics. The W atoms are octahedrally coordinated by oxygen atoms and these octahedra share all six corners with other octahedra to form a three-dimensional structure, as can be seen in Fig. 5.1. In WO_3 adjacent bonds in linear - O - W - O - W - O - arrangements have alternating lengths (about 1.8 and 2 Å,). The oxide can adopt

several distorted forms of the ReO_3 structure and can crystallise with different symmetries when prepared at various temperatures, including triclinic, monoclinic and orthorhombic. The bond energy[121] for W-O is 672 $\pm$ 42 $kJmol^{-1}$ (the average bond enthalpy in methane is 416 $kJmol^{-1}$).

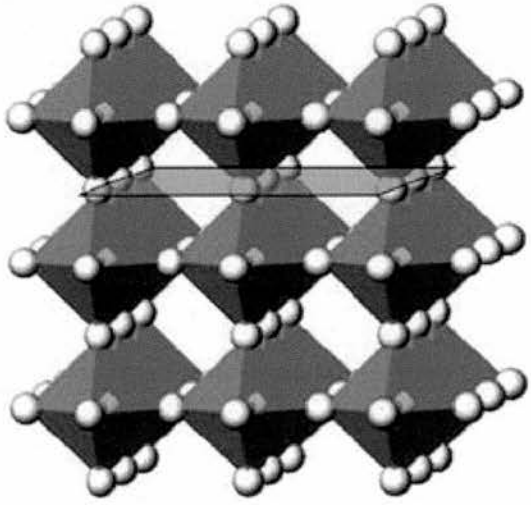

Fig. 5.1 Ideal crystal structure of WO_3 showing vertex-sharing WO_6 octahedra, reproduced from ref [122].

Tungsten oxide nanorods have been produced using several different methods. These reactions have all utilised harsh conditions, high reaction temperatures and, in many cases, elaborate routes. The rods are all single crystals and composed of WO_3 or sub oxides of WO_3, such as $W_{18}O_{49}$ or WO_2, denoted WO_x, and have exhibited several different crystalline phases, including hexagonal and monoclinic. A number of groups have converted these nanorods into WS_2 nanotubes by reducing them in the presence of H_2S.

Metal oxide nanorods have been produced using carbon nanotubes as templates[123]. As well as WO_3, rods of V_2O_5, Sb_2O_5, MoO_3, MoO_2, RuO_2 and IrO_2 were formed from this reaction. The carbon nanotubes were prepared by the arc vaporization

of graphite rods in a helium atmosphere. The tubes were treated with boiling HNO_3 for 24 h. The acid treated tubes are nearly always open ended and have a large number of acid sites on the surface, around 6×10^{20} sites g^{-1}. The tubes were treated with a metal oxide precursor and then dried in air at 100 °C and calcined at 450 °C. The samples were then heated at 700 °C to burn off the carbon. To produce tungsten rods Na_2WO_4 was passed through a cation exchange column, producing tungstic acid, H_2WO_4, which was stirred with the acid treated carbon tubes for 48 h. The yield of tungsten oxide rods was lower than the other metal oxides. The rods had diameters between 15 and 60 nm, with lengths of up to 5 μm, much larger than the starting nanotube. The rods were single crystals with a zone axis projection along [010]. It is thought that CO or CO_2 is evolved when the oxide coated tubes are heated and that the remaining metal or suboxide is reoxidised and recrystallizes, or that decomposing material gives crystals, elongated by the movement of gas.

Several groups using tungsten oxide precursors and hydrothermal methods have produced nanorods. Using hexadecylamine and citric acid as a template and structure modifying agent respectively a gel was produced by heating an aqueous solution of $(NH_4)_{10}W_{12}O_{41}.7H_2O$ and citric acid at 120 °C for 4 h[124]. The amine was dissolved in ethanol and added to the gel, which was stirred for a further 10 h. This mixture was placed in a Teflon vessel in a steel autoclave at 180 °C for a week. The rods had diameters within the range 5 – 50 nm and lengths of between 150 and 250 nm and were hexagonal single crystalline WO_3. The rods were reduced to WS_2 nanotubes by heating with H_2S gas.

Hexagonal WO_3 nanowires were produced by the hydrothermal reaction of tungstic acid, H_2WO_4, lithium sulfate, Li_2SO_4 and oxalic acid, $H_2C_2O_4$. SEM of the product shows the presence of large rod-like structures 200 - 400 nm in diameter and

2.5 - 10 μm in length. Closer inspection of these rods revealed that they were in fact composed of many nanowires, 5 – 15 nm in diameter. The sulfate and oxalic acid were structure directing and dispersing agents, necessary to the production of bundles of hexagonal phase rods[125].

Single crystalline $W_{18}O_{49}$ nanorods were produced from a hydrothermal method using tungstic acid[126]. Na_2SO_4 was added to freshly prepared H_2WO_4 and the mixture placed in a Teflon lined autoclave at 160 °C for between 2 and 24 h. The rods have diameters between 3 and 15 nm and lengths in the micrometer range.

Heating tungsten metal to high temperatures in the presence of other materials has been a successful route to tungsten oxide rods. Heating a tungsten foil partly covered with a SiO_2 plate in an Ar atmosphere to 1600 °C produced interesting micrometer tree-like structures[127]. When the product was subjected to ultrasonic treatment, the trees broke into nanoneedles and particles. The needles were monoclinic $W_{18}O_{49}$ with diameters of 10 – 50 nm. The same group then converted these needles into WS_2 nanotubes[128] by replacing the Ar with H_2S and reducing the temperature to 1000 °C. The tubes had diameters of 10 – 100 nm, lengths of 5 –30 μm and many had fully open tips

Monoclinic WO_2 nanowires have been produced by heating a tungsten wire which had partly been wrapped with melted boron oxide (B_2O_3) powder to 1600 °C in a nitrogen atmosphere[129]. The nanowires were observed on the surface of the wire with diameters of 10 – 30 nm and lengths of 2- 5 μm.

A similar method, carried out by H. Zhang et al[130], also produced tungsten oxide nanorods. Electrochemically etched tungsten tips were heated in a furnace under different atmospheres, the nanorods had an average diameter of 20 nm and lengths of 1–2 μm. Heating the tips at 830 °C under a H_2 and Ar mixture produced monoclinic sub

stoichometric WO_3 rods, whilst heating to 800 °C and 900 °C under Ar produced $WO_{2.9}$ and $W_{18}O_{49}$ rods respectively.

Three dimensional tungsten oxide nanowire networks were synthesised by the thermal evaporation of W powders in the presence of oxygen[131]. The tungsten was heated in a tungsten boat to 1400 – 1450 °C and the networks grew on substrates mounted above the boat, where the deposition temperature is around 950 °C. The nanowires were single crystalline cubic $WO_{2-\delta}$ with diameters of between 10 and 180 nm.

In an infrared irradiation heating furnace, tungsten filaments were heated to 950 – 1000 °C, with a silica wafer positioned below the filament acting as a substrate. The rods were single crystalline monoclinic WO_3 with diameters ranging from 20 to 100 nm[132].

Single crystalline $W_{18}O_{49}$ nanorods were produced when tungsten metal was heated to 800 – 1000 °C with water in a furnace[133]. The rods were extremely long, with lengths of up to 100 μm, and diameters of 20 – 400 nm, but mainly below 200 nm. It is thought that nucleation of $W_{18}O_{49}$ crystals occurs after water vapour causes the hydrolysis of the W-O-W bonds in the WO_2 layers formed on the stage. These crystals then grow into rods.

Nanorods with relatively small diameters were produced when $W(CO)_6$ reacted with $(CH_3)_3NO.2H_2O$ and excess oleylamine at 270 °C in a Schlenk tube, followed by various treatments in organic solvents[134]. The colloidal $W_{18}O_{49}$ rods had diameters of 3 – 6 nm and lengths of around 75 nm.

Nanowires with diameters of 10 – 50 nm and lengths of up to several micrometers were produced by the removal of surfactant from cetyltrimethylammonium intercalated tungsten oxide at high temperatures[135]. The

lamellar product was synthesised by the co-condensation of sodium tungstate, Na_2WO_4, and cetyltrimethylammonium bromide under hydrothermal conditions. This material was placed in a tube furnace and calcined at 720 °C for 2 h then cooled to room temperature, producing nanowires. The wires were monoclinic $W_{18}O_{49}$.

When a solution of $W(CO)_6$ in diphenylmethane was subjected to ultrasonic irradiation in the presence of an Ar/O_2 mixture at 90 °C an amorphous powder was formed. When this was heated to 550 °C snowflake-like particles were produced. Further heating of this product to 1000 °C produced nanorods 20 - 50 nm in diameter and 50 – 500 nm long[136].

Tungsten oxide, WO_3, is an electrochromic material that has attracted considerable attention due to its optical properties. Electrochromisim is defined as when a change in colour arises from an applied voltage. Electrochromic devices have many applications in smart windows, mirrors, displays, and optical switching devices due to their properties of low power consumption (<2 V), high coloration efficiency, and memory effects under open circuit conditions.[137] Tungsten oxide also has potential applications in catalysis and as the negative-electrode materials for lithium-ion batteries[138].

Mesoporous semiconducting films of tungsten trioxide have been prepared using the sol-gel technique. The films of preferentially orientated monoclinic-phase nanocrystals were prepared by adding a stabilising organic additive, such as polyethylene glycol, to a solution of tungstic acid, which was spread on a conducting glass substrate and annealed. The well crystallized films gave good photoresponse in the blue region of the spectrum and have applications in photoelectrochemical and electrochromic devices[139].

Using sputtering and lamination, a solid electrochromic device containing WO_3, $Ni(OH)_2$ and Ta_2O_5 as a protective layer was prepared. The device had good durability, response time and high coloration efficiency[137].

Films of tungsten trioxide have been used as a fast "writing-reading-erasing" memory device using a scanning electrochemical microscope[140]. This is possible because tungsten oxide undergoes a reversible reduction/oxidation process to form reduced tungsten oxide of mixed valence, with both states having different conductivity and colour.

Tungsten oxide has shown many applications in catalysis including olefin metathesis[141-144], oxidation of propene[145] and isomerisation of butene[146]. Carbon nanotubes loaded with WO_3 were prepared by wet impregnation with ammonium metatungstate pentahydrate, $(NH_4)_{10}W_{12}O_{41}.5H_2O$. The material was tested for C_6 olefin skeletal isomerization compared to a tungstated zirconia, WO_3/ZrO_2, catalyst and showed high conversion levels with no deactivation[147].

In the isomerisation of butene and cyclopropene, WO_3 supported on Al_2O_3, ZrO_2 and TiO_2 showed greater activity than WO_3 itself[146].

5.1.2 Aluminium oxide nanorods

Aluminium oxide, Al_2O_3, is a versatile ceramic with a wide range of applications. The aluminium atoms are octahedrally co-ordinated to 6 oxygen atoms in a cubic structure, as shown in Fig. 5.2.

Alumina is an excellent electrical insulator due to its high volume resistivity and dielectric strength, which makes it ideal for use in electronic connectors and insulators for spark plugs in cars. High purity aluminium oxide is used in orthopaedic

implants. The material is wear and abrasion resistant and is used in linings for pipes, faucet seals and thread and wire guides. Powdered aluminium oxide is also used in chromatography.[148]

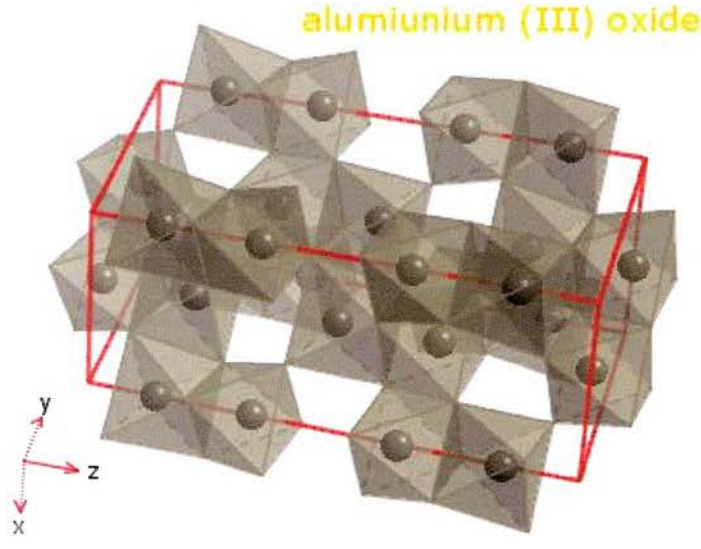

Fig. 5.2 Structure of Al_2O_3.

Nanotubes containing aluminium oxide have been produced using carbon tubes as templates and by electrochemical deposition, as previously described. Nanorods of Al_2O_3 have also been prepared by various methods, including atomic layer deposition and sintering. Most of the synthetic routes require extremely high temperatures or energy. There are many different crystal structures of Al_2O_3, the structure of $\alpha - Al_2O_3$ consists of a hexagonal close packed array of O^{2-} ions with the metal ions occupying two-thirds of the octahedral holes in an ordered array. Dehydration of aluminium hydroxide at temperatures below 900 °C leads to the formation of γ-Al_2O_3, a metastable polycrystalline form with a very high surface area.

Cubic γ-Al_2O_3 nanorods have been prepared by the DC electric arc discharge of Fe and Al powders. The diameters of the rods are relatively uniform, ranging from 20 to 30 nm. The proposed mechanism of formation is that a vapour-solid-vapour process

is assisted by a two dimensional vapour-solid nucleation and the rods grow from there[149]. γ-Al_2O_3 nanorods have also been synthesised by dehydration of a sol produced with aluminium isopropoxide[150]. The rods had diameters of less than 10 nm and lengths between 50 – 200 nm. The sol contained boehmite nanofibres and was produced with much less water than a normal sol.

Reacting aluminium metal with active carbon or graphite has produced Al_2O_3 nanotubes and rods[151]. Zinc oxide nanowires were also produced when ZnO was reacted with carbon nanotubes or active carbon. The aluminia tubes had outer diameters of 40 – 50 nm. The nanowires exhibited a d-spacing of 0.253 nm, which corresponds to the (104) plane, which were observed at 35° to the growth axis of the wire.

Sintering a mixture of Al and SiO_2 powders produced α-Al_2O_3 nanorods with diameters of 20 – 100 nm, lengths of 1 – 2 μm and slightly round or sharp tips[152]. The product is leached in HF – HNO_3 solution before the nanorods are collected.

α-Al_2O_3 nanotubes have been prepared from Al_4O_4C nanowires, which were made from a simple high temperature reaction[153]. An alumina crucible was placed in a furnace that contained a graphite rod heater, which was heated to 1600 °C. The green powder produced contained a high yield of nanowires, with diameters of 50 – 100 nm and lengths in excess of 10 μm. To produce nanotubes the wires were heated in a BN crucible by the same method and then oxidised in air at 800 °C.

Carbon nanotubes were coated and filled[154] with Al_2O_3 by atomic layer deposition of trimethyl aluminum at 300 °C. The alumina coating is amorphous and coats the tubes uniformly and then fills the inside of the multi walled tubes. The same group also coated zinc oxide nanorods with Al_2O_3 by atomic layer deposition[155]. The ZnO nanowires were synthesised by a thermal evaporation process on a Si substrate

and coated with Al_2O_3 by the same method. The rods were coated amorphously with a cylindrical shell of Al_2O_3.

Using a structure directing agent, nonionic triblock copolymer P123, nanorods of Ga_2O_3- Al_2O_3 have been synthesised. The rods have an average diameter of 10 nm and an average length of 50 nm[156] and are thought to be a promising material for lean-burn NO_x reduction.

5.1.3 Tantalum oxide nanorods

Ta_2O_5 is a ceramic with a wide range of applications. It is used to make capacitors in electronics, mobile phones and pagers, thin-film components and high-speed tools. Due to its high refractive index, Ta_2O_5 has been employed in the fabrication of the glass of many camera lenses[157].

There are at least two structurally distinct forms of tantalum oxide. The low temperature form is known as β-Ta_2O_5, and the high temperature form is known as α -Ta_2O_5. The transition point between the two forms is 1360 °C but the transition is very sluggish. The Ta atoms in β-Ta_2O_5 are 6 co-ordinated. This phase melts at 1785 °C. Due to the sluggish conversion it may melt before conversion into the α-phase[158]. The α-tantalum oxide is of the same general type as the β-tantalum oxide, but there is both 6- and 7-coordination of the metal atoms. Both orthorhombic and hexagonal phases are known. This phase melts at 1872 °C.

Very small tantalum oxide nanowires were produced using an atomic force microscope. The wires were between 2 and 6 nm high, with widths of 50 – 100 nm and a wide variety of lengths. A Ta film, which was deposited on a Si substrate, was oxidised using the AFM non-contact mode. An oscillating probe is placed about 10 nm above the sample surface and a cathodic voltage is applied to the probe and an anodic

voltage is applied to the Ta films to form a liquid bridge between the tip and sample and induce nano-oxidation[159].

Double walled nanotubes of Ta_2O_5, TiO_2 and ZrO_2 have been produced using steroidal derivatives as templates[160]. Sol-gel polymerisation of transition-metal alkoxides was carried out using 1,13-diamino-4,7,10-trioxadecanyl-13-butoxyl as a template. In the case of Ta, $Ta_2(OBu)_5$ was used to prepare the sol. The tubes had outer diameters of nearly 600 nm, with the walls being 50 nm thick.

Templates were also used in a sol-gel reaction to produce transition metal oxide nanotubes by Miyaji et al[161]. Tubes of TiO_2, Nb_2O_5, ZrO_2 and Ta_2O_5 were synthesised by coating the side faces of long needle like crystals of ammonium dl tartrate in metal oxide using the appropriate metal alkoxide. The crystal templates were removed, leaving hollow rectangular shaped tubes with rectangular inner channels. The tubes were 1 – 5 μm in diameter and 1.3 – 5.9 μm in length and were shown to be amorphous oxide gel by XRD.

Nanorods of Ta_2O_5 have been produced in the presence of poly L-lysine by a sol-gel process[162].

As well as the applications mentioned above, Ta_2O_5 has potential uses in catalysis and research into its use in other fields of electronics is ongoing.

Polymer thin film transistors that use Ta_2O_5 as gate insulators were produced by Seong et al[163]. Compared to conventional gate insulators Ta_2O_5 has a large dielectric constant, which enables the transistors to operate at a lower voltage. The insulator was prepared by anodizing a Ta gate electrode.

Thermally stable mesoporous Ta_2O_5 has been synthesised by a modified sol-gel process and has applications in photocatalysis[164]. The Ta_2O_5 is prepared using a neutral block co-polymer as a template, giving pore sizes of 3.5 nm. The NiO - loaded

mesoporous Ta_2O_5 photocatalyst exhibits high photocatalytic activity for the decomposition of water under ultraviolet light.

5.2 Results

5.2.1 Aluminium oxide

The reaction of aluminium oxide and 10 molar sodium hydroxide produced a high yield of nanorods, 70 %. The solid white product had fused to the base of the Teflon autoclave innard and a sample was scraped off and examined. Many nanorods were observed with a wide range of diameters, as shown in Fig. 5.3, and lengths of anywhere up to a few hundred nanometers (Fig. 5.4). The nanorods were crystalline in nature and EDX showed that material consists of Al and O with a weak Na signal (Fig. 5.5), caused by residual sodium after washing.

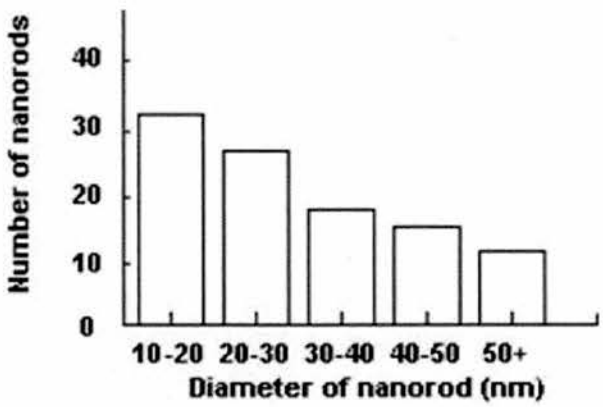

Fig. 5.3 Diameter distribution of Al_2O_3 nanorods.

In some areas the nanorods were surrounded by crystalline plate-like material, which are unreacted starting material, and many small particles and "messy looking" areas, shown in Fig. 5.4, which are formed by decomposition of the starting material in the strong reaction conditions. The three phases of reaction shown in the sample may

indicate that the full reaction is not complete, and that given a longer reaction time a higher yield of nanorods may be produced. However even at these reaction conditions decomposition is a competing reaction and may be the final product if the reaction is left to run for longer times.

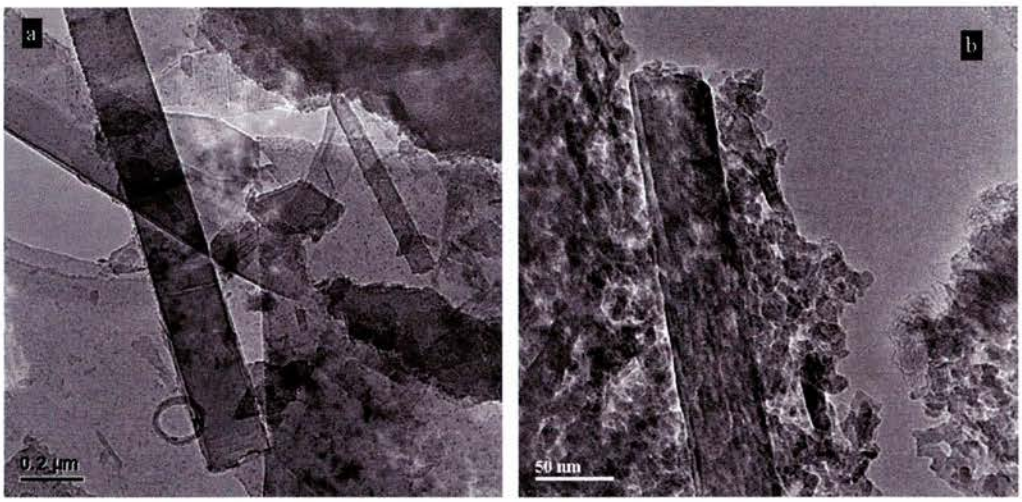

Fig. 5.4 TEM image of Al_2O_3 nanorods produced by the hydrothermal reaction of Al_2O_3 and 10 M NaOH.

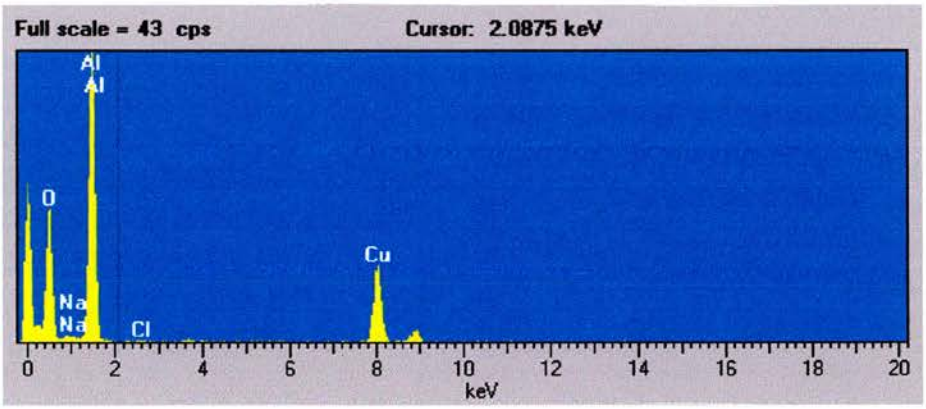

Fig. 5.5 Typical EDX spectrogram of the Al_2O_3 nanorods.

The material shown in Fig. 5.4 (b) looks very similar to the amorphous phase in the reaction of TiO_2, however this material was in fact crystalline.

The XRD pattern of the Al_2O_3 nanorods, shown in Fig. 5.6, is indexed based on monoclinic Al_2O_3 with unit cell parameters of a = 11.79 Å, b = 2.91 Å, c = 5.62 Å and

$\beta = 103.79^{\circ}$ and shows good agreement. An image of a nanorod is shown in Fig. 5.7. The lattice spacing of 4.65 Å corresponds to the (-201) plane, which runs parallel with the long axis of the nanorod. A spacing of 2.86 Å corresponds to the (002) plane, which runs at an angle of 41° to the nanorod growth axis. A spacing of 2.35 Å is also observed, which corresponds to the (111) plane, which runs at an angle of –23° to the nanorod growth axis. These values show good agreement with the results from the powder XRD pattern, showing that the rods have a monoclinic Al_2O_3 structure.

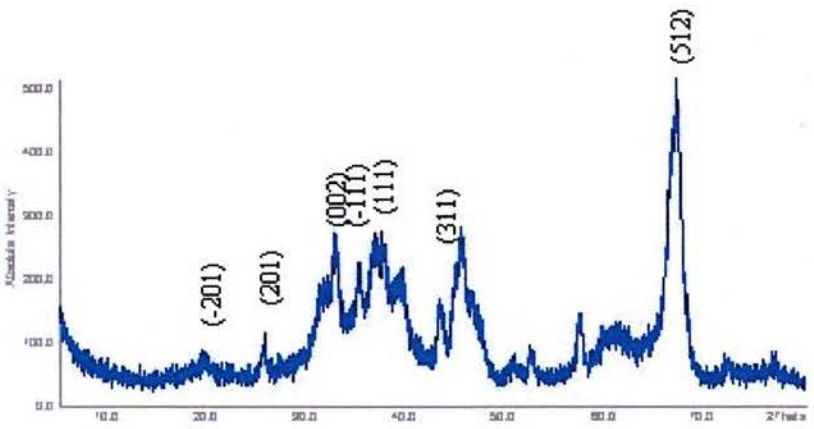

Fig. 5.6 XRD pattern of Al_2O_3 nanorods.

The nanorods are thought to be formed by cleavage of material from the Al_2O_3 parent crystals due to the harsh reaction conditions. Aluminium oxide is made up of AlO_6 octahedra. The structure of the rods is monoclinic Al_2O_3 as shown by SAED. This mechanism would explain the large range in diameter and length of the nanorods. There is no definitive size of rod that is prevalent in the reaction mixture, however the range of sizes may be more entropically stable than larger particles.

Some of the nanorods are found in bundles, shown in Fig. 5.8. In previous work, carbon nanotubes have been shown to stick together and form bundles[165]. This phenomenon was also observed in trititanate nanotubes. In this case it is more likely

that the bundle is a single Al_2O_3 particle that is in the process of breaking up into nanorods rather than independent rods aggregating. This would appear to be further evidence of the postulated mechanism, nanorods of Al_2O_3 are cleaved off from particles of aluminium oxide due to the reaction of 10 molar NaOH.

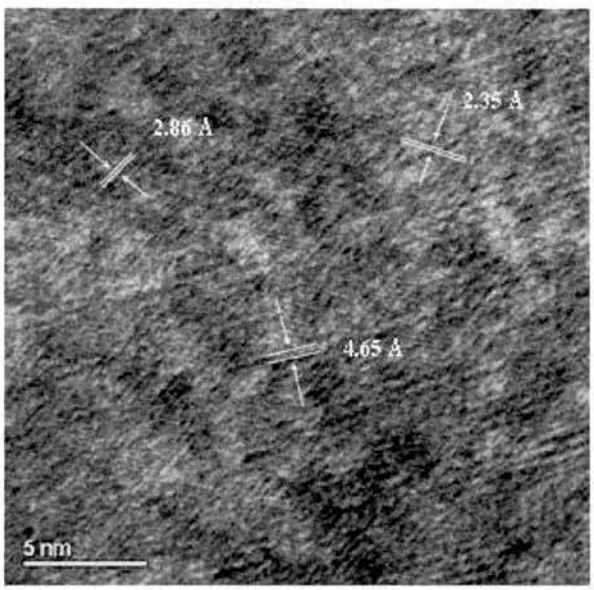

Fig. 5.7 TEM image of an Al_2O_3 nanorod and the corresponding SAED pattern.

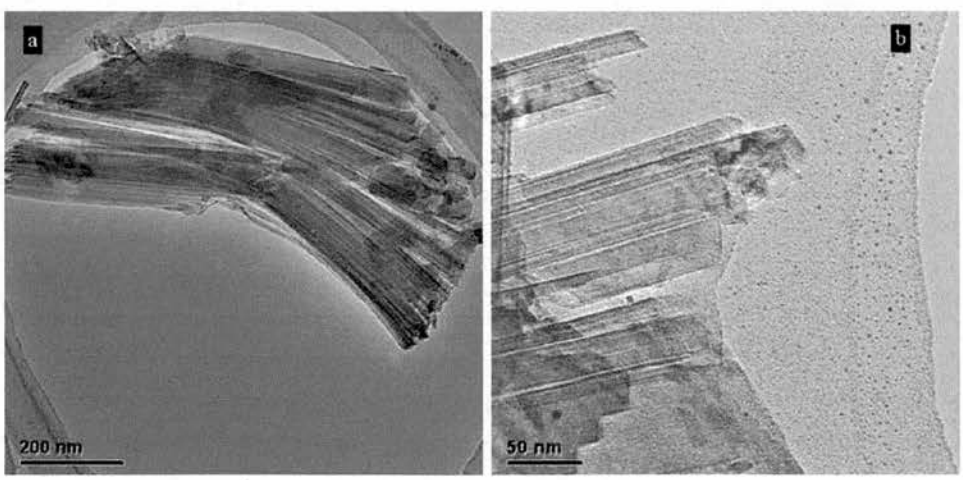

Fig. 5.8 a) TEM image of agglomerated Al_2O_3 rods, b) Higher magnification TEM image of Al_2O_3 rods.

5.2.2 Tantalum oxide

The hydrothermal reaction of tantalum (V) oxide and 10 molar sodium hydroxide solution produced a small yield of nanorods, with most of the product being unreacted starting material, shown in Fig. 5.9. The same reaction mechanism as for the production of aluminium oxide nanorods is proposed, and at these reaction conditions only a small percentage of material reacts successfully. The reaction was run at 170 °C for 48 hours. It is believed that if the temperature and reaction time were increased the yield of nanorods would increase.

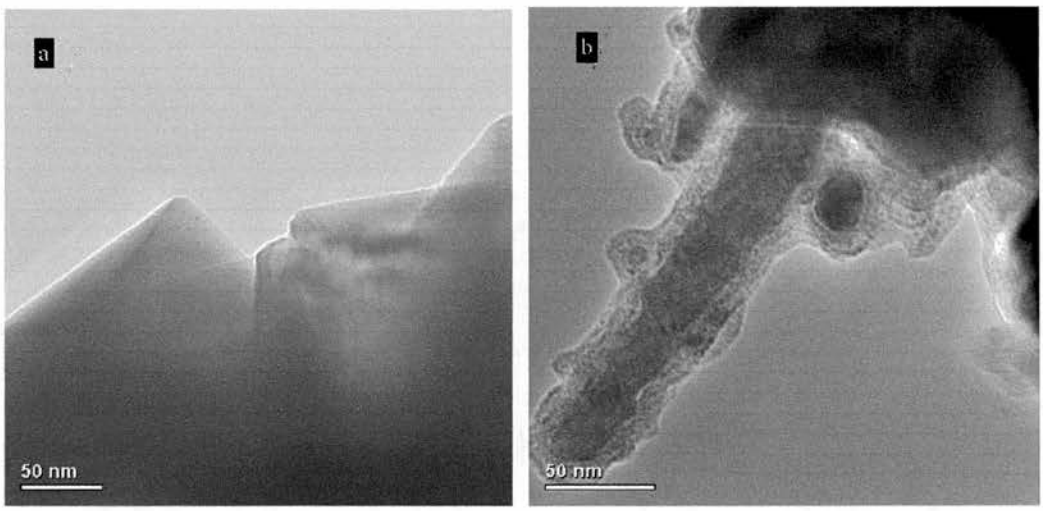

Fig. 5.9 TEM images of a) unreacted starting material and b) Ta_2O_5 nanorod.

The nanorod shown in Fig. 5.9 b) is 25 nm in diameter and 188 nm in length and is surrounded by amorphous material. This may be part of the rod that has further reacted with the strong base.

Tantalum pentoxide was also reacted with butyl amine in water using the same method which had produced nanotubes from ion exchanged niobate, in a templating reaction. This reaction produced nanorods (Fig. 5.10) whose lengths were in excess of 200 nm and had a range of diameters, as shown in Fig. 5.11. The average diameter of

the nanorods was 32 nm. A similar mechanism of production as for the aluminium oxide nanords is proposed, with the amine molecules intercalating into the structure and cleaving off the rods. The reaction occurs at room temperature, with stirring being the only energy added.

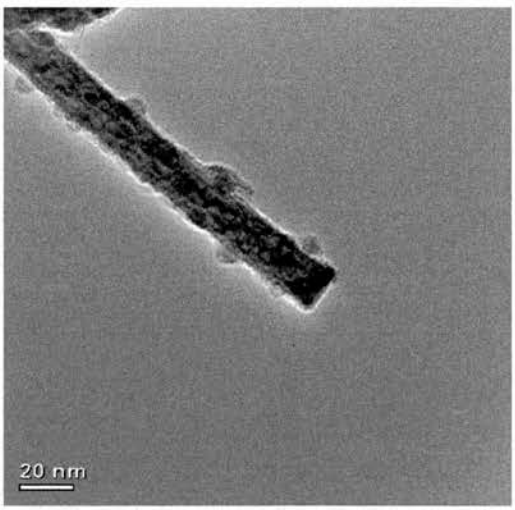

Fig. 5.10 TEM image of Ta_2O_5 nanorod produced by the reaction of butyl amine and Ta_2O_5 at room temperature.

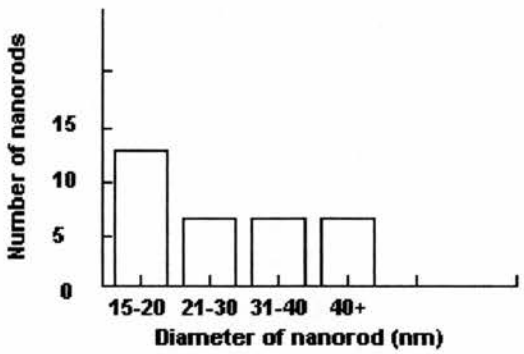

Fig. 5.11 Diameter distribution of Ta_2O_5 nanorods produced by reaction of Ta_2O_5 and butyl amine at room temperature.

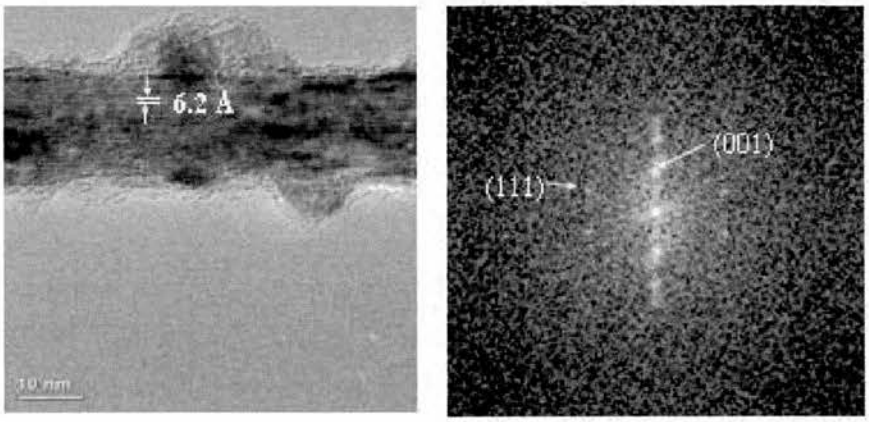

Fig. 5.12 High magnification TEM image of a Ta_2O_5 nanorod and the corresponding SAED diffraction pattern.

The SAED pattern of a nanorod is shown in Fig. 5.12, and is indexed based on hexagonal Ta_2O_5 with unit cell parameters of a = 7.24 Å and c = 11.61 Å. The lattice spacing of 6.2 Å corresponds to the (001) plane, which runs parallel with the long axis of the nanorod. A spacing of 3.44 Å corresponds to the (111) plane. The nanorods have a hexagonal Ta_2O_5 structure.

Fig.5.13 Nanorods produced by the reaction of Ta_2O_5 and $(C_2H_5)_4NOH$ at room temperature.

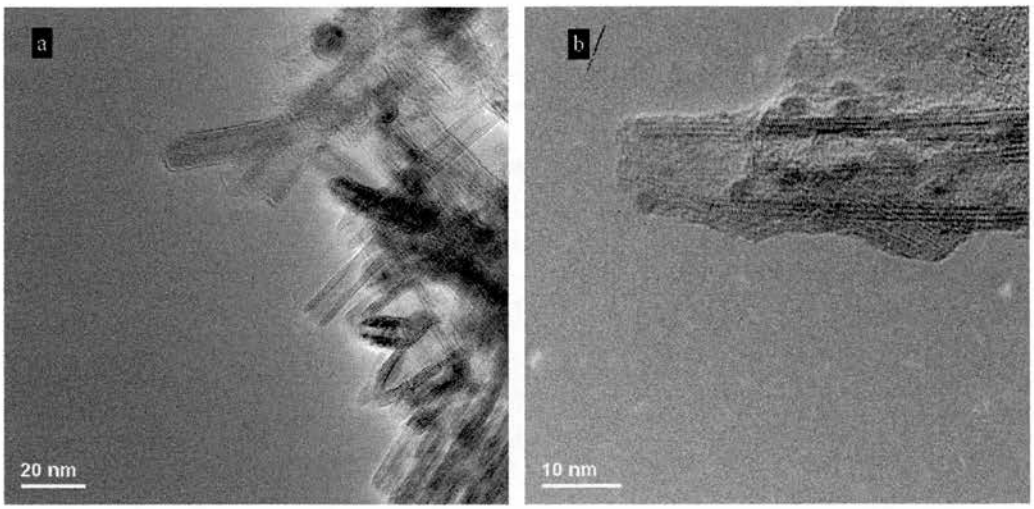

Fig. 5.14 Nanotubes produced by the reaction of Ta_2O_5 and $(C_2H_5)_4NOH$.

In the reactions of amines with ion exchanged niobate the amine molecules are protonated by the H^+ ions within the structure. There are no such protons in Ta_2O_5 so the reaction was repeated with tetraethylammonium hydroxide, which provides a positive amine. This reaction produced a mixture of nanords and nanotubes, as shown in Fig. 5.13 and Fig.5.14.

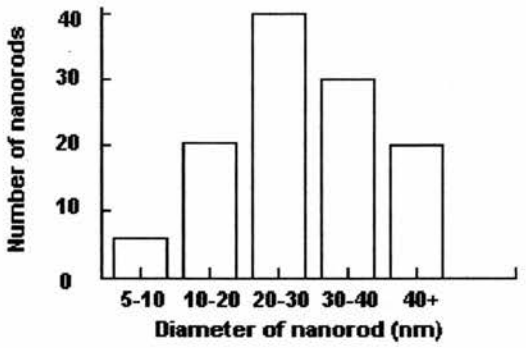

Fig. 5.15 Diameter distribution of Ta_2O_5 nanorods produced by reaction of Ta_2O_5 and tetraethylammonium hydroxide at room temperature.

The diameter of the nanorods showed a wide distribution, shown in Fig. 5.15, with an average diameter of 31 nm. The rods all had lengths in excess of 1 μm. The

mechanism of formation of the nanorods is thought to be the same in this reaction as before, with the amine molecules breaking the Ta_2O_5 crystal particles into smaller rods. The images in Fig. 5.16 further illustrate the postulated mechanism, showing a tantalum oxide particle breaking into rods. The rods were crystalline and contained tantalum and oxygen, which was determined by EDX, shown in Fig. 5.17.

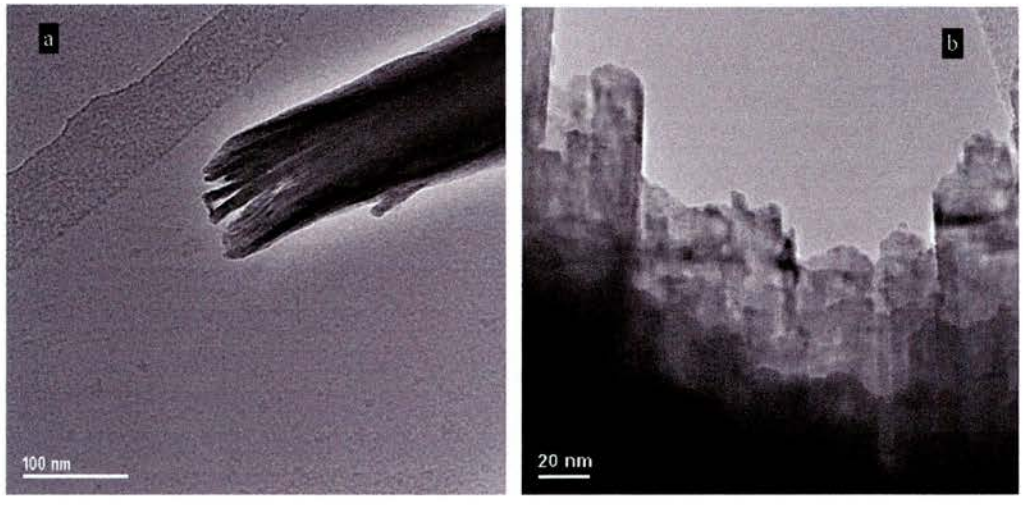

Fig. 5.16 a) Low magnification and b) higher magnification TEM images of a Ta_2O_5 particle breaking into nanorods.

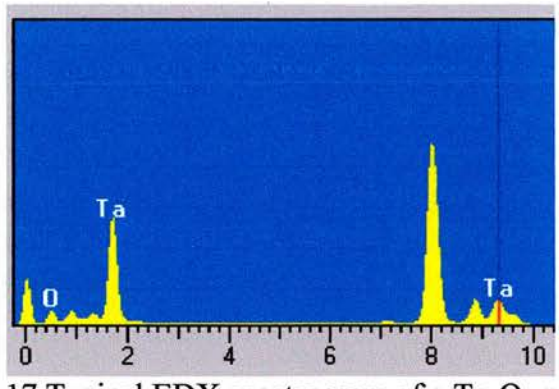

Fig. 5.17 Typical EDX spectrogram of a Ta_2O_5 nanorod.

The nanotubes had a much smaller diameter distribution, shown in Fig. 5.18, with an average diameter of 8.8 nm. The number of shells in each tube was either three or four, with many tubes having more layers on one side than the other, as shown in

Fig. 5.19, which is indicative of a scrolled structure. The tubes had an interlayer spacing of 0.66 nm and lengths between 60 and 200 nm and are open at both ends.

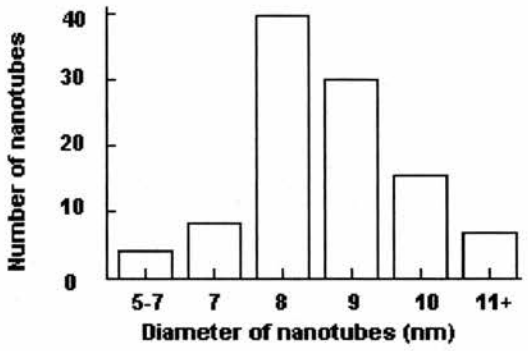

Fig. 5.18 Diameter distribution of Ta_2O_5 nanotubes produced by reaction of Ta_2O_5 and tetraethylammonium hydroxide at room temperature.

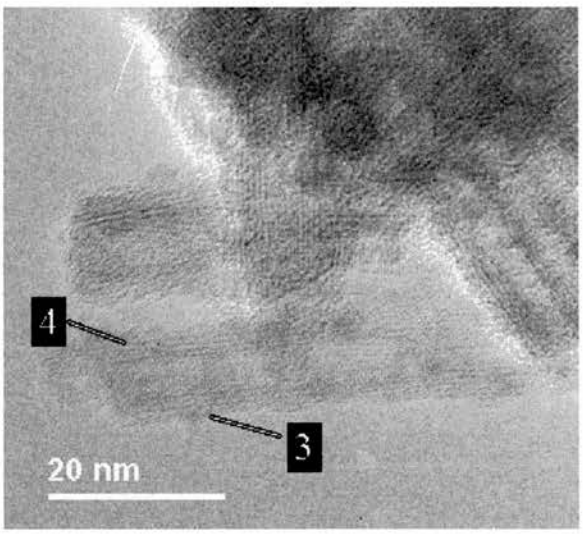

Fig. 5.19 TEM image of a Ta_2O_5 nanotube with 3 layers on one side and 4 layers on the other.

The SAED pattern of a nanorod is shown in Fig. 5.20, and is indexed based on hexagonal Ta_2O_5 with unit cell parameters of a = 7.24 Å and c = 11.61 Å. The lattice spacing of 6.2 Å corresponds to the (001) plane, which runs parallel with the long axis

of the nanorod. A spacing of 3.46 Å corresponds to the (111) plane. The nanorods have a hexagonal Ta_2O_5 structure.

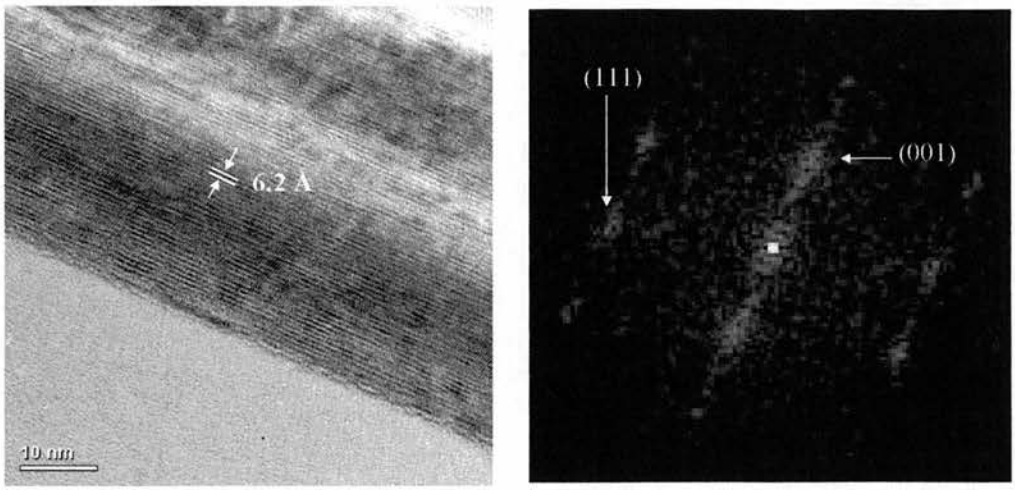

Fig. 5.20 High magnification TEM image of a Ta_2O_5 nanorod produced by reaction of Ta_2O_5 and tetraethylammonium hydroxide at room temperature and the corresponding SAED pattern.

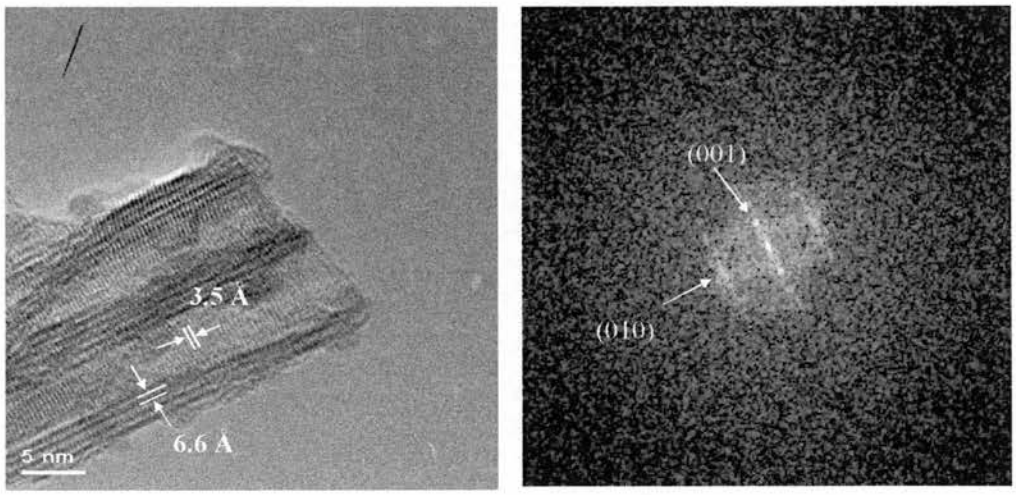

Fig. 5.21 High magnification TEM image of a Ta_2O_5 nanotube produced by reaction of Ta_2O_5 and tetraethylammonium hydroxide at room temperature and the corresponding SAED pattern.

The SAED pattern of the nanotube is shown in Fig. 5.21, and is indexed based on hexagonal Ta_2O_5 with unit cell parameters of a = 7.24 Å and c = 11.61 Å. A spacing of 3.34 Å corresponds to the (111) plane, which runs perpendicular to the long axis of the nanotube. The interlayer spacing in the nanotubes is 6.2 Å, which corresponds to the (001) plane of Ta_2O_5. The nanotubes have a hexagonal Ta_2O_5 structure.

The tubes are thought to form when a thin crystal sheet (Fig. 5.22) is cleaved off from the starting material rather than nanorods, These sheets then scroll to produce nanotubes. The driving force for the scrolling of sheets into tubes may result from an asymmetry in the sheet, which causes scrolling to release strain, however the nanosheets may just curl and scroll naturally into tubes after they are exfoliated. As no nanotubes were produced when butyl amine was used as a reactant, either the size of the amine, which is more sterically hindered and bulky than butyl amine or the fact that the amine is protonated results in the exfoliation of nanosheets, and therefore the production of nanotubes.

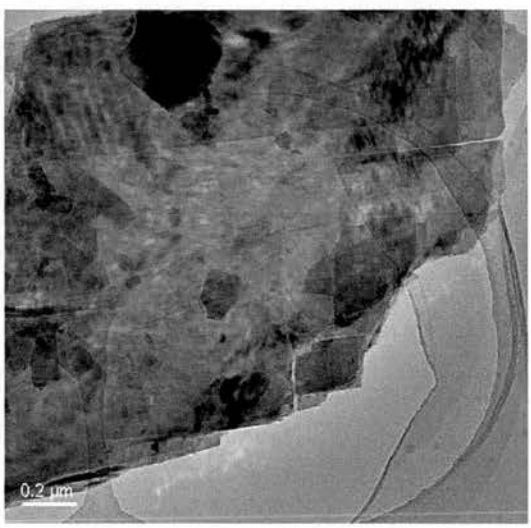

Fig. 5.22 Thin plate like material of Ta_2O_5.

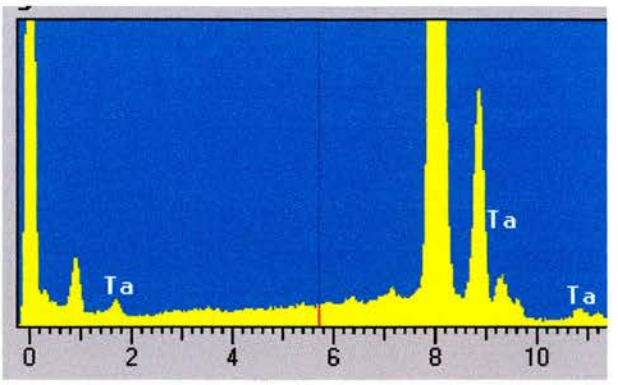

Fig. 5.23 EDX spectrum of a Ta_2O_5 nanotube.

The nanotubes did not contain any structural amine molecules, shown by a lack of nitrogen in the EDX spectrum, Fig. 5.23, which indicates that the role of the amine in the reaction is purely one of exfoliation/cleavage.

The tubes were found in bunches, often with two tubes stuck together, this can be seen in Fig. 5.21. This aggregation has also been observed in the trititanate tubes and occurs due to electrostatic attraction and the low density of the tubular material.

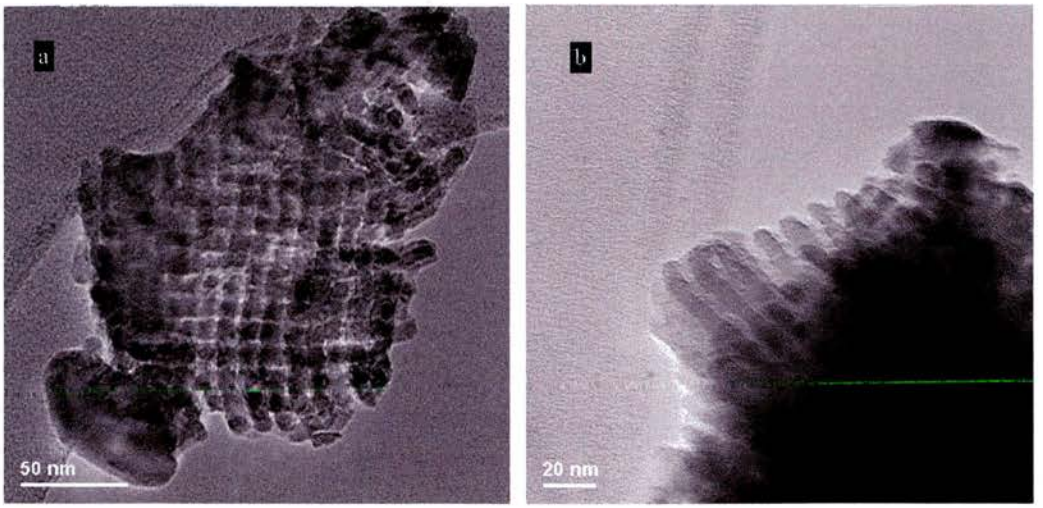

Fig. 5.24 TEM images of Ta_2O_5 nanorods self assembled.

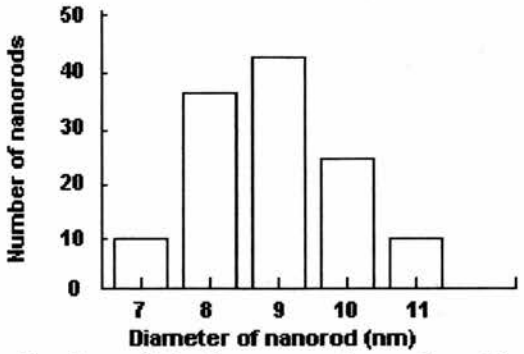

Fig. 5.25 Diameter distribution of Ta_2O_5 nanorods produced by reaction of Ta_2O_5 and tetraethylammonium hydroxide at room temperature and then dried at 160 °C.

The product of the reaction is sticky, even after filtration and drying in air. A sample containing rods and tubes was heated to 160 °C in order to remove water. When this dried sample was examined, only rods were present, and the rods self assembled into arrays, shown in Fig. 5.24. The nanorods had smaller diameters than those in the previous samples and also a narrow distribution of diameters, shown in Fig. 5.25.

The self-assembled nanorods are similar in dimension to the nanotubes present in the wet sample. The average diameter of the rods was 8.5 nm, compared to 32 nm for the independent rods in the wet sample and 8.8 nm for the nanotubes. The lengths of the self-assembled rods were also comparable to the nanotubes. The nanorods are related to the nanotubes rather than the other rods.

The SAED pattern of a nanorod is shown in Fig. 5.26, and is indexed based on hexagonal Ta_2O_5 with unit cell parameters of a = 7.24 Å and c = 11.61 Å. A lattice spacing of 2.58 Å corresponds to the (2 -1 0) plane. Perpendicular to this plane, a spacing of 2.07 Å is observed, which is indexed as (0 3 2). The (2 -1 0) planes are at an angle of 43° to the rod axis. The nanorods have a hexagonal Ta_2O_5 structure.

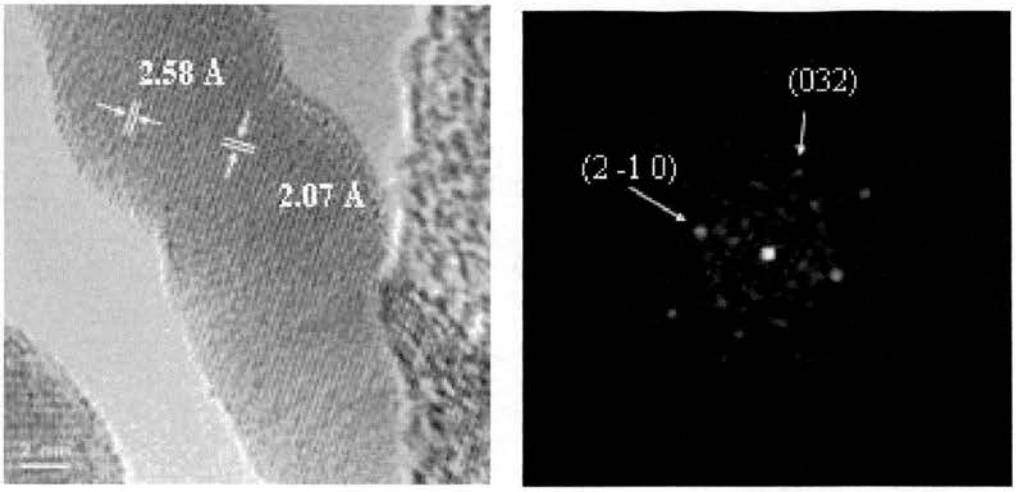

Fig. 5.26 HRTEM image of a Ta_2O_5 nanorod produced by heating a sample of Ta_2O_5 rods and tubes to 160 °C and the corresponding SAED pattern.

Due to the size of the nanorods, it is thought at this stage that the nanotubes, which are thermally unstable, decompose to form nanorods upon heating. This phenomenon has been observed in work on trititanate nanotubes. There are no structural amine molecules between the nanotube layers so heating either removes water molecules or directly decomposes the layers, resulting in rods. The rods self assemble due to the attraction between the parent nanotubes, which is seen in Fig. 5.21, and the energy put in by heating. The structure of the rods is also different from the rods produced directly from Ta_2O_5 and tetraethylammonium hydroxide, where the planes run parallel to the rod axis. In this case the (2 -1 0) planes run at 43° to the rod axis, suggesting a different method of formation, which is thought to be the decomposition of the nanotubes. Some of the larger diameter nanorods were also present in this sample.

When Ta_2O_5 and tetraethylammonium hydroxide were subjected to a hydrothermal reaction at 160 °C for 48 hours the starting material particles had agglomerated into larger fused particles, shown in Fig. 5.27, with sizes in excess of 1

μm. It was thought that the increase in temperature would enhance the templating reaction of the amine, however the desired reaction has not occurred.

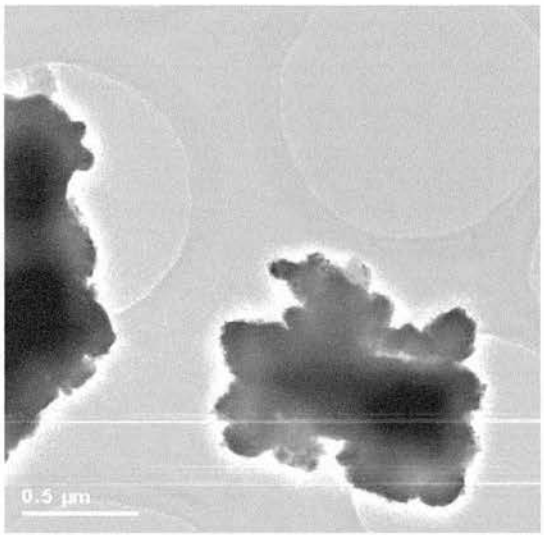

Fig. 5.27 Low magnification TEM image of Ta_2O_5 particles after hydrothermal reaction with tetraethylammonium hydroxide.

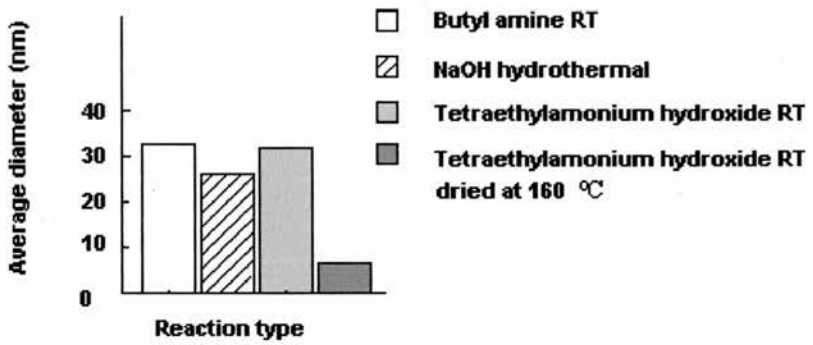

Fig. 5.28 Average diameter of Ta_2O_5 nanorods produced by various methods.

Using the same tantalum precursor, nanorods of different diameter have been produced by different methods, shown in Fig. 5.28. The hydrothermal reaction between Ta_2O_5 and 10 molar NaOH produced rods with an average diameter of 25 nm. Stirring Ta_2O_5 at room temperature with butyl amine and tetraethylammonium hydroxide produced rods of similar dimensions, however the later reaction also produced

nanotubes with an average diameter of 8.8 nm. When a sample containing rods and tubes was heated to 160 °C to drive off the water present, the tubes were converted to nanorods, which self-assembled into arrays and had an average diameter of 8.5 nm.

5.2.3 Silicon dioxide

The hydrothermal reaction of SiO_2 with 10 molar sodium hydroxide solution did not produce any tubes or rods, with most of the crystalline starting material remaining unreacted, shown in Fig. 5.29

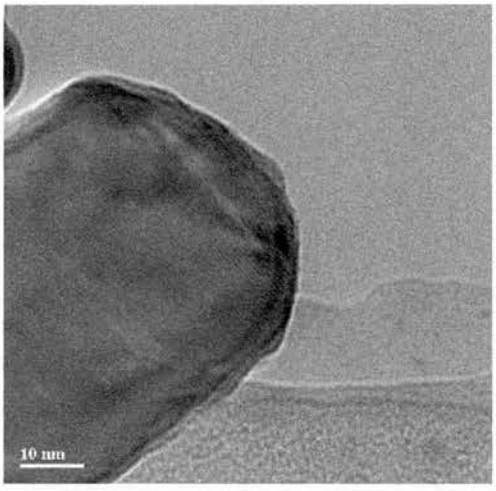

Fig. 5.29 TEM image of product of reaction between SiO_2 and 10 M NaOH.

5.2.4 Tungsten oxide

Tungsten oxide was reacted with 10 molar sodium hydroxide solution in a sealed autoclave at 160 °C for 24 hours. This reaction did not produce any nanorods or tubes. The starting material is a light green powder and the product is comprised of large (0.5-1 cm) bright green crystals. The material was examined using TEM, mass spectrometry and NMR. The starting material, WO_3, is a connected 3-D network.

The product was crystalline and contained warped layered structures, shown in Fig. 5.30. This material is markedly different from the starting material under the microscope as well as to the naked eye. The mass spec showed that, along with WO_3, other oxides of tungsten were present, as well as a mixed metal oxide peak for $NaWO_8$, shown in Fig. 5.31. The NMR results were inconclusive, as the product would not dissolve in a solvent.

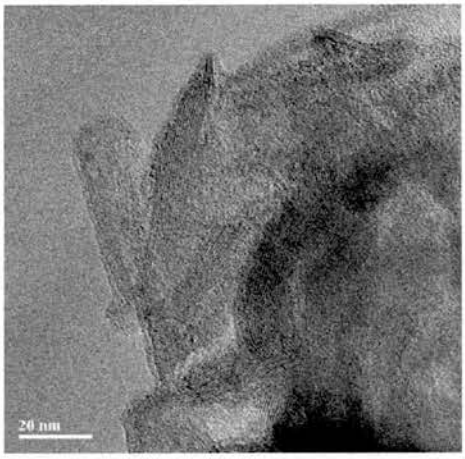

Fig. 5.30 TEM image of product of reaction between WO_3 and 10 M NaOH.

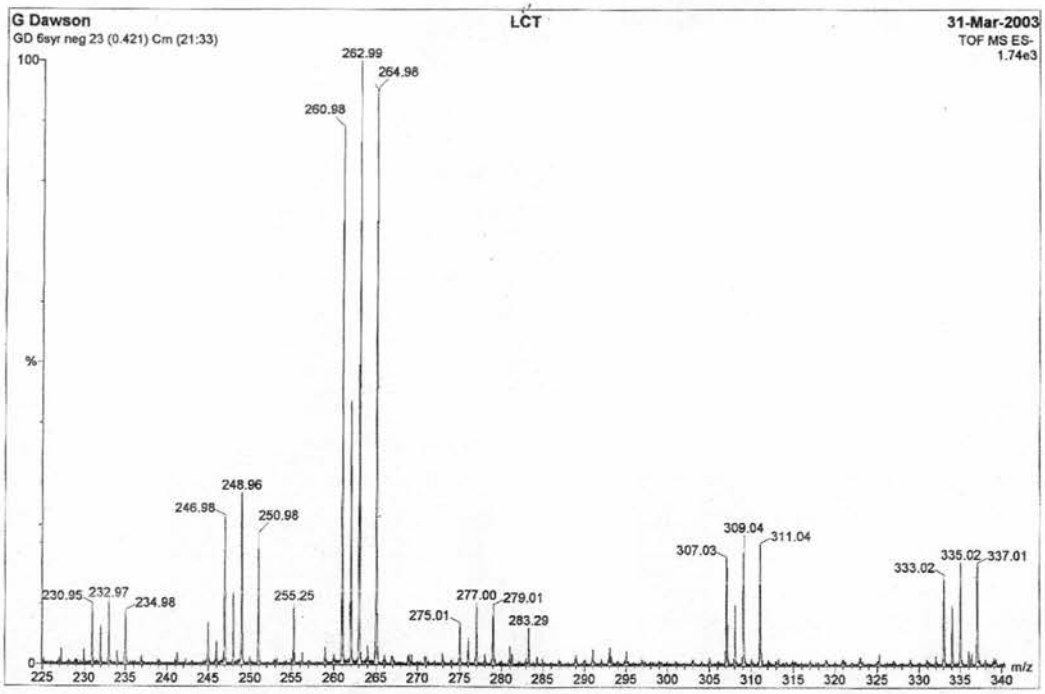

Fig. 5.31 Mass spectrum of WO_3 reacted with 10 M NaOH in sealed autoclave.

The reaction of tungsten oxide and butyl amine in water at room temperature produced a high yield of tetragonal WO_3 nanorods, shown in Fig. 5.32. The diameter range of the rods was not as wide as for the tantalum rods, with most rods having diameters between 7 and 13 nm, shown in Fig. 5.33. The average diameter of the tungsten rods was 12.9 nm.

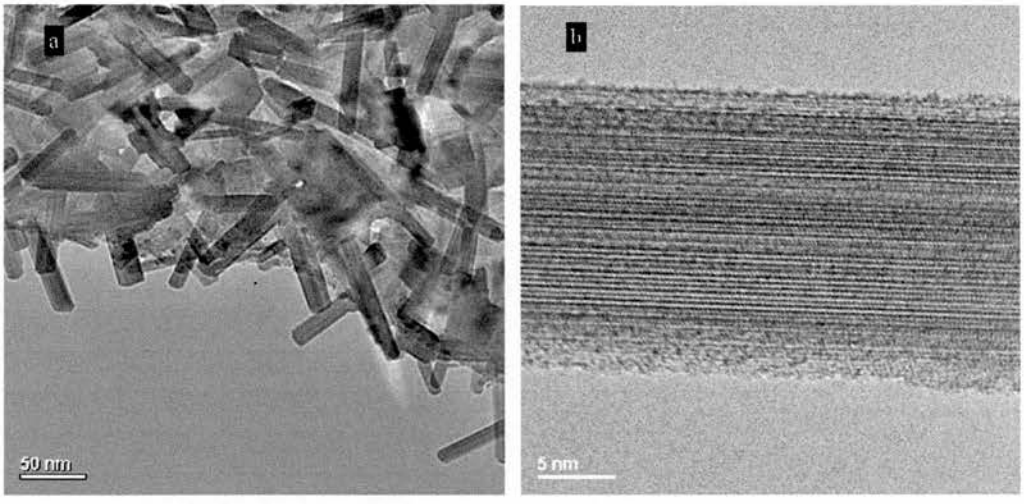

Fig. 5.32 TEM of WO_3 nanorods produced from the reaction of WO_3 and tetraethylammonium hydroxide in water at room temperature.

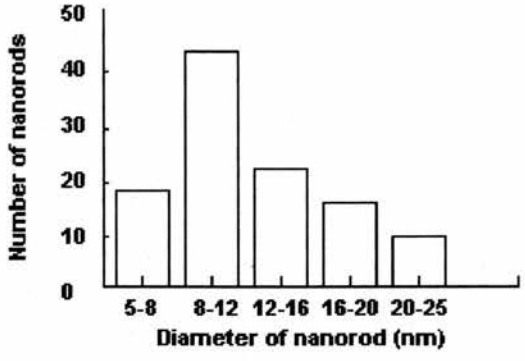

Fig. 5.33 Diameter distribution of WO_3 nanorods produced by the reaction of WO_3 and tetraethylammonium hydroxide.

The rods predominantly had lengths of less than 100 nm and did not contain any amine molecules, only tungsten and oxygen, shown by Fig. 5.34.

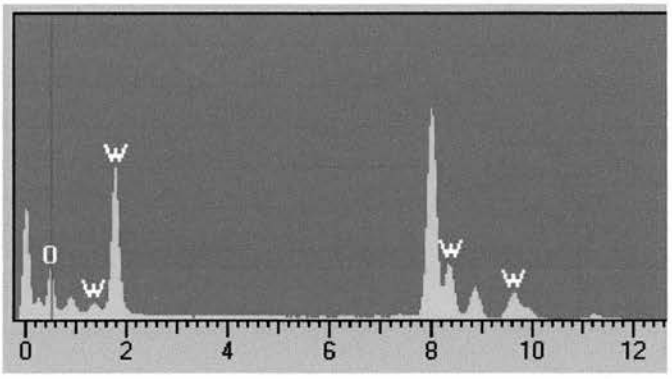

Fig. 5.34 EDX spectrum of WO_3 nanorod.

The formation mechanism for the tungsten rods is thought to be the same as the postulated mechanism for the tantalum rods. The amine cleaves off the rods from the parent WO_3 crystals.

The driving force to produce rods must be large, as it has to overcome the energy of the W-O bonds without the input of heat energy. The bond energy for W-O is 672 ± 42 kJmol^{-1}.

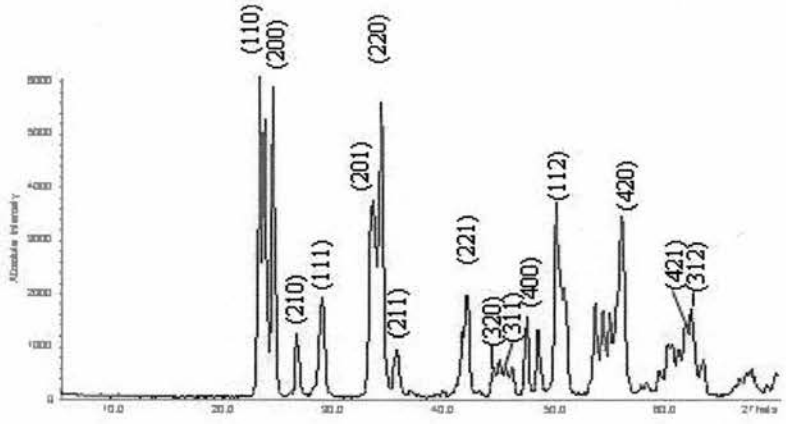

Fig. 5.35 XRD pattern of WO_3 nanorods produced by the reaction of WO_3 and butyl amine at room temperature.

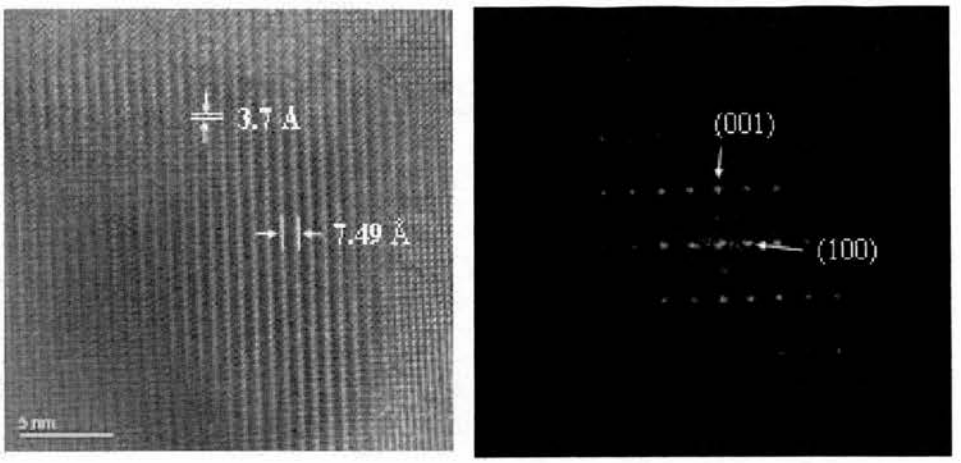

Fig. 5.36 HRTEM image of a WO_3 nanorod produced by the reaction of WO_3 and tetraethylammonium hydroxide at room temperature and the corresponding SAED pattern.

The XRD pattern of the WO_3 nanorods, shown in Fig. 5.35, is indexed based on tetragonal WO_3 with unit cell parameters of a = 7.39 Å and c = 3.88 Å and shows good agreement. The SAED pattern of a nanorod is shown in Fig. 5.36. The lattice spacing of 7.49 Å corresponds to the (100) plane, which runs parallel with the long axis of the nanorod. A spacing of 3.7 Å corresponds to the (001) plane, which runs perpendicular to the nanorod growth axis. These values show good agreement with the results from the powder XRD pattern, showing that the rods have a tetragonal WO_3 structure.

The attempt to produce nanotubes from various metal and non metal oxides by the same methods described in previous chapters had surprising results. The hydrothermal reaction of oxide with 10 molar sodium hydroxide in a sealed autoclave produced nanorods in the cases of Al_2O_3 and Ta_2O_5. The rods were of similar dimensions, with average diameters of 37.6 nm and 25 nm respectively. The lengths of the rods were around 200 nm in both cases. In the case of SiO_2 and WO_3 no rods or tubes were produced.

Stirring the parent oxide with amine in water at room temperature produced nanorods from WO_3 and Ta_2O_5. When tetraethylammonium hydroxide was used with Ta_2O_5 nanotubes were produced along with the nanorods. When a sample containing tubes was heated to remove water the tubes decomposed into nanorods, which self-assembled. The rods from tungsten oxide are considerable smaller than the corresponding tantalum rods, with lengths of less than 100 nm compared to greater than 1 μm for the tantalum rods. The self-assembled tantalum rods were of the same order as the nanotubes, with diameters of 8.5 nm and lengths of around 100 nm.

Chapter 6 Conclusion

6.1 Trititanate Nanotubes

In order to elucidate the formation mechanism of trititanate nanotubes, the hydrothermal reactions of titanium dioxide and 10 M sodium hydroxide solution were run at 2-hour intervals up to 24 hours. A high yield of nanotubes is formed after 72 hours, however after 24 hours many tubes are present.

In the samples four phases were found. The first phase is the crystalline starting material, rutile titanium oxide. This material is polyhedral and crystalline with a large size range.

The second phase is the amorphous material. This phase contains Ti, O and Na in a disordered state, as shown by EDX. When a sample was washed excessively no sodium was found in the amorphous phase. This shows that the sodium ions are weakly bound to the Ti and O. The harsh reaction conditions have broken the strong Ti-O bonds to create an amorphous phase.

The third phase contains thin plates of trititanate, $H_2Ti_3O_7$. These plates are formed when single sheets of trititanate extrude out of the amorphous phase and couple to form layered plates. It is these layers that scroll to form the nanotubes.

The nanotubes have a scroll structure. The number of shells in a single tube is ordinarily 4, with a diameter of ~ 8 nm. The tubes are hollow, with an intershell spacing of 0.78 nm.

The concentration of hydroxide ions is higher on the surface of the top layer than it is between the layers. Therefore the side in contact with the solution undergoes much more frequent collisions with the sodium and hydroxide ions. The energy gain for an OH^- ion to remove a H^+ ion from the crystal surface is high, as much as 2 eV, so it is very likely that the H^+ ion will be neutralised to form a water molecule. The

sodium ions in solution balance the charge on the surface layer. The hydrogen content of the crystal sheet is now asymmetric. When hydrogen is bonded to the surface the relevant Ti-O bond is lengthened. When the hydrogen is removed the bond will contract and this will cause the surface to curve. The strain in the layer will eventually overcome the interlayer coupling and the single sheet will peel off and scroll to form nanotubes, with the tension in the layer being the driving force in this formation.

The dimension of the nanotube is controlled by the surface tension and with interlayer coupling energy and Coulomb force.

The structure of the nanotubes is confirmed by XRD, Raman and HRTEM. Due to the closely related structures of TiO_2 and other titanate compounds similarities with the starting material are seen in the spectra, however the results may be more closely indexed as trititanate.

To gain further evidence of this mechanism, we reacted bulk $H_2Ti_3O_7$ and $Na_2Ti_3O_7$ specimens with 10 molar sodium hydroxide. Nanotubes were produced from both reactions. The starting material was shown to contain no TiO_2 through XRD.

6.2 Nanotubes from $K_{4-x}H_xNb_6O_{17}$

In previous work straight chain amines were used as intercalation and exfoliation materials in the reaction with partially ion exchanged potassium hexaniobate, $K_{4-x}H_xNb_6O_{17}$, to create nanotubes. The number of layers in the wall is typically 4, but can be between 3 and 8. When tetrabutylammonium hydroxide is used the intershell spacing is 0.83 nm. The intershell spacing can be altered using di and tri substituted amines. When diethyl amine is used the spacing is increased to 0.93 and 1.4 nm. The diameter of the tubes is 20 nm with a wide range of lengths.

Changing the intercalation agent to triethyl amine increased the spacing to 2.18 nm, and the outer diameter to 40 nm. Nanotubes with a decreased spacing of 0.74 nm are also observed.

When an amine is intercalated between the layers of the crystal the top layer can cleave off, and as the monolayer is asymmetric an intrinsic tension exists which curves the sheet to release the strain and produce tubes. When the $K_4Nb_6O_{17}$ has not been acid treated the intercalation results in the exfoliation of large bilayers and multilayers.

It can be seen that altering the intercalating amine results in nanotubes of different intershell spacing and consequently, different diameters. This may be useful in catalytic reactions, where the tube size may affect activity and in the many instances where amines are used as templates in nanoscale synthesis. These results show that, rather than just cleave the layer off and scroll independently, the amine molecules are incorporated into the nanotube and affect its size.

When the amine is replaced with other similar molecules no nanotubes are produced, however in the case of ethanol and tetra-n-butlyphosphonium bromide, nanorods are produced.

6.3 Nanotubes and nanorods from other metal and non-metal oxides

The production of nanotubes from various metal and non-metal oxides was attempted using the previous methods of hydrothermal reaction with 10 molar NaOH solution and stirring at room temperature with amine solution. Nanotubes were only produced in one case, however several nanorods were prepared.

Reacting Al_2O_3 with 10 M NaOH in a sealed autoclave produced nanorods with an average diameter of 37.6 nm and lengths of around 200 nm. The rods were composed of monoclinic Al_2O_3. The same reaction produced rods with an average

diameter of 25 nm in the case of Ta_2O_5. No rods or tubes were produced from the hydrothermal reactions of SiO_2 and WO_3 with NaOH.

Stirring the parent oxide with amine in water at room temperature produced nanorods from WO_3 and Ta_2O_5. When WO_3 was stirred with butyl amine in water nanords with an average diameter of 12.9 nm and lengths of less than 100 nm were produced. The structure of the rods was shown to be tetragonal WO_3 by SAED.

When Ta_2O_5 was stirred with butyl amine at room temperature nanorods with an average diameter of 32 nm and lengths in excess of 200 nm were produced. The rods were hexagonal in structure, with the (001) plane running parallel to the rod growth axis. The proposed mechanism of formation of the rods is that amine molecules intercalate into the structure and cleave off the rods.

When tetraethylammonium hydroxide was reacted with Ta_2O_5 a mixture of nanotubes and nanorods were produced. The rods had a wide diameter distribution, with an average diameter of 31 nm and lengths greater than 1 μm. The rods were shown to have a hexagonal Ta_2O_5 structure, with the (001) plane running parallel to the nanorod growth axis. The same formation mechanism is proposed.

The nanotubes had a much smaller diameter distribution, with an average diameter of 8.8 nm. The number of shells in each tube was either three or four, with many tubes having more layers on one side than the other which is indicative of a scrolled structure. The tubes had an interlayer spacing of 0.66 nm and lengths between 60 and 200 nm and are open at both ends. The nanotubes had a hexagonal Ta_2O_5 structure with the interlayer spacing corresponding to the (001) plane, and a spacing of 3.5 Å, which corresponds to the (111) plane, running perpendicular to the long axis of the nanotube. The tubes are thought to form when thin sheets of material, rather than

rods are cleaved off. These sheets then scroll to form tubes due to an asymmetry in the sheet or to release strain.

When a sample containing tubes was heated to remove water the tubes decomposed into nanorods, which self-assembled, and were of the same order as the nanotubes, with diameters of 8.5 nm and lengths of around 100 nm. The structure of the rods was again hexagonal Ta_2O_5, with the (2-10) plane observed at 43° to the growth axis of the rod. It is thought that the rods are formed from tubes that collapse upon heating due to loss of structural amine or water molecules. The average diameter of rods produced from Ta_2O_5 is summarised in Fig. 5.28.

6.4 Future work

The production of trititanate nanotubes directly from the parent layered material has opened up the possibility of preparing nanotubes from a family of layered transition metal hydroxide oxides by the hydrothermal reaction with concentrated sodium hydroxide. The structural motif thought necessary for the production of nanotubes is stepped layers of metal-oxide polyhedra separated by protons or alkaline metal cations, which makes scrolling much easier, shown in Fig. 6.1. Examples of componds from this family include $H_2Ti_4O_9$, $H_4Nb_6O_{17}$, HNb_3O_8, $HTiNbO_5$, HTi_2NbO_7, $H_3Ti_5NbO_{14}$, $H_xV_2O_5$ and H_xMVO_5 (M=Nb or Ta), H_4MO_5 and H_2MO_4 (M = Mo or W), $HTaWO_6$. Nb can normally be replaced by Ta in Nb-containing compounds.

This work has also shown that nanorods of metal and non-metal oxides can be produced by stirring the oxide with tetraethylammonium hydroxide at room temperature. This synthetic route is low cost and facile and should be expandable to other metal oxides.

It would be interesting to investigate the catalytic properties of the synthesised nanotubes in the future.

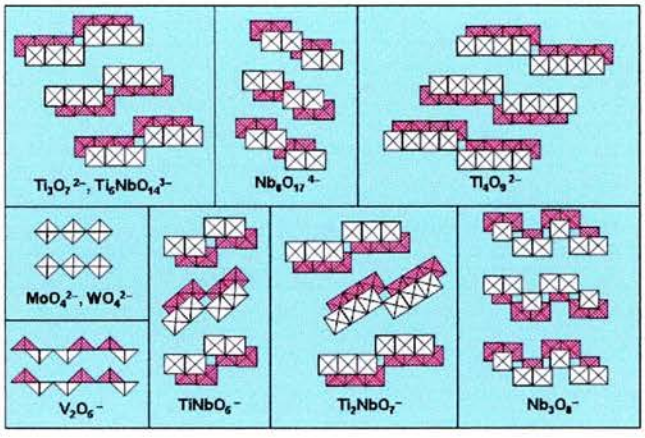

Fig. 6.1 Stepped structure of transition metal hydroxide oxides.

References

1. www.dti.gov.uk/innovation/nanotechnologyreport.pdf
2. www.nanotec.org.uk/finalReport.htm
3. www.bbc.co.uk
4. S. Iijima, *Nature*, 1991, **354**, 56.
5. N. Hamada, S. Sawada, A. Oshiyama, *Phys. Rev. Lett.*, 1992, **68**, 1579.
6. C. N. R. Rao, M. Nath, *Dalton Trans.*, 2003, **1**, 1.
7. www.nanoledge.com/
8. Q. H. Wang, A. A. Setlur, J. M. Lauerhaas, J. Y. Dai, E. W. Seelig, R. P. H. Changa, *App. Phys. Lett.*, 1998, **72**, 2912.
9. www.nano-proprietary.com/index.htm?ani.htm
10. A. B. Dalton, S. Collins, E. Munoz, J. M. Razal, V. H. Ebron, J. P. Ferraris, J. N. Coleman, B. G. Kim, R. H. Baughman, *Nature*, 2003, **423**, 703.
11. M. Zhang, S. Fang, A. A. Zakhidov, S. B. Lee, A. E. Aliev, C. D. Williams, K. R. Atkinson, R. H. Baughman, *Science*, 2005, **309**, 1215.
12. R. Alwin, *Nature*, 1998, **393**, 49.
13. G. L. Che, B. B. Lakshmi, C. R. Martin, E. R. Fisher, *Langmuir*, 1999, **15**, 750.
14. J. M. Planex et al, *J. Am. Chem. Soc.*, 1994, **116**, 7935.
15. G. Mestl, N. I. Maksimov, N. Keller, V.V. Roddatis, R. Schlogl, *Angew. Chem.*, 2001, **40**, 2066.
16. D. J. D. Corcoran, D. P. Tunstall, J. T. S. Irvine, *Solid State Ionics*, 2000, **136**, 297.
17. R. Tenne, L. Margulis, M. Genut, G. Hodes, *Nature*, 1992, **360**, 444.
18. Y. Feldman et al. *Science*, 1995, **267**, 222.

19. M. Nath, A. Govindaraj, C. N. R. Rao, *Adv. Mater.*, 2001, **13**, 283.

20. M. Remskar, Z. Skraba, F. Cleton, R. Sanjines, F. Levy, *App. Phys. Lett.*, 1996, **69**, 351.

21. M. Remskar, Z. Skraba, M. Regula, C. Ballif, R. Sanjinés, F. Lévy, *Adv. Mater.*, 1998, **10**, 246.

22. M. Nath, S. Kar, A. K. Raychaudhuri, C. N. R. Rao, *Chem. Phys. Lett.*, in press.

23. M. Nath, C. N. R. Rao, *J. Am. Chem. Soc.*, 2001, **123**, 4841.

24. M. Nath, C. N. R. Rao, *Angew. Chem., Int. Ed.*, 2002, **41**, 3451.

25. M. Brorson, T.W. Hansen, C.J.H. Jacobsen, *J. Am. Chem. Soc.*, 2002, **124,** 11582.

26. D. H. Galván, J.-H. Kim, M. B. Maple, M. Avalos-Berja, E. Adem, *Fullerene Sci. Technol.*, 2000, **8**, 143.

27. D. H. Galvan, Shi Li, W. M. Yuhasz, J.-H. Kim, M. B. Maple, E. Adem, *Physica C*, 2003, **398**, 147.

28. C. N. R. Rao, A. G. Govindaraj, F. L. Deepak, N. A. Gunari, M. Nath, *Appl. Phys. Lett.*, 2001, **78**, 1853.

29. J. R. Ota *et al*, *Nanotech., 2005,* **16**, 2415.

30. L. Dloczik, R. Engelhardt, K. Ernst, S. Fiechter, I. Seiber, R. Könenkamp, *Appl. Phys. Lett.*, 2001, **78**, 3687.

31. X. Ziang, Y. Xie, L. Zhu, W. He, Y. Qian, *Adv. Mater.*, 2001, **13**, 1278.

32. Y. Peng, Z. Meng, C. Zhong, J. Lu, L. Xu, S. Zhang, Y. Qian, *New J. Chem.*, 2001, **25**, 1359.

33. N. G. Chorpa et al., *Science*, 1995, **269**, 966.

34. J. Goldberger, R. He, Y. Zhang, S. Lee, H. Yan, H. J. Choi, P. Yang, *Nature*, 2001, **422**, 599.

35. H. Nakamura, Y. Matsui, *J. Am. Chem. Soc,* 1995, **117**, 2651.

36. H. Nakamura, Y. Matsui, *Adv. Mater.*, 1995, 7, 871.

37. A. P. Lin, C. Y. Mou, S. D. Liu, *Adv. Mater.*, 2000, **12**, 103.

38. M. Harada, M. Adachi, *Adv. Mater.*, 2000, **12**, 839.

39. L. Wang, S. Tomura, F. Ohashi, M. Maeda, M. Suzuki, K. Inukai, *J. Mater. Chem.*, 2001, **11**, 1465.

40. Y. Zhang, A. Reller, *Chem. Commun.*, 2002, 606.

41. B. C. Satishkumar, A. Govindaraj, E. M. Vogl, L. Basumallick, C. N. R. Rao, *J. Mater. Res.,* 1997, **12**, 604.

42. H. J. Chang, Y. F. Chen, H. P. Lin C. Y. Mou, *Appl. Phys. Lett.*, 2001, **78**, 3791.

43. L. Pu, X. Bao, J. Zou, D. Feng, *Angew. Chem., Int. Ed.*, 2001, **40**, 1490.

44. J. Zou, L. Pu, X. Bao, D. Feng, *Appl. Phys. Lett.*, 2002, **80**, 1079.

45. M. E. Spahr, P. Bitterli, R. Nesper, M. Müller, F. Krumeich, H. U. Nissen, *Angew. Chem., Int. Ed.*, 1998, **37**, 1263.

46. F. Krumeich, H.-J. Muhr, M. Niederberger, F. Bieri, B. Schnyder, R. Nesper, *J. Am. Chem. Soc.*, 1999, **121**, 8324.

47. M. Niederberger, H. J. Muhr, F. Krumeich, F. Biere, D. Gunther, R. Nesper, *Chem. Mater.*, 2000, **12**, 1995.

48. P. Hoyer, *Langmuir*, 1996, **12**, 1411.

49. T. Kasuga, M. Hiramatsu, A. Hoson, T. Sekino, K. Niihara, *Langmuir*, 1998, **14**, 3169.

50. H. Imai, Y. Takei, K. Shimizu, M. Matsuda, H. Hirashima, *J. Mater. Chem.*, 1999, **9**, 2971.

51. J. Zhang, L. Sun, C. Liao, C. Yan, *Chem. Comm.*, 2002, 262.

52. B. A. Hernandez, K.-S. Chang, E. R. Fisher, P. K. Dorhout, *Chem. Mater.*, 2002, **14**, 480.

53. B. Cheng, E. T. Samulski, *J. Mater. Chem.*, 2001, **11**, 2901.

54. G. Tourillon, L. Pontonnier, J. P. Levy, V. Langlais, *Electrochem. Solid-State Lett.*, 2000, **3**, 20.

55. C. R. Martin, M. Nishizawa, K. Jirage, M. Kang, *J. Phys. Chem. B*, 2001, **105**, 1925.

56. B. Mayers, Y. Xia, *Adv. Mater.*, 2002, **14**, 279.

57. J. Bao, C. Tie, Z. Xu, Q. Zhou, D. Shen, Q. Ma, *Adv. Mater.*, 2001, **13**, 1631.

58. S. V. Krivovichev, V. Kahlenberg, I. G. Tananaev, R. Kaindl, E. Mersdorf, B. F. Myasoedov, *J. Am. Chem. Soc.*, 2005, **127**, 1072.

59. S. V. Krivovichev, V. Kahlenberg, I. G. Tananaev, R. Kaindl, E. Mersdorf, B. F. Myasoedov, *Angew. Chem. Int. Ed.*, 2005, **44**, 1134.

60. M. Yada, M. Mihara, S. Mouri, M. Kuroki, T. Kijima, *Adv. Mater.*, 2002, **14**, 309.

61. W.-Q. Han, L. Wu, Y. Zhu, *J. Am. Chem. Soc.*, 2005, **127**, 12814.

62. Y. R. Hacohen, E. Grunbaum, R. Tenne, J. Sloan, J. L. Hutchison, *Nature*, 1998, **395**, 337.

63. Y. Q. Zhu, W. K. Hsu, H. Terrones, N. Grobert, B. H. Chang, M. Terrones, B. Q. Wei, H. W. Kroto, D. R. M. Walton, C. B. Bothroyd, I. Kinlöch, G. Z. Chen, A. H. Windle, D. J. Fray, *J. Mater. Chem.*, 2000, **10**, 2570.

64. J. Chen, S. L. Li, Q. Xu, K. Tanaka, *Chem. Comm.*, 2002, **16**, 1722.

65. A. Rothschild, S.R. Cohen, R. Tenne, *Appl. Phys. Lett.*, 1999, **75**, 4025.

66. M. Nath, S. Kar, A. K. Raychaudhuri, C. N. R. Rao, *Chem. Phys. Lett*, 2003, **368**, 690.

67. L. Rapoport, Y. Bilik, Y. Feldman, M. Homyonfer, S. R. Cohen, R. Tenne, *Nature*, 1997, **387**, 791.

68. M. Adachi, Y. Murata, M. Harada, *Chem. Lett.*, 2000, **8**, 942.

69. G. Dagan, M. Tomkiewicz, *J. Phys. Chem.*, 1993, **97**, 12651.

70. K. Fukushima, I. Yamada, *J. Appl. Phys.*, 1989, **65**, 619.

71. G. L. Che, B. B. Lakshmi, C. R. Martin, E. R. Fisher, *Langmuir*, 1999, **15**, 750.

72. www.titaniumart.com/photocatalysis-ti02.html

73. M. G. Kang, N. G. Park, Y. J. Park, K. S. Ryu, *Sol. Energy Mater.*, 2003, **75**, 475.

74. H. Imai, M. Matsuta, K. Shimizu, H. Hirashima, N. Negishi, *Solid State Ionics,* 2002, **151**, 183.

75. www.nanoquest.com.au/TiO2.htm

76. www.state.ar.us/agc/titanium.htm

77. T. Kasuga, M. Hiramatsu, A. Hoson, T. Sekino, K. Niihara, *Adv. Mater.*, 1999, **11**, 1307.

78. Q. Chen, W. Zhou, G. Du, L.-M. Peng, *Adv. Mater.*, 2002, **14**, 1208.

79. G. H. Du, Q. Chen, R. C. Che, Z. Y. Yuan, L.-M. Peng, *Appl. Phys. Lett.*, 2001, **22**, 3702.

80. A. Thorne, Senior Honours Project, University of St. Andrews, 2002.

81. Q. Chen, G. H. Du, S. Zhang, L.-M. Peng, *Acta Cryst. Section B,* 2002, **58**, 587.

82. A. Thorne, A. Kruth, D. Tunstall, J. T. S. Irvine, W. Zhou, *J. Phys. Chem. B*, 2005, **109**, 5439.

83. T. P. Fiest, P. K. Davies, *J. Solid State Chem.*, 1992, **101**, 275.

84. S. Zhang, L-M Peng, Q. Chen, *Phys. Rev. B.*, 2005, **71**, 014104.

85. J. Hong, J. Cao, J.Z. Sun, H.Y. Li, H.Z. Chen, M. Wang, *Chem. Phys. Lett.*, 2003, **380**, 366.

86. V. Idakiev, Z.Y. Yuan, T. Tabakova, B.L. Su, *Appl. Cat. A*, 2005, **281,** 149.

87. M. Haruta, *Cat. Today*, 1997, **36**, 153.

88. C.-H. Lin, S.-H. Chien, J.-H. Chao, C.-Y. Sheu, Y.-C. Cheng, Y.-J. Huang, C.-H. Tsai, *Cat. Lett.*, 2002, **80**, 153.

89. H. Tokudome, M. Miyauchi, *Chem. Lett.*, 2004, **33**, 1108.

90. M. Hodos, E. Horvath, H. Haspel, A. Kukovecz, Z. Konya, I. Kiricsi, *Chem. Phys. Lett.*, 2004, **399**, 512.

91. A. Kukovecz, M. Hodos, Z. Ko´nya, I. Kiricsi, *Chem. Phys. Lett.*, 2005, **411**, 445.

92. R. Z. Ma, T. Sasaki, Y. Bando, *Chem. Comm*, 2005, 948.

93. X. Sun, Y. Li, *Chem. J. Eur.*, 2003, **9**, 2229.

94. J. R. Li, Z. L. Tang, Z. T. Zhang, *Electrochem. Solid State Lett*, 2005, **8**, A316.

95. O. K. Varghese, D. Gong, M. Paulose, K. G. Ong, E. C. Dickey, C.A. Grimes, *Adv. Mater.*, 2003, **15**, 624.

96. A. Kleinhammes, G. W. Wagner, H. Kulkarni, Y. Jia, Q. Zhang, L.-C. Qin, Y. Wu, *Chem. Phys. Lett.*, 2005, **411**, 81.

97. M. Wei, Y. Konishi, H. Zhou, H. Sugihara, H. Arakawa, *Solid State Comm.*, 2005, **133**, 493.

98. S. Zhang, L.-M. Peng, Q. Chen, G.H. Du, Y. Yu, W. Zhou, *J. Mater. Chem.*, 2004, **14**, 1437.

99. K. Nassau, J.W. Shiever, J.L. Bernstein, *J. Electrochem. Soc*, 1969, **116**, 348.

100. G. Lagaly, K. Beneke, *J. Inorg. Nucl. Chem*, 1976, **38**, 1513.

101. M. A. Bizeto, V. R.L. Constantino, *Mater. Res. Bull.*, 2004, **39**, 1811.

102. K. Domen, A. Kudo, M. Shibata, A. Tanaka, K. Maruya, T. Onishi, *J. Chem. Soc. Chem. Comm*, 1986, **23**, 1706.

103. K. Sayama, A. Tanaka, K. Domen, K. Maruya, T. Onishi, *J. Phys. Chem.*, 1991, **95**, 1345.

104. A. Kudo, K. Sayama, A. Tanaka, K. Doen, K. Maruya, T. Onishi, *J. Catal.*, 1998, **120**, 337.

105. J. Yoshimura, *Bull. Chem. Soc. Jpn.*, 1995, **68**, 2439.

106. N. Miyamoto, H. Yamamoto, R. Kaito, K. Kuroda, *Chem. Comm.*, 2002, 2378.

107. N. Miyamoto, T. Nakato, *J. Phys. Chem. B,* 2004, **108**, 6152.

108. R. Kaito, K. Kuroda, *J. Phys. Chem. B*, 2003, **107**, 4043.

109. G. H. Du, L.-M. Peng, Q. Chen, S. Zhang, W. Zhou, *Appl. Phys. Lett.*, 2003, **83**, 1638.

110. G. B. Saupe, C. C. Waraksa, H. -N. Kim, Y. J. Han, D. M. Kaschak, D. M. Skinner, T. E. Mallouk, *Chem. Mater.*, 2000, **12**, 1556.

111. M. Gasperin, M. L. Bihan, *J. Solid State Chem.*, 1982, **43**, 364.

112. S. Uchida, et al, *J. Mater. Sci.*, 1998, **33**, 5125.

113. J. Hastings, O. Howarth, *J. Chem. Soc. Dalton Trans.*, **1992**, 209.

114. Progress in Transmition Electron Microscopy. 1 Concepts and Techniques, Edited by Xiao-Feng Zhang and Ze Zhan, Tsughua University press, 1999.

115. Fundamentals of Molecular Spectroscopy, C. Banwell and E McCash, 1994, McGraw-Hill Book Company.

116. S. Zhang, L.M. Peng, Q Chen, G.H. Du, W. Zhou, G. Dawson, *Phys. Rev. Lett.*, 2003, **91**, 256103.

117. www.accelry.com

118. A. R. Armstrong, G. Armstrong, J. Canales, P. G. Bruce, *Angew. Chem. Int. Ed.*, 2004, **43**, 2286.

119. S. Papp, L. Korosi, V. Meynen, P. Cool, E. F. Vansant, I. Dekany, *J. Solid State Chem.*, 2005, **178**, 1614.

120. Organic Chemistry, Seventh Edition, T.W.G. Solomns, C.B. Fryhle, John Wiley & Sons, 2000.

121. www.webelements.com

122. A. R. Armstrong, J. Canales, P. G. Bruce, *Angew. Chem. Int. Ed.*, 2004, **43**, 4899.

123. B. C. Satishkumar, A. Govindaraj, M. Nath, C. N. R. Rao, *J. Mater. Chem.*, 2000, **10**, 2115.

124. H. A. Threrese, J. Li, U. Kolb, W. Tremel, *Solid State Sciences*, 2005, **7**, 67.

125. Z. Gu, Y. Ma, W. Yang, G. Zhang, J. Yao, *Chem. Comm.*, 2005, 3597.

126. X. W. Lou, H. C. Zeng, *Inorg. Chem.*, 2003, **42**, 6169.

127. Y. Q. Zhu, W. Hu, W. K. Hsu, M. Terrones, N. Grobert, J. P. Hare, H. W. Kroto, D. R.M. Walton, H. Terrones, *Chem. Phys. Lett.*, 1999, **309**, 327.

128. Y. Q. Zhu, W. K. Hsu, N. Grobert, B. H. Chang, M. Terrones, H. Terrones, H. W. Kroto, D. R. M. Walton, *Chem. Mater.*, 2000, **12**, 1190.

129. Z. Liu, Y. Bando, C. Tang, *Chem. Phys. Lett.*, 2003, **372**, 179.

130. H. Zhang, M. Feng, F. Liu, L. Liu, H. Chen, H. Gao, J. Li, *Chem. Phys. Lett.*, 2004, **389**, 337.

131. J. Zhou, Y. Ding, S. Z. Deng, L. Gong, N. S. Xu, Z. L. Wang, *Adv. Mater.*, 2005, **17**, 2107.

132. Y. B. Li, Y. Bando, D. Golberg, K. Kurashima, *Chem. Phys. Lett.*, 2003, **367**, 214.

133. Y. Z. Jin, Y. Q. Zhu, R. L. D. Whitby, N. Yao, R. Ma, P. C. P. Watts, H. W. Kroto, D. R. M. Walton, *J. Phys. Chem. B,* 2004, **108**, 15572.

134. K. Lee, W. S. Seo, J. T. Park, *J. Am. Chem. Soc.* 2003, **125**, 3408.

135. X.-L. Li, J.-F. Liu, Y.-D. Li, *Inorg. Chem.*, 2003, **42**, 921.

136. Y. Koltypin, S. I. Nikitenko, A. Gedanken, *J. Mater. Chem.*, 2002, **12**, 1107.

137. K.-S. Ahn, Y.-C. Nah, Y.-E. Sung, K.-Y. Cho, S.-S. Shin, J.-K. Park, *Appl. Phys. Lett.*, 2002, **81**, 3930.

138. P. Poizot, S. Laruelle, S. Grugeon, L. Dupont, J.-M. Tarascon, *Nature*, 2000, **407**, 406.

139. C. Santato, M. Odziemkowski, M. Ulmann, J. Augustynski, *J. Am. Chem. Soc.*, **2001,** 123, 10639.

140. I. Turyan, U. O. Krasovec, B. Orel, T. Saraidorov, R. Reisfeld, D. Mandler, *Adv. Mater.*, 2000, **12**, 330.

141. W. Grunert, E. S. Shpiro, R. Feldhaus, K. Anders, G. V. Antoshin, K. M. Minachev, *J. Catal.*, 1987, **107**, 522.

142. M. Kazuta, K. I. Tanaka, *J. Catal.*, 1990, **123**, 164.

143. I. Rodriguez-Ramos, A. Guerrero-Ruiz, N. Homs, P. Ramirez de la Piscina, J. L. G. Fierro, *J. Mol. Catal. A*, 1995, **95**, 147.

144. A. J. Van Roosmalen, J. C. Mol, *J. Catal.*, 1982, **78**, 17.

145. J. Haber, J. Janas, M. Schiavello, R. J. D. Tilley, *J. Catal.*, 1983, **82**, 395.

146. T. Yamaguchi, Y. Tanaka, K. Tanabe, *J. Catal.*, 1980, **65**, 442.

147. A. Pietruszka, F. Di Gregorio, N. Keller, V. Keller, *Cat.Today*, 2005, **102**, 94.

148. www.azom.com/details.asp?ArticleID=52

149. W. F. Li, X. L. Ma, W. S. Zhang, W. Zhang, Y. Li, Z. D. Zhang, *Physica A*, 2006, **203**, 294.

150. S. C. Kuiry, E. Megen, S. A. Patil, S. A. Deshpande, S. Seal, *J. Phys. Chem. B*, 2005, **109**, 3868.

151. G. Gundiah, F. L. Deepak, A. Govindaraj, C. N. R. Rao, *Topics in Cat.*, 2003, **24,** 137.

152. A. J. Deng, P. Yu, M. Y. Yau, C. S. Ku, D. H. L. Ng, *J. Am. Ceram. Soc.*, 2003, **86,** 1385.

153. Y. B. Li, Y. Bando, D. Goldberg, *Adv. Mater.*, 2005, **17**, 1401.

154. J. S. Lee, B. Min, K. Cho, S. Kim, J. Park, Y. T. Lee, N. S. Kim, M. S. Lee, S. O. Park, J. T. Moon, *J. Crys. Growth*, 2003, **254**, 443.

155. B. Min, J. S. Lee, J. W. Hwang, K. H. Keem, M. I. Kang, K. Cho, M. Y. Sung, S. Kim, M. -S. Lee, S. O. Park, J. T. Moon, *J. Crys. Growth,* 2003, **253**, 565.

156. Y. M. Luo, Z. Y. Hou, D. F. Jin, J. Gao, X. M. Zheng, *Mat. Lett.*, 2006, **60,** 393.

157. www.wikipedia.org/wiki/

158. The chemistry of niobium and tantalum, F. Fairbrother, Elsevier Pub., 1967.

159. T.-H. Fang, W.-J. Chang, *Physica B*, 2004, **352**, 190.

160. J. H. Jung, T. Shimizu, S. Shinkai, *J. Mater. Chem.*, 2005, **15**, 3979.

161. F. Miyaji, Y. Tatematsu, Y. Suyama, *J. Ceram. Soc. Jpn.*, 2001, **109**, 924.

162. H. M. Romero, A. M. Villafane, J. C. Nava, P. G. Casillas, C. M. Perez, *Ann. Di Chim.*, 2005, **95**, 703.

163. J. Y. Seong, K. S. Chung, S. K. Kwak, Y. H. Kim, D. G. Moon, J. I. Han, W. K. Kim, *J. Kor. Phys. Soc.*, 2004, **45**, S914.

164. K. Nakajima, D. Lu, M. Hara, K. Domen, J. N. Kondo, *Mol. Sieves*, 2005, **158**, 1477.

165. M. J. O'Connell et al, *Science*, 2002, **297**, 593.